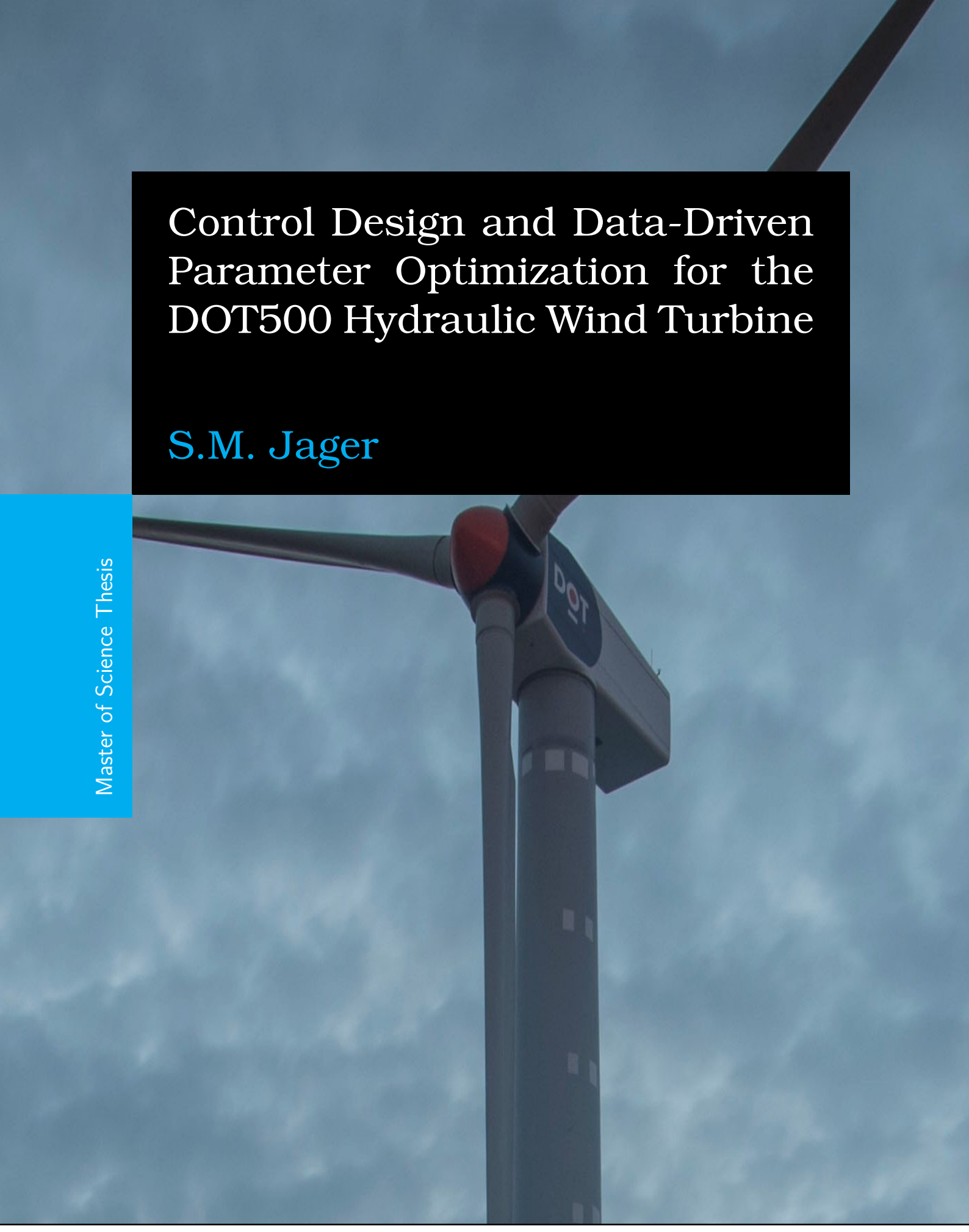

Control Design and Data-Driven Parameter Optimization for the DOT500 Hydraulic Wind Turbine

S.M. Jager

Master of Science Thesis

TU Delft Delft University of Technology

Delft Center for Systems and Control

Control Design and Data-Driven Parameter Optimization for the DOT500 Hydraulic Wind Turbine

Master of Science Thesis

For the degree of Master of Science in Systems and Control at Delft University of Technology

S.M. Jager

January 3, 2017

Faculty of Mechanical, Maritime and Materials Engineering (3mE) · Delft University of Technology

The work in this thesis was supported by DOT BV. Their cooperation is hereby gratefully acknowledged.

Abstract

In an effort to reduce the Levelized Cost Of Energy (LCOE) of offshore wind energy to a market competitive level, a new wind turbine prototype with hydraulic drive train has been introduced by the start-up company Delft Offshore Turbine (DOT). In the DOT concept, a seawater pump is directly connected to the rotor shaft. The pump pressurizes sea water, which is transferred to a hydro-power station at sea level. There, the hydraulic power is converted to electric power by means of a Pelton turbine, which is mechanically connected to an electric generator.

In below-rated wind conditions, practically all commercial wind turbines regulate the rotor speed by adjusting the generator torque demand. However, due to the decoupling of the rotor and generator in the DOT concept, conventional below-rated torque control is no longer possible. With the hydraulic drive train concept considered in this thesis, an alternative torque control strategy is designed and implemented, where fluid pressure is regulated to vary the system torque. The developed hydraulic torque control strategy is integrated in the turbine control system, which includes e.g. yaw, pitch and supervisory control.

Functionality of the derived strategy is validated through field trials, performed on a 500 kW prototype of the DOT wind turbine. A second-hand Vestas V44 wind turbine was retrofitted with hydraulic components and installed on the Maasvlakte II for this purpose (see Figure 1). Since the required seawater pump for the ideal DOT concept is not yet commercially available on the market, an intermediate hydrostatic oil transmission was used as a hydraulic gearbox between rotor and water pump. However, the operating principles of the control strategy remain identical for both the ideal and intermediate DOT scenario.

Results show that below-rated speed regulation is possible with the derived hydraulic torque controller. The developed strategy enables operation along the theoretical optimal tip-speed ratio for attaining the maximum (rotor) power coefficient. The blade fine-pitch angle, which leads to maximum rotor power extraction in the below-rated region, was subsequently found with the direct data-driven Extremum Seeking Control (ESC) algorithm. Finally, the ESC method was implemented to find the generator speed feedforward control gain. Results indicate an instant generator power increase and led to the detection of a malfunctioning sensor. Therefore, ESC appeared to be a valuable tool to deal with modelling and measurements uncertainties.

The developed strategy enables operation at the tip-speed ratio for which the turbine rotor attains maximum power extraction from the wind. However, due to the mismatching efficiency operating envelopes of the rotor and the hydraulic components, optimal rotor power extraction does not necessarily lead to maximum electricity generation. Deviation from the theoretic optimal tip-speed ratio is therefore expected to result in higher electricity generation. For future DOT prototypes, where the intermediate oil loop will be omitted, an Extremum Seeking Control power maximisation approach is suggested.

Figure 1: Photo of the DOT500 prototype at Maasvlakte II, the Netherlands.

Contents

Acknowledgements

I would like to thank my supervisors dr. ir. J.W. van Wingerden, dr. ir. N.F.B. Diepeveen (DOT BV) and ir. S.P. Mulders for their assistance during the course of this graduation project. Special thanks and appreciation go to ir. S.P. Mulders for his motivation and dedication in helping to make this project to a success.

I also wish to thank all of my colleagues at DOT BV for providing me with the opportunity to work on an actual wind turbine and the very rewarding experience to work with and learn from them.

I further would like to express my gratitude to my family for their endless support during the whole period of my bachelor and master study.

Delft, University of Technology S.M. Jager
January 3, 2017

Chapter 1

Introduction

This chapter starts with an introduction to Delft Offshore Turbine and the motivation behind this thesis research topic. Then, in Section 1-2, the problem is formalised into a clear research objective. Finally, the thesis structure is given in Section 1-3.

1-1 Motivation: control design of the DOT500 hydraulic turbine

Background: Delft Offshore Turbine (DOT)

The start-up company Delft Offshore Turbine (DOT) aims to make offshore wind farms a cost-effective source of energy, by redesigning the way wind energy is converted and transported to the onshore electricity grid. The main concept idea is to radically reduce the weight, complexity and costs of offshore wind turbines by removing multiple heavy components from the nacelle and replacing them with robust hydraulic components (see Figure 1-1).

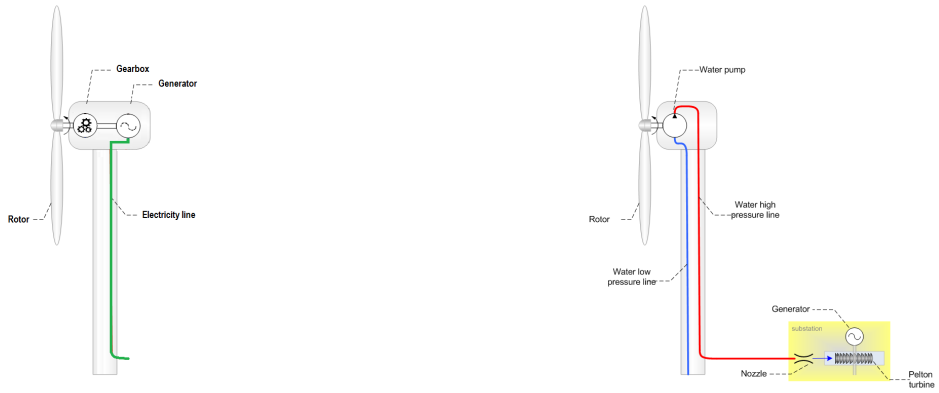

(a) Offshore wind industry standard **(b)** Ideal DOT design concept [1]

Figure 1-1: Wind turbine configurations

In this concept the turbine rotor powers a water pump that pushes a high-pressure water flow to a hydro-power station at sea level. There, the hydraulic power is converted to electric power by means of a Pelton turbine, which is mechanically connected to an electric generator. Eventually, the main goal is to combine high-pressure water lines from multiple turbines to centralize and simplify electricity generation, as shown in Figure 1-2. The DOT idea was patented by Van der Tempel [2], and a successful feasability study was carried out by Diepeveen [1].

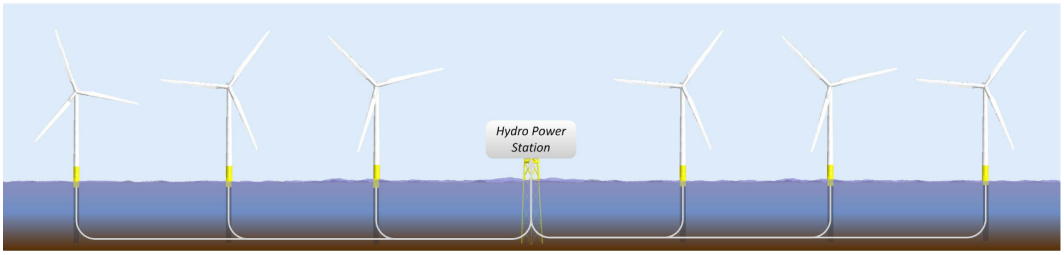

Figure 1-2: Artist impression of DOT wind farm [1]

The use of water instead of oil reduces the risk of oil pollution in case of leakages and obviates the need of a return line to the hydro-power station. This should, together with the abundantly availability of seawater offshore, outweigh the unfavourable viscous properties of water with respect to oil hydraulics.

Current state of DOT

Unfortunately the required low-speed, high-torque water pump is not yet commercially available and therefore a 500 kW water pump is currently being developed by DOT. In order to speed up the development of the DOT concept, an intermediate transmission oil loop was introduced to the set-up, as presented in Figure 1-3. The intermediate hydrostatic transmission acts as a gearbox between rotor and water pump. Off-the-shelf components are selected for this design, resulting in a reduced overall efficiency compared to the original concept, but allows for faster development.

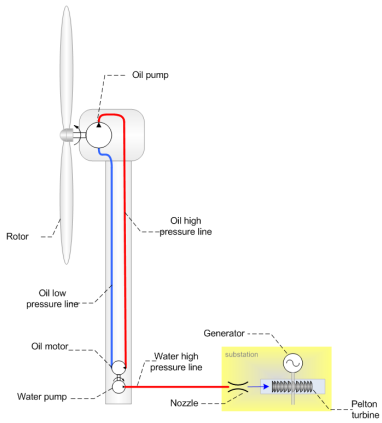

Figure 1-3: DOT500 set-up with integrated oil loop [1]

A second-hand Vestas V44 turbine, with a nominal power rating of 600 kW, is acquired and converted to the intermediate hydraulic configuration in Figure 1-3. This set-up will be referred to in this thesis as the DOT500 turbine. A prototype was erected in June 2016 at Maasvlakte II, the Netherlands.

Problem: control design of the DOT500

Practically all drive trains of commercial offshore wind turbines consist of a rotor-gearbox-generator configuration in the nacelle. In the DOT500 configuration, however, the generator is mechanically decoupled from the rotor. This eliminates the generator torque control possibility, which is normally used to regulate turbine rotor speed in below-rated wind conditions. Instead, the system torque of the DOT500 turbine is controlled by varying the high-pressure water flow by altering the effective nozzle diameter. For this purpose, spear valves are used with an adjustable nozzle diameter, as shown in Figure 1-4.

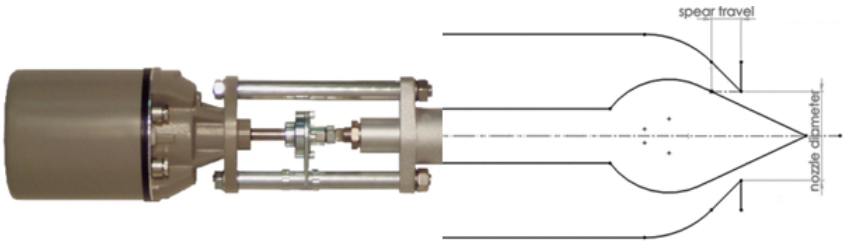

Figure 1-4: Spear valve actuator configuration. The system torque of the DOT500 is controlled by varying the high-pressure water flow by altering the effective nozzle diameter.

Where in conventional turbines the required system torque is directly regulated by the generator torque demand, the relation between spear valve travel position (effective water flow area) and system torque of the DOT500 turbine is still unknown. Furthermore, based on this relation, a suitable spear valve control strategy has to be formulated and incorporated in the turbine control system; which includes e.g. yaw, pitch and supervisory control.

Since the acquired Vestas V44 is second-hand, the existing software can no longer be used and has to be redesigned and rewritten. Due to confidentiality reasons, accurate rotor aerodynamic data of the turbine is unavailable. Therefore yaw, pitch and supervisory control has to be derived through literature research, computer modelling and experimentation. Easy and reliable control design and implementation is essential, since the software is put into practice and tested on the actual wind turbine.

The control objective is to maximize wind energy capture, while taking into account of safe operation restrictions such as rated power, rated speed and cut-out wind speed. Due to many estimated design parameters, data-driven techniques are used for further parameter tuning once the turbine is operational. Due to the influence of turbulent wind conditions and the difficulties to distinguish these effects on the turbine performance, these data-driven techniques are still scarcely applied in the wind industry.

1-2 Research objective

Main research question

Due to the absence of the standard generator torque possibility, an alternative control solution is required for the DOT500 turbine. Therefore, the main research question of this thesis becomes:

How to implement below-rated hydraulic drive train control in the DOT500 wind turbine, as a substitute to regular generator torque control, and use direct data-driven optimization for verification of assumed controller parameters?

Which includes:

- How to derive the system torque mapping of a hydraulic wind turbine drive train and use this mapping to augment the standard control law for below-rated operation?
- How to incorporate hydraulic torque control into integrated wind turbine control?
- How to design and implement data-driven controller optimization techniques to deal with modelling and measurement uncertainty on a practical wind turbine set-up?

Deliverables

The main deliverable of this thesis is the design of a control strategy applied to the DOT500 hydraulic wind turbine, both in software and a functional description thereof. Functionality over the entire turbine operating range is proven through field trials. In addition, this work gives proof of performance increase by using Extremum Seeking Control parameter tuning.

Approach

First, a literature study is performed to analyse existing hydraulic wind turbine concepts. The DOT500 turbine is compared to these concepts, and its novelty is explained. In addition, since the DOT500 has many unknown parameters, different methods to improve turbine performance by tuning controller parameters directly from measurement data are explored.

Next a control strategy for the DOT500 is developed. Essential in this development is the replacement of traditional generator torque control by fluid pressure control. Furthermore, the strategy had to be robust, safe and conveniently implementable.

The effect of spear valve control on the system torque of the DOT500 drive train is analysed in detail on an indoor test set-up, before it is placed in the Vestas V44 turbine. With the acquired knowledge of the hydraulic drive train, fluid pressure control is incorporated into the developed overall control system, which includes e.g. yaw and pitch control. Design of

the latter required approximation of rotor dynamics and specific turbine knowledge through literature research, computer modelling and experimentation.

The overall performance of the control strategy is analysed through field trials. Finally, Extremum Seeking Control (ESC) is used to tune parameters of the DOT500 control system. First, the fine-pitch angle that leads to maximum rotor power in the below-rated region is experimentally derived. Second, the ESC algorithm is used to find the generator speed feedforward control gain. The latter experiment is also used to show the capability of the ESC algorithm to compensate for modelling and measurement errors.

1-3 Thesis structure

The mentioned approach is incorporated in the thesis structure, as depicted in Figure 1-5. First a literature study is performed in Chapters 2 and 3. Then the DOT control design is outlined and tested in Chapters 4 through 6. After a functional control system was developed, data-driven controller tuning is applied and described in Chapter 7. Conclusions & recommendations are presented in Chapter 8.

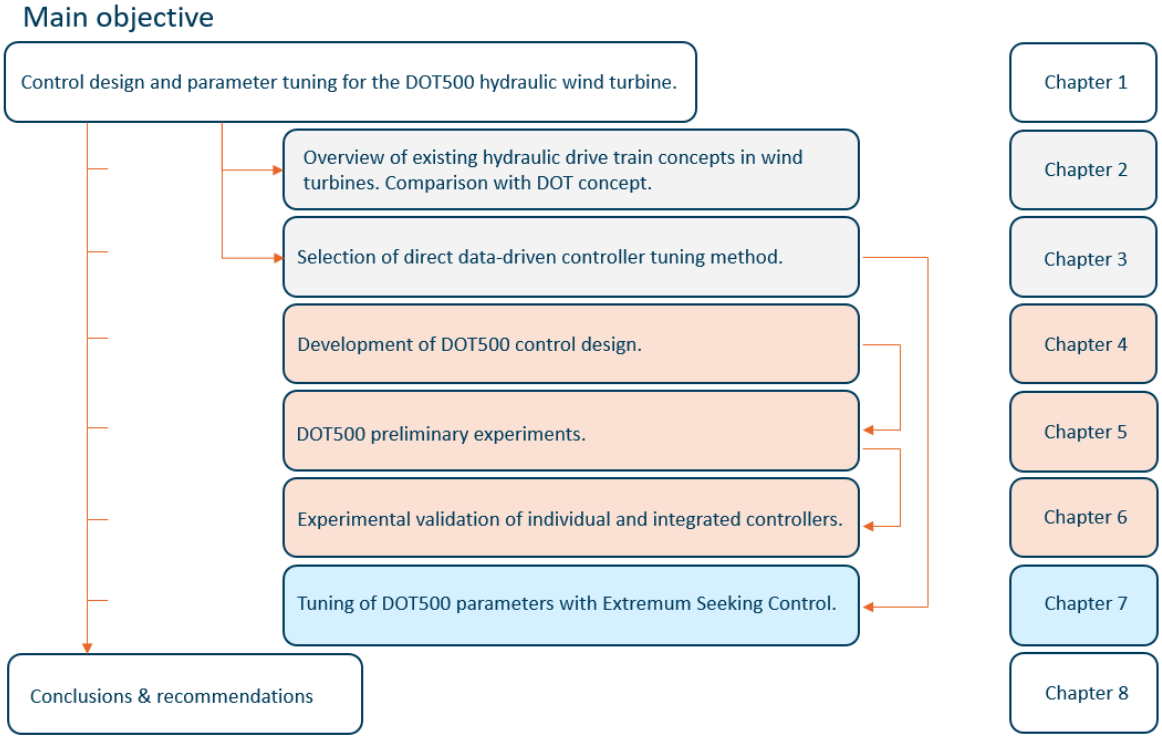

Figure 1-5: Flowchart of the structure of this thesis.

Chapter 2

Hydraulic drive trains in wind turbines

The objective of this chapter is to provide background information on the how and why hydraulic drive trains are used in wind turbines. Section 2-1 explains the turbine energy conversion principle and outlines the necessity to replace state-of-the-art wind turbine drive trains with robust hydraulics. Next, in Section 2-2, the working principle of hydraulic drive trains is explained. Section 2-3 gives a detailed overview of the developments in hydraulic wind turbines and Section 2-4 explains the novelty of the DOT concept. Finally, in Section 2-5, specifications of the DOT500 prototype are given.

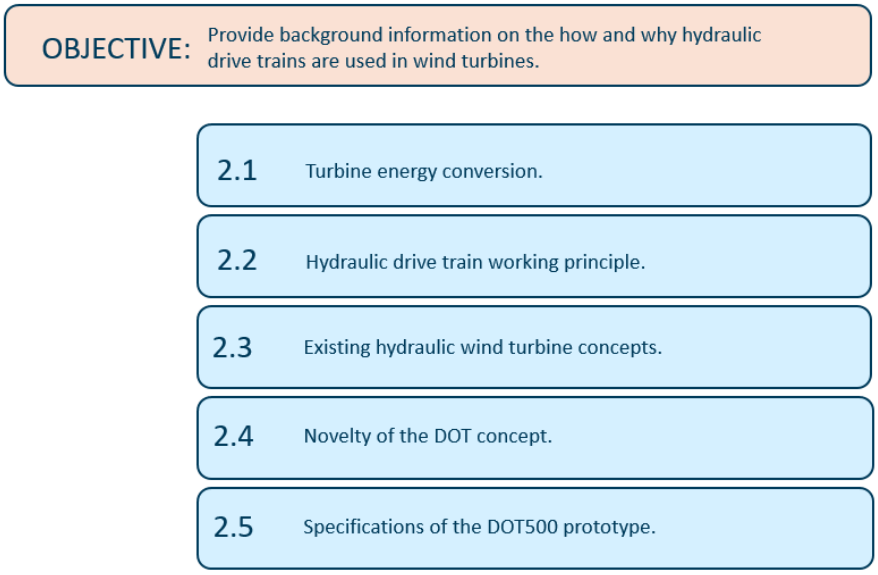

Figure 2-1: Chapter outline

.

2-1 Turbine energy conversion

The main goal of an offshore wind turbine is to convert aerodynamic power from wind into electrical power. This conversion is accomplished in two main stages. The primary energy conversion process occurs at the rotor, where aerodynamic power is converted into mechanical high-torque, low-speed power. The rotor shaft mechanical power is transformed into electricity in the second stage. The turbine energy conversion stages are schematically presented in Figure 2-2.

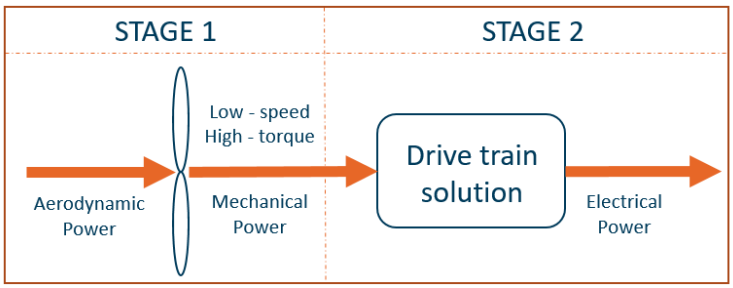

Figure 2-2: Schematic overview of the two stages in wind turbine energy conversion.

In this thesis, the second stage is of interest. DOT aims to redesign the way wind energy is converted to the electricity grid. This chapter outlines the use of a hydraulic drive train as an alternative to the state-of-the-art solutions that are mentioned hereafter. Hydraulics are widely used in the wind turbine industry, but only for active control purposes (like pitch and yaw actuators). Hydraulics were briefly considered for wind turbine drive train purposes in the early 1980s [3], but a lack of suitable components made their use unsuccessful. However, the industry has matured and nowadays hydraulics are considered as a robust and reliable way for power transmission purposes. Hydraulics therefore made their comeback in several turbine drive train concepts in the past decade and are considered as a promising alternative to state-of-the-art solutions.

State-of-the-art solutions

For the second stage, two main concepts are commercially applied in current wind turbines.

- **A mechanical gearbox coupled to a high-speed generator** is the most used configuration in offshore wind turbines. However, the gearbox has been singled out as a key source of high operation & maintenance (O&M) costs in offshore wind farms. The typical design lifetime of a turbine is 20 years, but gearboxes commonly fail within an operational period of 5 years [1, 4, 5]. A gearbox replacement can cost up to 10 percent of the original wind turbine installation costs [4]. Vibrations and asymmetric loading have caused components, mainly bearings, to break down sooner than expected [1]. Any misalignment in the transmission concentrates mechanical loads within the gearbox, hence requiring the underlying mechanical structure to be inherently rigid, which adds undesired weight to the transmission.

- The alternative solution used in onshore turbines is **direct drive technology** [1, 4, 6], where the rotor is directly coupled predominantly to a low-speed, high-torque generator and full size converter. This concept sets new references for drive train efficiencies and reliability onshore, mainly due to component reduction. Some trade-offs in terms of weight, cost and size became evident, but the market was willing to pay for them [7]. However, because of the current trend of increasing rotor size for offshore power maximization, the direct drive technique has been considered too bulky to install offshore in multi-MW turbine wind farms.

The main objective of any drive train is the transformation of power into a desired output power configuration. Transfer of power is commonly accomplished via mechanical, electrical and/or fluid power solutions [8]. The amount of intermediate stages is typically highly correlated with the overall efficiency and reliability of the turbine. The motivation to increase the rotational speed via a gearbox is to allow for smaller generators, since the required rotational speed at the generator increases linearly when the number of its poles decreases. The rotational speed of the rotor is limited by the airspeed experienced by the blade tips. The world's current biggest wind turbines have rotor speeds around 10 RPM and due to the current trend towards larger blades even lower rotor speeds are expected in the near future [9]. The expected size increase makes mass reduction and reliability of paramount importance to the system's economy [1].

2-2 Hydraulic drive train working principle

This section gives a short theoretical background on hydraulic drive trains. The aim is to provide sufficient background knowledge for the reader to be able to understand the concepts discussed in the next section. With this objective in mind, a classification of hydraulic drive trains is given in Figure 2-3. The individual components of this classification are discussed next.

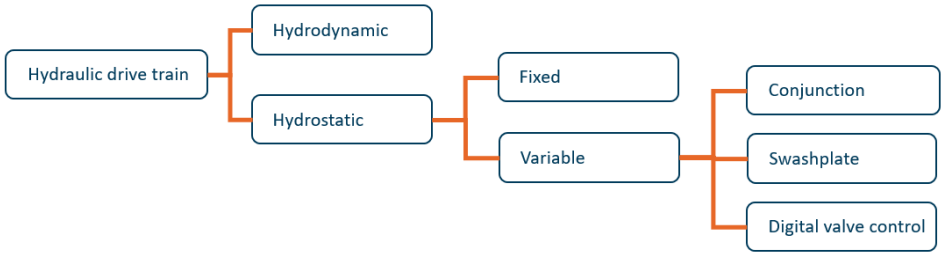

Figure 2-3: Classification of hydraulic drive trains.

Operating principle

Hydrodynamic transmissions operate at high rotational speeds to give and take kinetic energy from a fluid flow. In a hydrodynamic transmission, fluid is generally impelled by a centrifugal pump and harvested again by a turbine runner. There, it is reconverted into mechanical power, as shown in Figure 2-4. The intermediate fluid transports hydraulic energy

at high flow and low pressure. Hydrodynamic transmissions make it possible to regulate torque and are known for high efficiencies, but require high rotational speed at the input shaft. Due to the latter, hydrodynamic transmissions are not well suited to be directly connected to a wind turbine rotor. This type of transmission is however widely used for the transport of fluids.

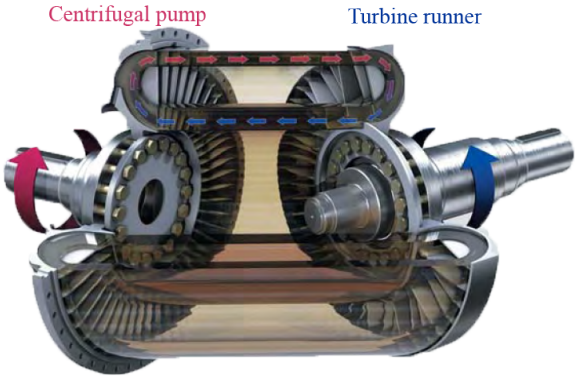

Figure 2-4: Hydrodynamic drive train energy conversion: the mechanical power introduced by a centrifugal pump is transmitted to a fluid, that transports it as hydraulic energy and forwards it to the turbine runner [10].

Hydrostatic transmissions are based on volume displacement and typically operate at low flow rates and high pressures. Using a hydraulic pump, the torque and rotational speed of the inlet shaft are transformed to fluid flow and pressure. As the pump shaft rotates, the positive volume of fluid is sealed from the inlet and transported to the outlet where it is subsequently discharged. A hydraulic motor converts the pressure and flow back into mechanical energy, with the desired torque and rotational speed (see also Figure 2-5). Systems that handle the largest force densities are normally from the hydrostatic type, with a radial or axial piston configuration [7].

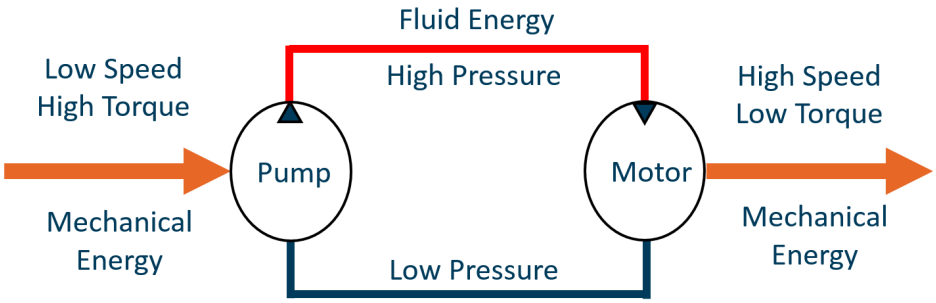

Figure 2-5: Hydrostatic drive train energy conversion. The pump transforms the torque and rotational speed of the inlet shaft into fluid flow and pressure. The motor converts the flow and pressure back into mechanical energy, with the desired torque and rotational speed.

Hydrostatic transmissions are widely recognized as excellent systems for power transmission when variable output velocity is required. There are many hydraulic power transmission applications with low speeds and high torques, such as excavators, but there is a lack of

suitable components for multi-MW drive trains required for wind turbines [1]. Nonetheless, developments in the last decades pushed towards renewed potential in the wind industry. Critical is the selection of the pump, which should match the rotor characteristics.

The pump required in the hydrostatic transmission is comprised of a lot of small hydraulic cylinders, so the redundancy of cylinders enables high availability to be maintained if some cylinders fail. Also, total replacement is not required in case of failure since the hydraulic components are partially exchangeable. Moreover, if larger capacity is required, the modular design concept enables easier scale-up in shorter time and at lower development costs [11].

Fixed vs variable transmission

In the hydrostatic configuration, a further distinction can be made between fixed and variable transmissions, as shown in Figure 2-3. If the displacement volumes of both pump and motor are fixed, the hydrostatic transmission simply acts as a gearbox with fixed gear ratio. A fixed displacement pump has a predefined flow rate, hence in the ideal situation every stroke of the pump moves the same amount of fluid. Control can only be performed through an external flow control circuit, fluid properties, or by the mechanical power at the shaft. However, when the pump works at power levels below its rated capabilities, at partial load, reduced efficiencies are generally obtained.

The phenomenon of reduced efficiency at partial load is typically avoided by using either multiple pump configurations or by variable displacement pumps, where the flow rate configurations can be changed as the pump operates. Pumps with variable displacement allow the operator to vary the fluid displaced per revolution of the pump. This can be done either mechanically using swash plates or by (digitally) enabling/ disabling individual cylinder valves.

However, no matter how compact and robust they may be, state-of-the-art hydrostatic transmissions suffer from reduced efficiency at partial load and displacement volumes different from the nominal value [12]. The interest for applications of this type of transmission in wind turbines is mainly related to the potential increase of reliability and reduction of maintenance costs in spite of an expected reduction of overall efficiency [12].

Decoupling

Hydraulic drive trains allow for complete mechanical decoupling of the rotor from the generator. The characteristics of each can be optimized without concern for the torsional dynamics of the drive shaft. This produces a substantial increase in expected lifetime, since accuracy of alignment of the power train is less critical [13]. The decoupling in variable hydraulic transmissions is often used to maintain constant generator speed, which allows a synchronous generator directly to the grid.

2-3 Existing hydraulic wind turbine concepts

The first hydraulic wind turbines have emerged as a response to the oil crises in the 1970s. Over the past decades there have been a number of research projects investigating the use of hydraulics in the wind turbine drive train to replace the gearbox and electrical converters. These research projects have led to prototypes being produced and major wind turbine manufacturers acquiring some of the hydraulic technologies developed. This section provides an overview of the developments in the industry.

Bendix SWT-3 Already in the early eighties the Bendix SWT-3 concept (Figure 2-6) incorporated a hydraulic drive train into a 3MW wind turbine in the San Giorgino Pass, USA [3]. This concept included a mechanical gearbox that was driving a hydrostatic transmission, which consisted of fourteen fixed displacement pumps in the nacelle operating in conjunction with eighteen variable displacement motors at the tower base (Figure 2-7).

Figure 2-6: Bendix SWT-3 turbine, 1980 [7]

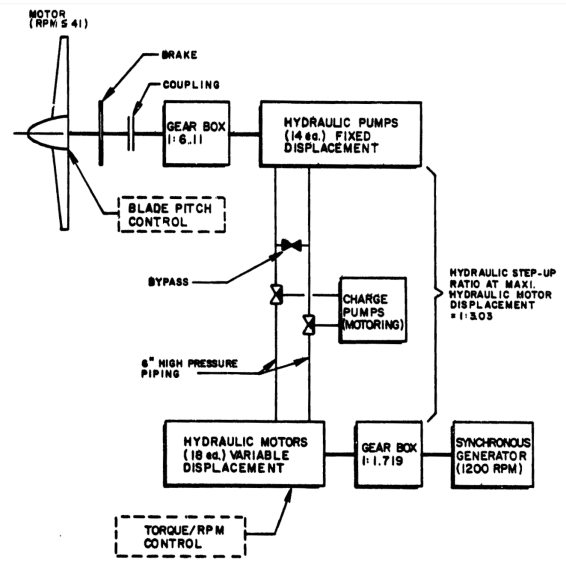

Figure 2-7: Original schematic diagram of Bendix SWT-3 drive train [3]

The fourteen fixed displacement pumps were sequentially activated in such a way that only one out of fourteen was working at partial load. The motor displacements were varied in order to vary the effective gear ratio accordingly. The transmission was then led through a second mechanical gearbox to a low voltage electrically excited synchronous generator, which in turn was connected to a step-up transformer that was directly connected to the grid. The generator, step-up transformer and yaw system were all located at the base of the rigid triangular tower truss configuration. Three charge pumps supplied fluid from a reservoir to the low-pressure side of the fixed displacement pumps. In terms of control, it was provided with full blade pitch and yaw control, which was controlled via a microprocessor.

Although the feasibility of a hydraulic drive train in wind turbines was proven, it may not come as a surprise that the extensive list of drive train components made the overall system

overly complex and therefore inefficient. That, in combination with the end of the oil crisis, was the reason why the turbine was taken apart several years after construction.

Orbital2 Ltd. At the other side of the Atlantic Ocean, on the Orkney Islands in Britain, another hydraulic turbine concept arose in 1982 as a potential solution to the oil crisis. The Orkney LS1 was a 2 bladed, 3MW wind turbine on a concrete tower as shown in Figure 2-8. The drive train of the Orkney LS1 laid the foundation for the hybrid variable ratio transmissions category.

Figure 2-8: Orkney LS1 wind turbine with concrete tower, 1982 [14]

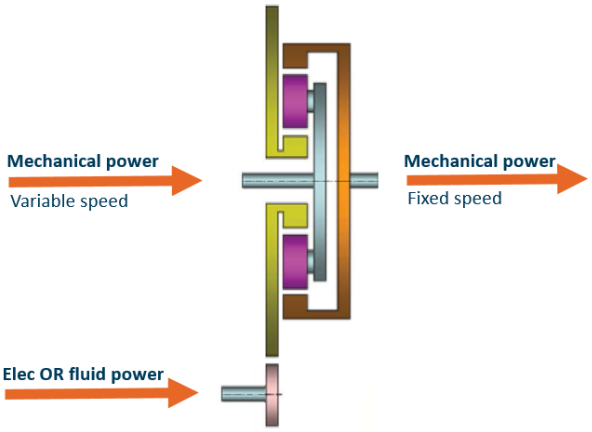

Figure 2-9: Super Positioned Gear (SPG), with input carrier in blue, sun wheel in purple and output annulus in orange [7].

The LS1 consisted of a mechanical gearbox and an electrical reaction motor, both connected to a by Hicks [15] patented Super Positioned Gear (SPG) as shown on the left of Figure 2-9. The gearbox is connected to the input carrier of the differential and the electrical reaction motor to the sun wheel. On the right in Figure 2-9, the generator is connected to the annulus of the SPG.

The SPG technology led to the company Orbital2 Ltd. and was in 2006 licensed to Wikov Wind, a Czech wind turbine manufacturer. Wikov Wind replaced the electrical reaction motor at the sun wheel with a hydrostatic transmission in their Wikov W2000 2MW turbine.

The mechanical input power from the turbine rotor shaft is split by a parallel shaft. The largest part is passed through the mechanical gearbox to the SPG input carrier, whereas a smaller part is now passed through the hydrostatic transmission to the sun wheel. When a wind gust increases the torque on the parallel shaft, the variable hydrostatic transmission is adjusted such that the generator speed remains constant. This enables variable rotor speed while maintaining constant speed of the generator shaft. As a result a high voltage electrically excited synchronous generator can be directly connected to the grid.

The Orbital2 method is used commercially in a wide variety of multi-MW turbines all over the world, up to 5MW turbines in China. Nonetheless, W2000 SPG is still a geared transmission that makes use of a hydrostatic transmission to control a secondary set of mechanical gears.

WinDrive The WinDrive concept from the German company Voith is based on a hydrodynamic transmission torque converter, where turbines give and take energy from an oil flow. The concept was conceived in 2003, and in 2005 Voith partnered with the company DeWind for the development of their first 2 MW prototype turbine.

The WinDrive technology can be considered a variable-speed hydrodynamic gearbox that is located between the main gearbox and the electrical generator (see Figure 2-10). The WinDrive converts the wind turbine rotor's speed into a constant speed for the generator. It replaces the power electronic converter and step up transformer functions by making it possible to fit a high voltage electrically excited synchronous generator. It can even be used as an upgrade for conventional drive train systems.

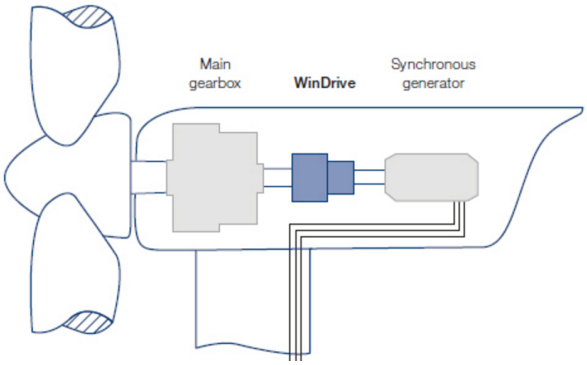

Figure 2-10: Placing of WinDrive between the mechanical gearbox and synchronous generator [16]

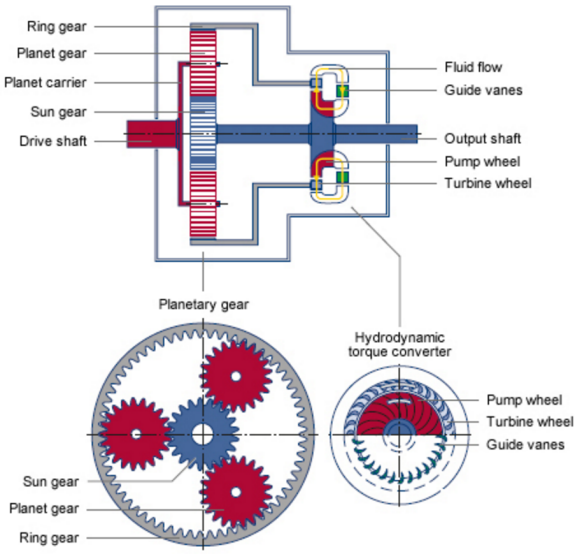

Figure 2-11: WinDrive variable-speed hydrodynamic gearbox overview [16]

The WinDrive variable-speed hydrodynamic gearbox (Figure 2-11) uses a planetary gear set to split the power input in two sections. The first transmits the major portion of the power directly through a fixed ratio rotating output shaft to the generator. The second uses hydrodynamic fluid power through a torque converter, which diverts only a small fraction of the overall power. This diverted power is fed back to the planetary gear through the ring gear. The planetary gear combines the power from the wind rotor with the adjustable power fed back through the ring gear to then drive the sun gear at a constant speed. This increases the effective torque of the output shaft, reduces mechanical stresses in the main gearbox and provides additional damping.

The company built several more 2MW prototypes in 2008, placed in Texas, USA and even at 4300m altitude in Argentina. The Voith WinDrive then proved to be commercially successful, as it was later installed in several wind farms in both the USA and Canada.

As in the Orbital2 method, the product is an addition to the existing main gearbox instead of a replacement. The main difference between the two concepts is the use of a hydrodynamic implementation in the Windrive concept versus the Orbital2 hydrostatic transmission.

Artemis Intelligent Power Artemis is a spin-off company from a research group at the University of Edinburgh which initially focused on wave energy converters. Already in 1984, Artemis co-founder Professor Stephen Salter mentioned the potential of hydraulics for wind turbines [13]. The company has developed since then a high efficient hydraulic pump/motor combination by means of computer controlled high speed valves.

In conventional variable displacement machines, such as an axial swash plate pump, no means are provided to regulate the flow of the fluid that leaves the individual cylinders. It is left to a hydraulically or mechanically driven swash plate to adjust the stroke of all the pistons together and hence control the amount of displacement that the pump provides. However, efficiency and power losses are inevitable at displacement levels different from the nominal value.

In contrast, the Artemis Digital Displacement pump controls solenoid valves associated with each individual cylinder by a small computer driven, electro-magnetic latch. The displacement of a pump, or the speed of a motor, is accurately controlled by opening or closing the valves associated with each cylinder on each stroke. This overcomes operation at partial load, resulting in high efficiencies over the complete range of operation (see Figure 2-12). In wind energy applications, where the average load on a system is 30 percent of the peak power, that part-load efficiency is critical. The obtained efficiencies are comparable to those of current wind turbine transmissions and the technique is widely regarded as potentially revolutionary for fluid power drives.

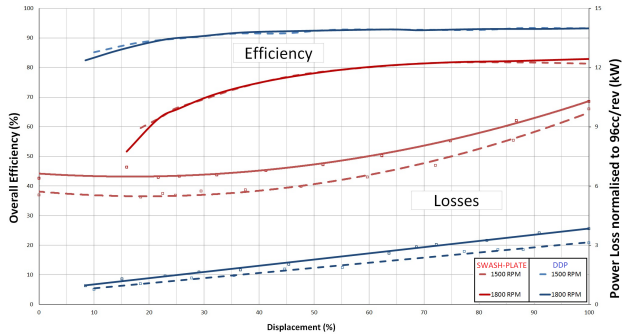

Figure 2-12: Typical efficiency and power loss comparison between Digital Displacement pump (blue) and swash-plate pump (red) indicates higher partial load efficiency for the first [17].

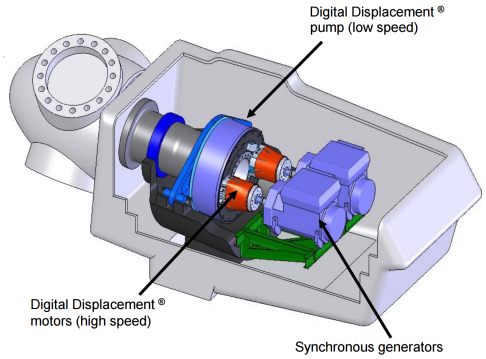

Figure 2-13: Impression of Artemis Digital Displacement system [17]

The Digital Displacement system relies entirely on software to implement pump and motoring function and even braking. It has a 30 ms response time to setpoint changes, independent of pressure. The variable ratio transmission takes care of angular speed regulation and is directly linked to a synchronous generator (see Figure 2-13). This makes it easier to meet grid requirements. In 2009 Artemis reported laboratory results for their 1.6MW test bench prototype. The hydrostatic transmission integrates a 1.6MW Digital Displacement pump and the output fluid drives two 800kW hydraulic motors that can work independently and are coupled to high speed synchronous generators.

In December 2010 Artemis Intelligent Power was acquired by the wind turbine manufacturing division of Mitsubishi Heavy Industries Ltd. Together, both companies worked on several Digital Displacement Transmission (DDT) prototype wind turbines, including the SeaAngel

7MW turbine (see Figure 2-15). The drive train consists of a 7MW hydraulic pump and two 3.5MW hydraulic motors, in the same configuration as depicted in Figure 2-13. Feasibility of the transmission was first proven on a 7MW test bench in [11], which is shown in Figure 2-14.

The SeaAngel is placed at the Hunterston, Schotland, test site in 2014, and is the largest capacity hydrostatic transmission currently built. The company claims that the heaviest component in the DDT system is just 25kg, and states that most of the parts are small enough to be carried by an individual technician [18].

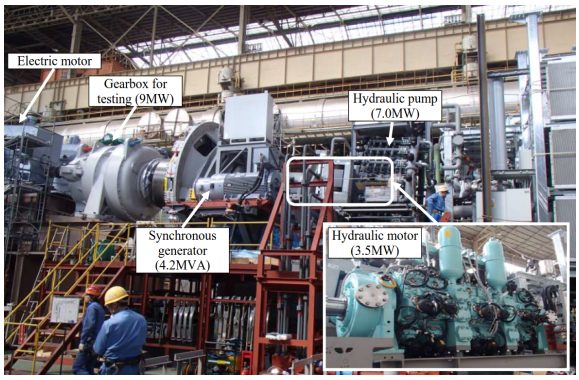

Figure 2-14: 7MW test bench [11]

Figure 2-15: 7MW SeaAngel nacelle [18]

Mitsubishi Heavy Industries Ltd and Vestas Wind Systems A/S joined forces in 2014 and decided to concentrate its future offshore turbine efforts in the MHI Vestas joint venture rather than across two platforms. Mitsubishi has abandoned plans to develop its 7MW SeaAngel offshore wind turbine as a commercial product and will instead focus on development of its hydraulic drive as a standalone component [19]. The joint venture is currently working on the MHI Vestas V164-8MW turbine.

ChapDrive AS The Norwegian company ChapDrive AS is a spin-off company from the Norwegian University of Science and Technology (NTNU) in Trondheim, Norway. It was originated in 2004 as a proposition to floating offshore structures. ChapDrive developed a hydraulic drive train solution for wind turbines that serves to reduce top weight, eliminate the mechanical gearbox and reduce cost of energy compared to conventional wind turbines. Several full scale prototypes were built.

The core technology is a hydraulic transmission with a variable speed control system (Figure 2-16). A fixed displacement pump is attached to the rotor shaft and pumps oil directly from the reservoir to the variable displacement motor. The motor is intended to maintain a constant speed due to fast displacement control by digital valve control. The motor is directly coupled to a synchronous high voltage generator, eliminating the need for a mechanical gearbox, frequency converter, permanent magnets and a voltage transformer. The transmissions allows variable speed control, reduction of power fluctuations and grid stabilization.

The original idea was further characterized by relocating the majority of the critical components from the nacelle in the top of the turbine down to a power unit at the foundation. This would reduce the top weight significantly and simplifies service access. This configuration is also used at DOT. Nonetheless in 2010, ChapDrive diverted from their initial idea of having

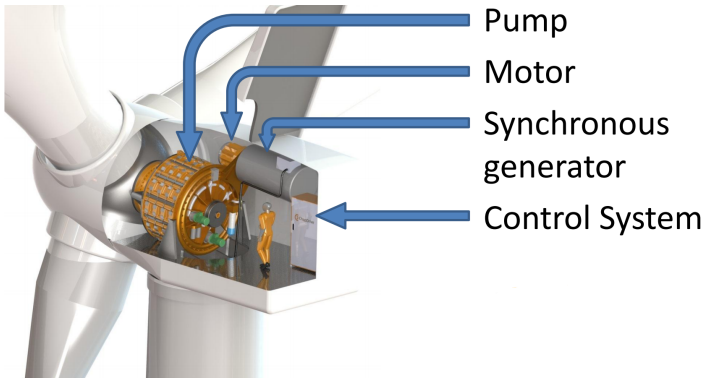

Figure 2-16: Chapdrive prototype design [20]. The fixed displacement pump is attached to the rotor shaft and pumps oil directly from the reservoir to the variable displacement motor. Motor and generator remain at constant speed due to digital valve control.

the generator at ground level and placed it in the nacelle as depicted in Figure 2-16. Although ChapDrive made successful 50kW (2005), 300kW (2006) and 900kW (2008) prototypes in the past and secured sufficient funding from Statoil for their 5MW concept in 2010, the company is no longer in business.

The Statoil/Hägglunds two-speed concept Statoil and the hydraulic motor company Hägglunds proposed in 2011 a two-speed hydraulic concept that allows for a discrete hydraulic gear ratio by switching hydraulic motors on and off depending on the current operating point [21, 22]. In this way, only a single motor is working at partial load for all operating conditions. The reasoning is that current variable displacement motors are less efficient at partial load. The proposed solution implies that the aerodynamic efficiency would be somewhat reduced, but the improved hydraulic efficiency leads to an increased overall efficiency compared with other hydraulic transmission concepts. A 5MW turbine modelling study was presented in 2012, using a set of six fixed displacement radial piston hydraulic motors in conjunction [22]. A simplified schematic overview of the Statoil concept is shown in Figure 2-17.

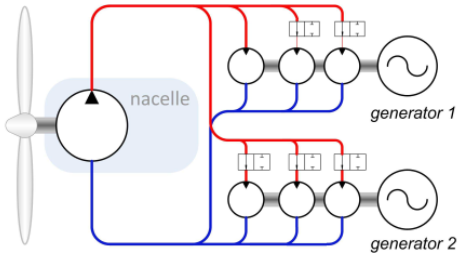

Figure 2-17: The Statoil concept with six fixed displacement motors in conjunction [1]

Statoil made several other significant investments in the offshore wind industry, including their recent Hywind project to build the first floating wind farm off the Scottish coast. The 30MW pilot project will consist of five 6MW floating turbines operating in waters exceeding 100m of depth and construction is planned in 2017 [23]. A world's first floating full-scale wind turbine Hywind demo was installed in 2009. The incorporation of a hydraulic drive train into a floating wind turbine would be particularly interesting due to the expected mass reduction.

IFAS - 1MW test bench The Institute for Fluid Power Drives and Controls (IFAS) at Aachen University in Germany developed a 1MW hydraulic drive train for wind turbines (see Figure 2-18). The idea behind the concept is similar to the Statoil concept, with multiple motors in conjunction, but uses variable displacement motors and a second pump (see Figure 2-19). Each component, except for the smallest pump, can be switched to idle mode, which allows different pump-motor combinations for different operating points. The 1MW test bench allows real time simulation of the different components both in static and dynamic operating conditions. For more details regarding the system and test bench the reader is referred to [1, 24, 25, 26].

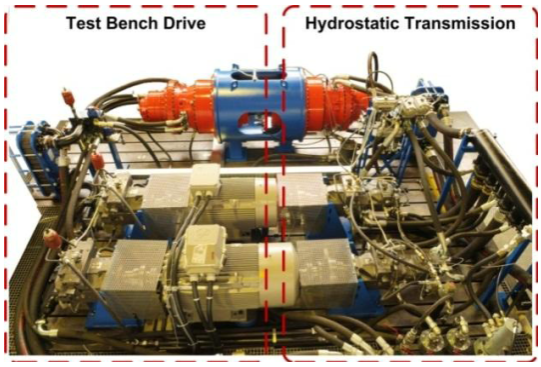

Figure 2-18: IFAS 1MW test bench [1]

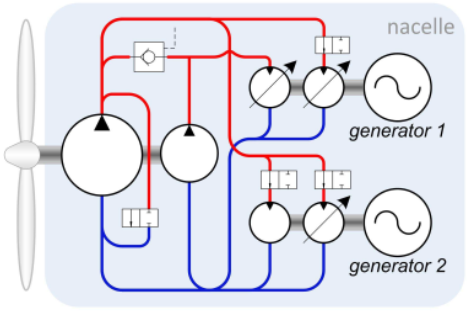

Figure 2-19: The IFAS concept [1] with two pumps and four variable displacement motors in conjuction.

2-4 Novelty of the DOT concept

This section outlines the novelty of the DOT concept. First the advantages of the hydraulic drive train with respect to current commercial wind turbines are summarized. Second, the novelty with respect to the drive train concepts that were discussed in the previous section is explained.

Replacement of a gearbox by a hydraulic transmission has a number of advantages. Hydraulic transmissions are known for their redundancy and have a proven track record in a wide variety of industries. Due to their high torque to weight ratio, mass reduction of the nacelle can be accomplished. The nacelle mass can be further decreased by bringing the hydraulic motor and generator down to foundation level. The gearbox, generator and converter in the nacelle are then replaced by only a hydraulic pump. These mass reductions have a positive effect on the dimensioning of the support structure design, resulting in an overall reduced mass. Moreover, hydraulic drive trains can be made continuously variable. This allows the use of a synchronous generator directly connected to the grid, without the need of a converter, due to the decoupling of generator speed from rotor speed. Finally, hydraulic transmissions add desired damping to the load shaft and transmission.

Mentioned advantages should outweigh these of traditional gearbox usage, which are known for their high efficiency but also for their high failure rates and maintenance costs. The

main disadvantage of hydraulic transmissions is its reduced efficiency at partial load and displacement volume different from the nominal value. However, cost reductions are expected to outbalance this disadvantage over the turbine lifetime. The use of water hydraulics in the DOT concept, instead of oil, reduces the risk of pollution and obviates the need of a return line from the hydro-power station to the turbines.

The discussed WinDrive torque converter concept is of the hydrodynamic type, which make use of a spinning body to give and take kinetic energy from a fluid flow. Since hydrodynamic transmissions require high speed at the input shaft, most other discussed concepts are of the hydrostatic type, based on volume displacement, which typically operate at low flow rates and high pressure. For the same reason DOT concept uses an hydrostatic transmission between pump and spear valve. However, the fluid power transmission between spear valve and Pelton wheel is of the hydrodynamic type.

Hydrostatic transmissions can be fixed or variable displacement. The ratio of fixed displacement transmissions is only dependent on the fluid properties and mechanical power input. Variable displacement transmissions allow, in addition, fluid flow control. This can be done by adjustable swash plates in pump and/or motor, or by digitally deactivation of individual pressure chambers. The latter, an Artemis invention, is considered as a promising solution to the partial load problem. Finally, as in both the Bendix and Statoil/Hägglunds two-speed concept, variable displacement can be achieved by using multiple pump/rotor combinations in conjunction.

Current concepts prove the feasibility of hydraulic transmissions in wind turbines. The DOT concept, described in Section 1-1, takes an important step further by taking the hydraulic motor and generator down to sea level. This concept was also mentioned by Chapdrive, but they never built it on full scale. The improved accessibility, in contrast to the nacelle based critical components in current turbines, reduces maintenance costs. Moreover, the use of only a single generator at the hydro-power station further reduces the amount of critical components and copper usage.

Another important new aspect of the DOT concept is the use of spear valves to control the fluid properties. This novelty leads to the mechanical decoupling between generator and spear valve, hence allowing separate optimization of turbine and generator control. However, decoupling also requires an alternative torque control implementation where fluid pressure is regulated to vary the system torque. This is an alternative solution to the one discussed in [27], where the system torque is controlled by the swash-plate of a variable displacement pump and the spear valves are only varied to maintain constant pressure in the high-pressure water line in the above-rated region. The same research group proposes to use sea water in an additional heat exchanger to increase the overall DOT efficiency [28].

The most innovative part of the DOT concept is the integrated wind farm design approach. Individual DOT turbines are not necessarily more efficient, but the slender and robust design should ultimately lead to lower construction, operation and maintenance costs of future wind farms. However, a prototype of a single DOT turbine was build first to prove its feasibility. Specifications of the DOT500 prototype are discussed in the next section.

2-5 Specifications of DOT500 prototype

This section describes the DOT500 prototype, which is considered in the sequel of this thesis. Note that this prototype uses the turbine tower structure, nacelle and rotor of a second-hand Vestas V44 turbine. The drive train of the V44 is retrofitted with the DOT intermediate concept. Specifications of the original Vestas V44 turbine are given in Table 2-1.

Parameter	Value
Manufacturer, model	Vestas V44
Nominal power	600 kW
Rated rotor speed	28 RPM
Optimal tip-speed ratio / power coefficient	7.55 / 0.43
Gearbox ratio	1 : 52.8
Rotor diameter	44 m
Number of blades	3
Total weight	87000 kg

Table 2-1: Original Vestas V44 specifications [29]

The DOT500 prototype is shown in Figure 2-20 and schematically depicted in Figure 2-21. The intermediate oil loop serves as a hydraulic gearbox between the rotor and water pump. This oil loop will be omitted in the final DOT concept, where the water pump is directly attached to the rotor shaft, as explained in Chapter 1.

Figure 2-20: Photo display of DOT500 test set-up during prototype testing.

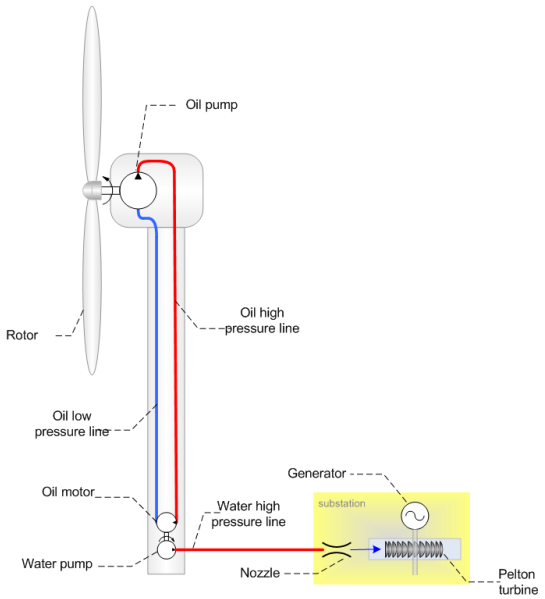

Figure 2-21: Overview of DOT500 test set-up with integrated oil loop [1].

The rotor of the DOT500 prototype drives the Hägglunds CB840 oil pump (see Figure 2-22).

(a) Nacelle top view

(b) Nacelle back view

Figure 2-22: Photos of the DOT500 Nacelle. Located central in the middle is the blue hydraulic pitch cylinder, linked to the grey link push rod, which goes through the red Hägglunds CB840 oil pump to the pitch traverse in the hub. The pump is attached to the turbine rotor shaft.

The pressurized oil flow then drives the Rexroth A6VLM oil motor, which is placed in the tower at access platform height, by means of a hydrostatic transmission. The displacement volumes of both pump and motor are fixed, hence the hydrostatic transmission acts as a hydraulic gearbox with fixed gear ratio. The oil motor is mechanically coupled to the Kamat water pump, which pressurizes the water inlet flow (see Figure 2-24).

The high-pressure water line is controlled by two adjustable spear valves, which transmit the fluid power to the Turbogen Pelton turbine by means of a hydrodynamic transmission. Finally, a Motec 400kW electro-motor, mechanically connected to the Pelton turbine, is used as an electrical generator (configuration overview shown in Figure 2-23 and located at ground level in the bottom-left corner of Figure 2-20).

Figure 2-23: Mechanically coupled Pelton turbine and generator. The two variable spear valves are pointed towards the Pelton turbine buckets (located in the white housing).

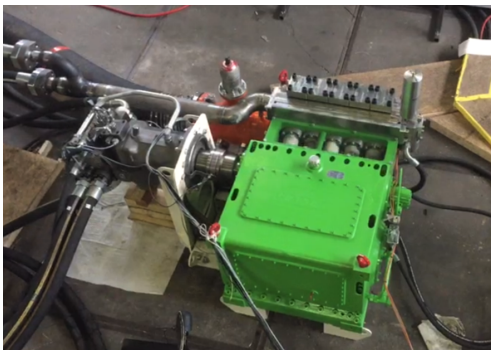

Figure 2-24: Left the Rexroth oil motor, mechanically coupled to the Kamat water pump (green) which pressurizes the water inlet flow.

The DOT500 uses the original Vestas V44 collective blade-pitch mechanism, to keep the blades in fine-pitch position at below-rated wind speeds and to turn the blades in the correct position at above-rated wind speeds. A hydraulic cylinder assembly, mounted to the nacelle

frame (see Figure 2-22), is connected to a link push rod, going through the middle of the Hägglunds pump. On the rotor side, the push rod is mechanically attached to the pitch traverse of the rotor blades. The unidirectional movement of the hydraulic cylinder pushes the traverse (see Figure 2-25), which translates the unidirectional movement into rotation of all three rotor blades (see Figure 2-26).

Figure 2-25: Original Vestas V44 hub, with in the middle the triangular pitch traverse.

Figure 2-26: Blade-to-hub bearing, with below the traverse connection link.

Finally, a yaw orientation system is used to keep the DOT500 rotor aligned with the dominant wind direction. The primary component is a large bearing that connects the nacelle frame to the tower. Two yaw motors drive pinion gears against a bull gear attached to the yaw bearing (see Figure 2-27, showing one of the two motors).

Figure 2-27: One of the two yaw motors driving the small pinion gear against the large bull gear of the bearing, which connects the nacelle frame to the tower.

Chapter 3

Direct data-driven controller optimization

This chapter serves as a study on the practical applicability of data-driven controller optimization algorithms. First in Section 3-1, the motivation for data-driven tuning is outlined, as opposed to model-based techniques. Then, in Section 3-2, the following three data-driven methods are elaborated: Iterative Feedback Tuning (IFT), Virtual Reference Feedback Tuning (VRFT) and Extremum Seeking Control (ESC). Finally, in Section 3-3, the potential applicability of these methods to the DOT500 turbine is discussed.

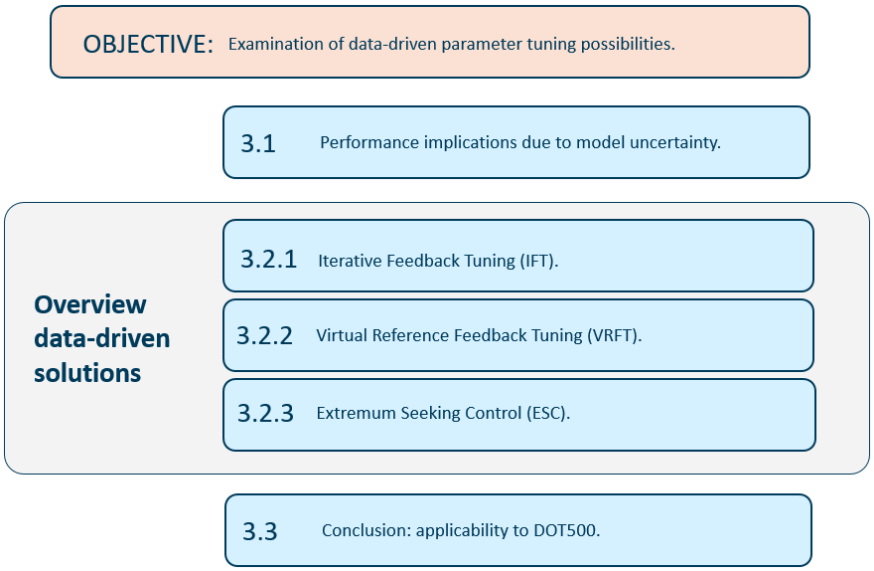

Figure 3-1: Chapter outline

.

3-1 Performance implications of model-based control

Current industry-standard wind turbine control designs still heavily rely on detailed first-principles modelling [30]. Linear control-oriented models are generally obtained from high-fidelity wind turbine simulation first-principle software packages, which approximate the non-linear wind turbine dynamics in the vicinity of selected operating points. The linear model is used to design a controller, of which the closed-loop performance is evaluated on the high-fidelity model. The use of a first-principles model, however, directly implies that there are modelling errors and therefore differences with the real world wind turbine dynamics of interest. The controller performance is highly dependent on this modelling accuracy. An experimental study conducted by the US National Renewable Energy Laboratory (NREL) reported large discrepancies between computational modelling results and the actual measurements on turbines [31].

An alternative to first-principles modelling is the use of system identification techniques, where a control-oriented model is derived from wind turbine input/output experiment data. In this way the collected set of data is used to identify a model, which is subsequently used to design a controller. A major drawback of this approach is that it might be time consuming and complicated to obtain the dynamics for all operating conditions. Currently, system identification is rarely used in the wind energy industry, but recently several major manufacturers have performed studies to determine the potential for system identification in their control approaches [32]. It is to be expected that once multivariable and multi-objective control design becomes commonplace, the need for accurate and refined models will increase [32].

As for the first-principles case, the identification methods remain a model-based approach, where the controller is calculated in a second step using the derived model. Several factors deteriorate the controller performance once implemented on the actual turbine [33]. First, the performance of the controller is limited by the general mismatch between the model and the real turbine. Second, the real-world turbine will deviate from the specifications due to for instance manufacturing errors and imperfections [32]. Third, due to manufacturing and other environmental differences such as varying soil dynamics throughout a wind plant, dynamics vary among turbines. Fourth, due to wear and tear dynamics will change over time. Finally, in many practical control applications, a mathematical description of the plant is not available or too costly and time-consuming to obtain.

3-2 Overview of 3 direct data-driven solutions

In recent years, several data-driven techniques have been proposed as an alternative to the model-based approaches described in the previous section. In a data-driven approach, the modelling step is omitted and the problem of undermodelling of the plant is avoided. Instead, measured data is used directly to minimize a control criterion. This concept has attracted the attention of control engineers since the forties with the pioneering work by Ziegler and Nichols [34], which focuses on the design of industrial PID controllers. Since there is no intermediate model, the structure of the designed controller does not depend on the structure of this model, and the order and structure of the controller are fixed [35]. This led to the development of new powerful methods for direct controller tuning.

In this overview three methods are discussed that use this data-driven controller tuning approach. First, in Section 3-2-1, the concept of Iterative Feedback Tuning (IFT) is explained. Subsequently, in Section 3-2-2, Virtual Reference Feedback Tuning (VRFT) is outlined, followed by Extremum Seeking Control (ESC) in Section 3-2-3. Each of the methods is introduced with a brief introduction, followed by a simplified description of the algorithms. Then extensions to more complex systems are discussed and each section finishes with several applications of the described method. Finally, in Section 3-3, the applicability of these concepts to the DOT project is discussed.

3-2-1 Iterative Feedback Tuning (IFT)

Iterative Feedback Tuning (IFT) was first proposed by Hjalmarsson et al. in [36]. There it was observed that the earlier described model bias problem could be avoided by replacing the information carried by the model by information obtained directly from the system itself. This led to an iterative scheme where the fixed-structure controller parameters were successively updated, using information from special defined closed-loop experiments with the most recent controller in the loop. A control objective is minimized using a gradient search approach to find a local optimum, with an initial stable controller as a starting point. The method relies on a specific selection of system inputs, in such a way that the gradient of the cost function with respect to the control parameters are estimated from the corresponding measured closed-loop experiments.

Implementation

The overview in [37] is used to explain the basics of the IFT framework, using an unknown Single-Input Single-Output (SISO) linear time-invariant (LTI) system described by

$$y(t,\rho) = Pu(t,\rho) + v(t), \tag{3-1}$$
$$u(t,\rho) = C(\rho)\left(r(t) - y(t,\rho)\right), \tag{3-2}$$

where P is an unknown LTI operator, $r(t)$ the reference input, $v(t)$ an unmeasurable noise disturbance, $u(t,\rho)$ the process input and $y(t,\rho)$ the corresponding process output. $C(\rho)$ represents a fixed-structure controller, parametrized by the parameter vector ρ. See also Figure 3-2 for a schematic overview of this closed-loop system representation.

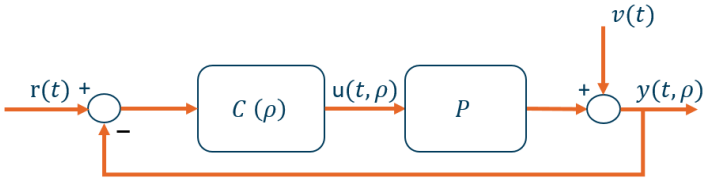

Figure 3-2: Closed-loop representation of the described system. $r(t)$ is the reference input, $v(t)$ an unmeasurable noise disturbance, $u(t,\rho)$ the process input and $y(t,\rho)$ the process output.

Minimizing the cost function

Now let y_d be the desirable output response to the reference signal $r(t)$. The error between the achieved and desired response is formulated as

$$\tilde{y}(t,\rho) \quad = \quad y(t,\rho) - y_d. \tag{3-3}$$

It is desirable to minimize some norm of this error quantity $\tilde{y}(t,\rho)$ with respect to the control parameter vector ρ. In this section, for reasons of simplicity, a quadratic norm function is used that is described by

$$J(\rho) = \frac{1}{2N} \sum_{t=1}^{N} E\left[\tilde{y}(t,\rho)\right]^2, \tag{3-4}$$

where $E\left[...\right]$ denotes the expectation w.r.t. the disturbance $v(t)$. Notice, however, that the discussion below is valid for basically any signal-based objective function defined by the user, and the quadratic norm of the input signal is often included in a second term. Some alternatives are discussed in [37]. The optimal set of control parameters ρ^* minimizing the described cost function $J(\rho)$ is defined by

$$\rho^* = \arg\min_{\rho} J(\rho). \tag{3-5}$$

Gradient estimation

The optimal set of control parameters is obtained by taking repeated steps in a gradient descent direction with the initial controller as starting point. This is done by using a local gradient based search algorithm of the type

$$\rho_{i+1} = \rho_i - \gamma_i R_i^{-1} \frac{\partial J}{\partial \rho}(\rho_i), \tag{3-6}$$

where i is the iteration number and γ the step size of the algorithm, which is a positive scalar and may vary after each iteration to improve speed of convergence. R_i is some appropriate positive definite matrix, typically an estimate of the Hessian of J, such as a Gauss-Newton approximation of this Hessian. Especially when $\tilde{y}$ is small,

$$R_i = \frac{1}{N} \sum_{t=1}^{N} \left[\widehat{\frac{\partial \tilde{y}}{\partial \rho}}(t,\rho_i) \widehat{\frac{\partial \tilde{y}}{\partial \rho}}^T(t,\rho_i) \right], \tag{3-7}$$

is a desirable choice. The minimization problem now boils down to computing the partial derivative of the cost function with respect to the control parameter vector ρ,

$$\frac{\partial J}{\partial \rho}(\rho_i) = \frac{1}{N}\sum_{t=1}^{N} E\left[\tilde{y}(t,\rho_i)\frac{\partial \tilde{y}}{\partial \rho}(t,\rho_i)\right]. \tag{3-8}$$

Hence, to find the optimal parameter vector ρ, the following quantities are required

1. the signal $\tilde{y}(t,\rho_i)$,
2. the gradient $\partial\tilde{y}/\partial\rho(t,\rho_i)$.

Experiment design

The signal $\tilde{y}(t,\rho_i)$ can easily be obtained only by measuring the output of the closed-loop system when the reference $r(t)$ is exciting the system and subsequently subtracting the desired response y_d from the measured output. Note also, from Equation 3-3 and the fact that the desired response y_d is independent of the parameter vector ρ, that the required gradient is equal to the gradient $\partial y/\partial\rho(t,\rho_i)$. Hence, with the use of Equation 3-3, 3-1 and 3-2 subsequently,

$$\begin{aligned}
\frac{\partial \tilde{y}}{\partial \rho}(t,\rho_i) &= \frac{\partial y}{\partial \rho}(t,\rho_i), && (3\text{-}9)\\
&= P\frac{\partial u}{\partial \rho}(t,\rho_i), && (3\text{-}10)\\
&= P\frac{\partial C}{\partial \rho}(\rho_i)(r(t)-y(t,\rho_i)) - PC(\rho_i)\frac{\partial y}{\partial \rho}(t,\rho_i). && (3\text{-}11)
\end{aligned}$$

Rewriting and defining the sensitivity function $S(\rho_i) = (I + PC(\rho_i))^{-1}$ results in

$$\frac{\partial y}{\partial \rho}(t,\rho_i) = S(\rho_i)P\frac{\partial C}{\partial \rho}(\rho_i)(r(t)-y(t,\rho_i)). \tag{3-12}$$

An estimate of this partial derivative is obtained by adding $r_1(t) - y_1(t,\rho)$ of the first experiment to the process input of a second closed-loop experiment, according to Figure 3-3.

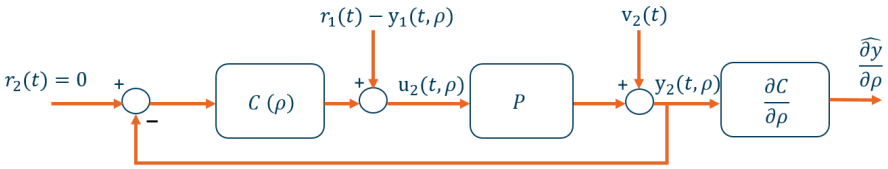

Figure 3-3: Schematic overview of the gradient experiment. An estimate of the required gradient $\widehat{\frac{\partial y}{\partial \rho}}$ is obtained by adding $r_1(t) - y_1(t,\rho)$ of the first experiment to the process input and multiplying the output $y_2(t,\rho)$ with the known gradient $\partial C/\partial\rho$.

The output $y_2(t,\rho)$ is multiplied with the known gradient $\partial C/\partial\rho$ to obtain the required gradient. However, the gradient retrieved with this second experiment is only an estimate, since it is contaminated with the noise $v_2(t)$. Hence,

$$\widehat{\frac{\partial y}{\partial \rho}}(t,\rho_i) = \frac{\partial C}{\partial \rho}(\rho_i)\left(S(\rho_i)P(r_1(t) - y_1(t,\rho_i) + S(\rho_i)v_2(t)\right), \tag{3-13}$$

where the subscript indicates the experiment number and $Sv_2(t)$ denotes the noise contamination. This noise contamination is removed by using data from a third experiment for $\tilde{y}(t,\rho_i)$ in the partial derivative described by Equation 3-8 . The motivation for the third experiment is to end up with an unbiased estimate of the cost function gradient, as its noise is uncorrelated with the noise present in both $y_1(t,\rho_i)$ and $S(\rho_i)v_2(t)$ in Equation 3-13. Summarizing, and defining $T(\rho_i)$ as the complementary sensitivity function, the following three experiments for data collection need to be performed

$$y_1(t,\rho_i) = T(\rho_i)r(t) + S(\rho_i)v_{i,1}(t), \tag{3-14}$$
$$y_2(t,\rho_i) = T(\rho_i)\left(r(t) - y_1(\rho_i)\right) + S(\rho_i)v_{i,2}(t), \tag{3-15}$$
$$y_3(t,\rho_i) = T(\rho_i)r(t) + S(\rho_i)v_{i,3}(t). \tag{3-16}$$

Convergence by iteration

Now all the required information of the gradient in Equation 3-8 is derived, a new set of control parameters can be obtained that is one step closer to the local minimum with the use of Equation 3-6. This minimum is found by iteration of the 3 described experiments, provided that the successive controllers in each iteration all stabilize the system. Unfortunately, guaranteeing stability is not straightforward and it is in general not known whether this condition is satisfied. A possible solution to this problem is adjusting the step size γ of the gradient search algorithm, to control how much a controller changes from one iteration to the next one, based e.g. on Bode plot comparison of each new derived controller with the previous one [36]. This solution, however, makes the iteration procedure more time-consuming which is a crucial problem with respect to practical points of view.

Extensions

The method was initially only intended for Single-Input Single-Output (SISO) linear time-invariant (LTI) systems under the assumption of closed-loop stability throughout the iterations. It has later been shown that IFT is capable of optimizing control parameters for disturbance rejection [38], non-linear systems [39, 40, 41], multivariable LTI systems [42] and periodic time-varying systems [43]. Extensions to non-linear controllers have been developed in [44, 45].

A number of articles have appeared on the subject of including stability constraints for the optimization procedure. In [46] both an H_∞ cost function and a robust H_2 criterion were proposed to ensure robust stability. Both approaches strive to achieve a compromise between

robustness and performance in iterative tuning steps. The H_2 optimization is simpler which typically means fewer iterations, i.e. faster convergence whereas the H_∞ design offers better control over the frequency behaviour. In [47] the robust stability is treated by a sensitivity shaping approach, and using a new criterion reflecting both performance and robustness specifications. In [48] a constrained IFT problem is formulated that is solved by introducing a frequency-domain penalty function, obtained through a non-parametric model of the controlled system, in order to penalize violations of the frequency-domain specifications imposed on the closed-loop sensitivity function.

Applications

Performance of the method has been shown in several application examples, together with an overview of the framework, in [37]. This reference mentions e.g. successful implementation for temperature regulation in a distillation column, and more recently, IFT was used to tune the control parameters of a robotic rehabilitation device for ankle injuries. It was concluded that the IFT scheme provided robustness to the control system by adapting to different situations, which in turn improved the effectiveness of robotic rehabilitation [49].

The main requirement that the initial closed-loop system is stable, implies that it can be directly used for optimization of wind turbine controllers [33]. The method is only recently applied to simulated wind turbines in [50] and in [33], both showing large potential in the wind industry. However, a warning for potential robustness issues and the explicit advise to be careful when implementing such algorithm on an actual turbine due to possible instability is also given in [33].

3-2-2 Virtual Reference Feedback Tuning (VRFT)

Another data-driven controller tuning approach is Virtual Reference Feedback Tuning (VRFT), which was originally introduced by Guardabassi and Savarasi in [51] and developed as a ready-to-use technique for controller design by Campi et al. in [52]. VRFT uses only a single record of input/output measurement data during normal closed-loop operation of the system.

The basic idea is that of interpreting the derived data as closed-loop data, produced by a virtual reference signal. This reference signal is computed by backpropagating the measured output of the system through a reference model, which describes the desired closed-loop of the system. In this way the fixed-structured controller can be optimized as a standard open-loop identification problem. A global optimum is found offline, without the need for any iterations.

Implementation

This implementation of the VRFT, applied in a Single-Input Single-Ouput (SISO) and Linear Time-Invariant (LTI) setting, is adopted from [51]. A schematic overview of the implementation is given in Figure 3-4. The process input $u(t)$ and corresponding output $y(t)$ are obtained through a single record on the actual unknown system. The reference model $M(z)$ describes the desired closed-loop of the system.

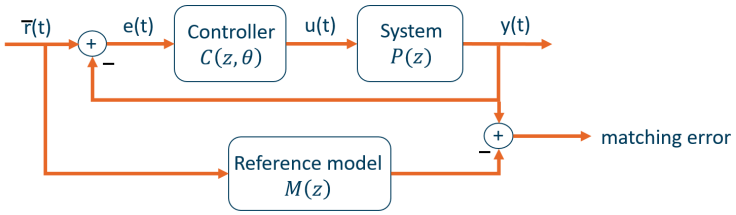

Figure 3-4: VFRT feedback control scheme, adapted from [51]. The reference signal $\bar{r}(t)$ is computed by backpropagating the measured system output $y(t)$ through the reference model $M(z)$. Next the tracking error signal $e(t)$ is computed. What is left is a standard open-loop identification problem between the computed $e(t)$ and the measured signal $u(t)$.

A virtual reference signal $\bar{r}(t)$ is calculated in such a way that it reproduces the system output $y(t)$ by filtering it through the reference model $M(z)$

$$y(t) = M(z)\bar{r}(t), \tag{3-17}$$

and the tracking error signal $e(t)$ is defined as the difference between virtual reference signal $\bar{r}(t)$ and the system output $y(t)$

$$e(t) = \bar{r}(t) - y(t). \tag{3-18}$$

Estimation of the control parameters θ is then reduced to an open-loop estimation problem, using filtered versions of both the tracking error $e(t)$ as input and the actual system input data $u(t)$ as output (for suitable selection of the pre-filter $L(z)$ the reader is referred to [52]),

$$e_L(t) = L(z)e(t), \tag{3-19}$$
$$u_L(t) = L(z)u(t), \tag{3-20}$$

such that the optimal control parameter vector $\hat{\theta}_N$ minimizes the following criterion

$$J_{VR}^N(\theta) = \frac{1}{N}\sum_{t=1}^{N}\left(u_L(t) - C(z,\theta)e_L(t)\right)^2. \tag{3-21}$$

This criterion is an explicit function of the data, computable without any knowledge of the system other than the single set of input/output measurement data under normal operation. The solution $C(z,\hat{\theta}_N)$ then results in a (nearly) optimal solution to the actual control objective

$$J_{MR}(\theta) = \left\| \left(\frac{P(z)C(z,\theta)}{1 + P(z)C(z,\theta)} - M(z) \right) W(z) \right\|_2^2, \tag{3-22}$$

that minimizes the difference between the system $P(z)$ response in closed-loop with the controller and the desired reference model. $W(z)$ represents an appropriate frequency domain

weighting function, as was introduced in [52] and is similar to the one used in [37] for IFT. If the controller is parametrized linearly, the optimization problem becomes convex and, in contrast to IFT, convergence to the global optimum can be shown [35].

The controller complexity is fixed in the beginning when the controller structure is selected and does not require a parameter initialization. Provided that the controller structure $C(z, \theta)$ is only slightly under-parameterized, the resulting $C(z, \hat{\theta}_N)$ is nearly optimal, and represents a good approximation of the optimal controller. If the optimized controller gives perfect matching between the closed-loop and the reference model, the obtained $C(z, \hat{\theta}_N)$ is the optimal one.

Extensions

The VRFT method has been extended to two-degree-of-freedom problems in [53] and non-linear systems in [54]. Improvements to the earlier implementation are made in [38], where a set of constraints is included for ensuring closed-loop stability and the correlation approach is used to deal with the influence of measurement noise. The latter approach to deal with noise is an alternative to the one in [52], which introduces instrumental variables consisting of either an additional experiment or identification of the plant (hence, in the latter case, making it model-based again). In [55] it is proposed to use VRFT in an iterative manner, gradually tightening the performance specifications, to fine-tune the controller closer to the optimal solution.

VRFT typically outperforms IFT in convergence rate [56] and only requires a single experiment, but often results in a *nearly* optimal solution. Therefore, in e.g. [52] and [57], it is suggested to use VRFT as an effective initialization tool and to use gradient-based iterative algorithms (like IFT) for the fine-tuning of controllers. Recently in [58], VRFT is used in combination with a reinforcement Q-learning algorithm for position control of a simulated multi-variable aerodynamic system.

Applications

In [59] an application of the VRFT method to an active suspension has been presented. The corresponding results show that the method has been able to provide satisfactory controllers in this context. In [60] VRFT was used to design feedback controllers for knee joint movement of paraplegics. Traditionally, this is done by model identification tests, requiring an iterative method of system excitations. The use of the VRFT strategy significantly reduces the time required for controller design and considerably simplifies the patient rehabilitation protocols. More recently, in [61], a multi-variable VRFT simulation study is performed for waste-water treatment plant control. The possible interactions amongst different control loops are handled using a decoupling approach where each control signal is computed depending on the error signal of all the loops at the same time. The results show substantial improvements in the plant performance after the controllers are implemented.

3-2-3 Extremum Seeking Control (ESC)

Extremum Seeking Control (ESC) is an online data-driven algorithm, built upon the gradient search scheme. The theory behind ESC was introduced by Leblanc and dates back to 1922 [62]. The algorithm estimates the online gradient by using a pair of dither and demodulation signals in combination with proper filtering, and optimality is achieved by closing the control loop via integral action. By locking the gradient extraction process to the dither frequencies, the search process is decoupled from changes due to exogenous disturbance and/or process variation provided that appropriate signal-to-noise ratio (SNR) is present in the dithered output [63].

Implementation

This implementation of the ESC control algorithm, applied in a Single-Input Single-Output (SISO) setting, is adopted from [63]. A schematic overview of the implementation is given in Figure 3-5. The objective is to maximize the function f by proper selection of the control parameter $\hat{u}$ in real time. ESC accomplishes this goal by finding the input that leads to a vanishing gradient of $\partial f/\partial u = 0$. The gradient is estimated from measurements of the objective function f using an additive perturbation $S(t)$ on the control parameter.

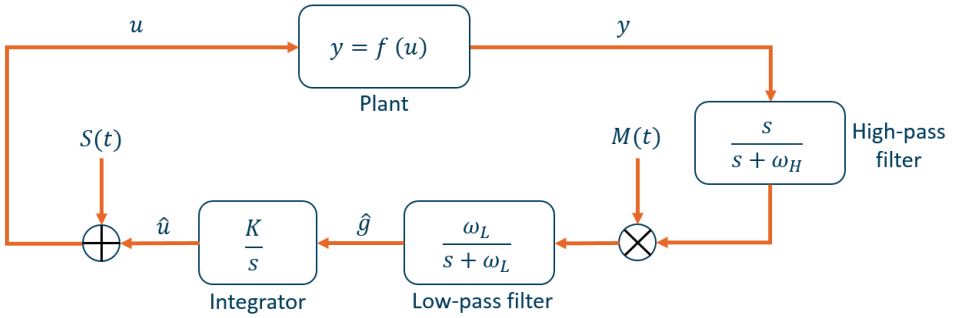

Figure 3-5: Schematic overview of the ESC control loop, adapted from [63]. The algorithm estimates the gradient $\hat{g}$ online, by using the sinusoidal dither $S(t)$ and demodulation $M(t)$ signal in combination with proper filtering. Optimality is achieved by closing the control loop via integral action.

The dither signal $S(t) = asin(\omega t)$, where ω defined as the dither frequency, is added to the control parameter $\hat{u}$ in real time (see lower left of Figure 3-5). The plant input u becomes

$$u = \hat{u} + asin(\omega t). \tag{3-23}$$

The corresponding plant output y is then

$$y = f(\hat{u} + asin(\omega t)). \tag{3-24}$$

The Taylor series expansion of the plant output is

$$y = f(\hat{u}) + asin(\omega t)\frac{\partial f}{\partial u} + h.o.t. \tag{3-25}$$

where "*h.o.t.*" stands for higher order terms. The high-pass filter is designed to filter out the DC term of Equation 3-25, while passing the AC terms, i.e.

$$asin(\omega t)\frac{\partial f}{\partial u} + h.o.t. \tag{3-26}$$

This high-pass filtered signal is then multiplied by the demodulation signal $M(t) = \frac{1}{a}sin(\omega t)$,

$$\frac{1}{a}sin(\omega t) \cdot \left(asin(\omega t)\frac{\partial f}{\partial u} + h.o.t.\right) = (1 - cos(2\omega t))\,\frac{\partial f}{\partial u} + h.o.t. \tag{3-27}$$

The low-pass filter is designed to retain the DC term $\partial f/\partial u$, which is the estimated gradient $\hat{g}$, and meanwhile filtering out the AC terms. Closing the loop with an integrator drives the gradient to zero in steady-state provided that the closed-loop is asymptotically stable, hence resulting in a local optimum.

Finally, the integrator gain K is a major parameter effecting the convergence speed, i.e. the larger the gain, the faster the convergence speed. However, too large gain leads to overshoot in the searching process, or even instability. A small integrator gain increases the degree of relative stability, however, results in slower convergence [63].

Extensions

Leblanc's work [62] and its application to electric railways in 1922 is often cited as the earliest work on ESC and is even quoted as the very first "adaptive" controller reported in literature [64]. He desribed an extremum seeking mechanism to maintain the desirable maximum power transfer from an overhead electrical transmission line to a tram car. There was also great interest in the field of ESC in 1950s and 1960s along with optimization theory, adaptive control and nonlinear control theory. However, it lost attention in the theoretical control literature because of the difficulties that arose in a rigorous analytical treatment. Still Åström and Wittenmark [65] put, in 1995, extremum control among the most promising future areas for adaptive control and mention applications in chemical reactors, combustion engines, and gas furnitures.

A major breaktrough came in 2000, when Krstić and Wang first proved stability of an extremum seeking feedback scheme [64]. They did this by employing the tools of averaging and singular perturbation analysis, and their research allowed for general SISO nonlinear dynamic systems. Some performance improvements were made by Krstić in [66], in particular the use of dynamic compensation to improve the rate of convergence. This reignited a renewed interest in ESC and many applications followed, of which multiple are listed in the overview of [67].

Rotea in [68] derived a model for the general case of multivariable optimization with constant parameters, which was used for stability and performance calculations in the presence of noise. Time-varying dynamics were transformed into a linear time-invariant (LTI) system with the use of averaging. The model was also used to derive a set of multivariable extremum seeking guidelines, which are often cited in literature. Ariyur and Krstić provided the multivariable ESC scheme for general time-varying parameters [69]. For a comprehensive overview of the method the reader is referred to the book of Ariyur and Krstić [70] on real-time optimization by ESC.

Applications

Unlike the previous two discussed methods in this chapter, ESC has been applied to several wind turbine related problems for more than a decade. A first attempt to control the pitch angle of a fixed-speed wind turbine was made by Komatsu et al. in 2001 [71]. The simulated turbine operated at a constant speed with pitch control only, but it appeared that the optimal pitch angle under different wind speeds remained the same, which did not reflect the fact that the optimal pitch varies with wind speed [67]. Ishii et al. [72] applied in 2003 a adaptive extremum control scheme to a two-bladed micro wind turbine with variable pitch structure and modelling was performed through a wind tunnel experiment.

Creaby et al. [67] proposed in 2009 a multi-input ESC algorithm for maximizing the wind power output using the generator torque gain and blade pitch, and simulation was performed for both fictitious and field recorded wind profiles. Significant improvement in power capture was was demonstrated, but no experimental field data was given. Another simulation based research was presented in 2014 by Ghaffari and Krstić, they applied a Newton-based multivariable ESC scheme to a two-layer control scenario, with the ESC torque control as the outer loop and a nonlinear power conversion controller for the squirrel-cage induction generator as the inner loop [73].

Finally, in 2016, Xiao et al. [63] presented both experimental and simulation based results on the CART3 facility at the National Renewable Energy Laboratory (NREL). Two individual single-input ESC schemes were used, i.e. collective blade pitch and torque gain ESC respectively. Double-digit percentage increases in energy capture with respect the NREL baseline controller were shown. Xiao et al. also proposed in [74], unfortunately only simulation based, a novel region 2 control scheme with a multi-objective ESC so that nearly optimum power capture is achieved while reducing structural loads. Hence, despite the ongoing research, field recorded results with respect to wind turbines remain scarce.

3-3 ESC as direct data-driven solution for DOT500

This section discusses the selection of a suitable data-driven controller tuning method for the DOT500 turbine. This method is later used in Chapter 7 to update actual control parameters of the DOT500, with the use of operational field data.

The underlying control design of both the Iterative Feedback Tuning (IFT) and Virtual Reference Feedback Tuning (VRFT) were set as a reference tracking problem, e.g. for the rotor speed regulation problem in region 3. In this region the suitable reference is known and the

tuning methods could be applied to update the blade pitch controller, which is used to regulate the rotor speed and to reject disturbances from wind fluctuations. In [33], collective pitch control was tuned with the IFT framework in simulation. As was discussed in Section 3-2-2, it could be interesting to combine this study with a VRFT approach as an initialization tool. The initialization then localizes the global optimum offline, reducing instability risks and turbine excitations, followed by local optimization through IFT. From a more practical point of view this would also reduce the amount of required iterations and time spent at the turbine.

Notice however that the key control novelty of the DOT500 turbine lays in the spear valve controller action, which is mainly active in below-rated wind regions. This region in particular is also very interesting for data-driven controller tuning, since modelling of this region is a cumbersome task. This region is less suited for reference tracking, since this would require the reference to be obtained from the (modelled) power map. Instead, Extremum Seeking Control (ESC) could be used for optimization of a certain performance index. Using this method to directly optimize the DOT500 power output would eliminate the reference requirement.

In addition, there are a number of other benefits to use ESC. First, the framework has been proven to work well in the presence of a wind disturbance [63]. Second, ESC requires a single experiment with only slowly varying excitation of the input signal. The framework does not require any iterations with newly derived controllers, hence reducing the risk of implementing an unstable controller. Third, stability issues could be further reduced by gradually increasing a conservatively chosen integrator gain. Finally, the ESC framework is fairly easy to obtain, implement and understand. This implies that the method could be easily reproduced, without the need of expert knowledge. In contrast, the main disadvantage is that ESC leads to a local optimum only. This could require multiple experiments from different starting points to check for the presence of additional minima in order to find the global minimum.

Tuning of the DOT500 with ESC not only improves turbine performance, but field recorded data also delivers an important contribution to the ongoing feasibility study concerning the applicability of the algorithm to wind turbines.

Chapter 4

DOT500 control design

This chapter outlines the development of the DOT500 control design. It first states the control objectives for the DOT500 turbine in Section 4-1. This is followed by the selection of a suitable control strategy in Section 4-2. Next the individual controller designs are introduced: spear valve control is explained in Section 4-3, the derivation of blade pitch and yaw control are given in Section 4-4 and 4-5 respectively. Finally, in Section 4-6, the control interaction and software implementation are given.

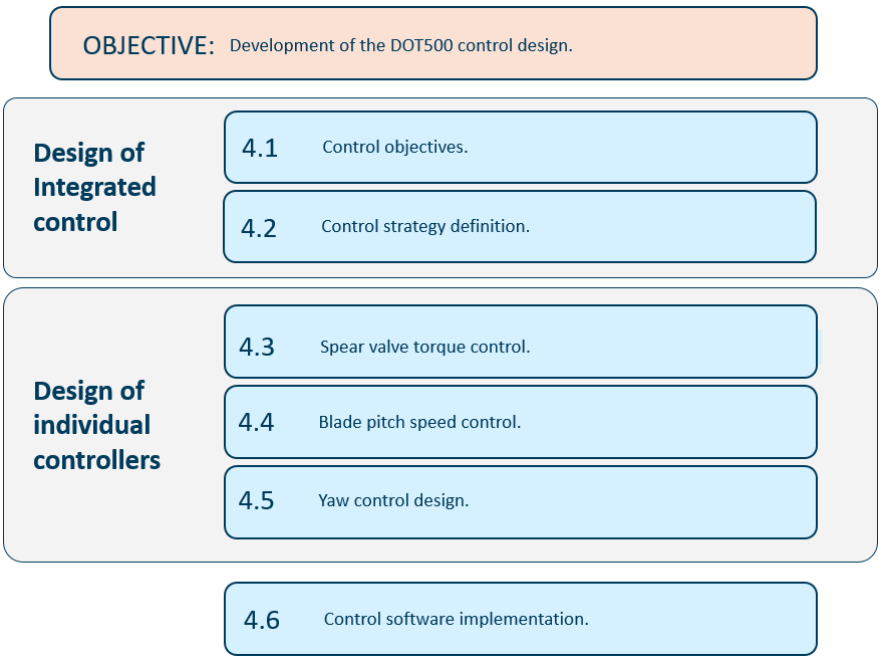

Figure 4-1: Chapter outline

.

4-1 Control objective: maximum energy capture

As in conventional turbine control, the primary control objective is to design a safe, functional controller for the DOT500. Once a functional control system is developed, maximum energy capture will be taken into account. Hence, the overall control objective is formulated as:

Maximisation of energy capture, while taking account of safe operation restrictions such as rated power, rated speed and cut-out wind speed.

The turbine is prevented from excessive dynamic mechanic loads by keeping the system within the regions of operation of the original Vestas V44. Load mitigation is not explicitly stated in the control objective, since both load design limitations and accurate load measurements are unavailable. In contrast to common practise, conditioning the generated power to comply with interconnection standards is also not taken into account, since the DOT500 is not yet connected to the grid.

Finally, due to inclusion of the oil loop, reduced partial load efficiency of the hydraulic drive train is expected from earlier performance tests. Therefore, a distinction in objective definition is made between below- and above-rated turbine operating conditions. In the below-rated region, the objective is to maximise rotor power, whereas generator power is maximised at rated operation.

The latter distinction is justified by the assumption that partial load efficiency will be improved in later design stages. For now, technical feasibility analysis of hydraulic transmissions over the turbine full operating range is the company's target. In this stage it is not yet expected to operate cost-effective in the below-rated wind speed region.

4-2 Control strategy definition

The control strategy describes the approach for the DOT500 turbine to attain the desired power curve in steady state. First the regions of operations are given in Section 4-2-1, followed by the main control loop strategy in Section 4-2-2. In conclusion, in Section 4-2-3, the control strategy is defined on the torque-rotational speed plane.

4-2-1 Regions of operation

The DOT500 has three main regions of operation, as depicted in Figure 4-2. In region 1, the power available in the wind is too low to start-up the rotor; hence, the turbine does not run. The cut-in wind speed ($V_{\text{cut-in}}$) is therefore defined as the minimum required start-up wind speed. Note that this approach deviates from industry standard, where often operation cost and losses are taken into account.

As mentioned in the previous section, the region 2 objective is to capture as much rotor power from the wind as possible. Region 3 is entered when the wind speeds are high enough (V_{rated}) that the turbine must limit the fraction of the wind power captured so that electrical and mechanical loads restrictions are not exceeded. Pitching the blades or yawing the turbine out of the wind are methods to actively limit the available aerodynamic torque.

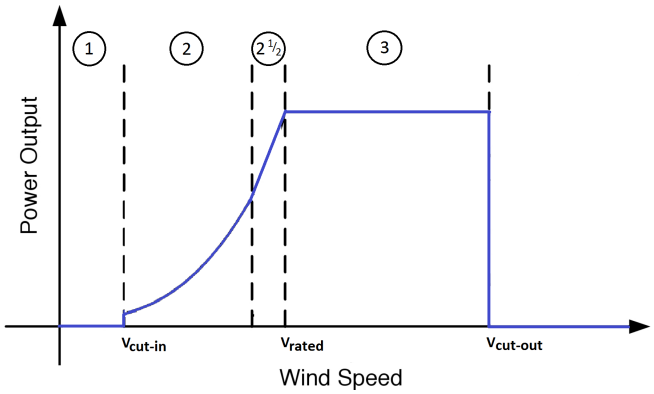

Figure 4-2: DOT500 turbine regions of operation

Above cut-out wind speed ($V_{\text{cut-out}}$), the turbine is shut down to prevent it from structural overload. The turbine rated power output normally arises from a compromise between available energy and manufacturing costs. For instance, designing the turbine to extract all the available energy up to cut-out wind speed would lead to an increment in the cost per kW, while wind speeds above rated are not frequent enough to justify the extra sizing of the turbine required to capture power above rated [75]. Rated power, rated speed and cut-out wind speed are taken from Vestas V44 turbine data sheets (see Table 4-1).

Parameter	Value
Cut-in wind speed	5 m/s
Cut-out wind speed	20 m/s
Rated rotor speed	28 RPM
Rated rotor power	600 kW

Table 4-1: Key operational parameters of the original Vestas V44 turbine [29]

Finally, an intermediate operation state is introduced: region $2\frac{1}{2}$. This region is used for the transition between control objectives around rated speed. Using a transition region smoother than the ideal one alleviates transient loads significantly at the cost of some loss in energy capture [75].

The remainder of this chapter will describe how the turbine control system is designed to approach the ideal power-versus-wind-speed curve in steady-state. The control strategy will settle steady-state values of rotor speed and torque within the range of turbine operation.

4-2-2 Main rotor speed control feedback loops

In accordance with widespread current practice and the original Vestas V44 design, the DOT500 turbine control design is based on the principle of Variable-Speed, Variable-Pitch (VSVP) control. Variable-speed operation increases the energy capture at low wind speeds whereas variable-pitch operation enables an efficient power regulation at higher than rated wind speeds [75].

However, as mentioned in Chapter 1, the novelty in the DOT500 control design is the use of hydraulic pressure regulation instead of generator torque to influence rotor speed in the below-rated region. Both spear valve and pitch control use the rotor speed as the sole feedback input, as shown in Figure 4-3.

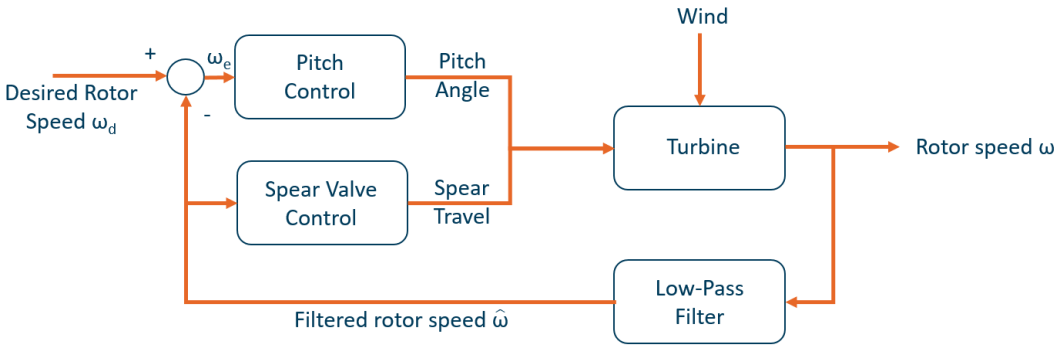

Figure 4-3: DOT500 control feedback loops

In below-rated wind speed conditions, the turbine operates at variable speed and a fixed fine-pitch angle in order to maintain operation at the maximum rotor power coefficient. In high wind speeds, the pitch angle is adjusted to limit the captured power at its rated value. Both control loops are Single-Input Single-Output (SISO) and are decoupled from each other.

Low-pass filter

The filter in Figure 4-3 is a first order low-pass filter on the rotor speed, discretized using Tustin's method [76] and the discrete time step T_s. This output of the filter is then given by

$$y(k) = \frac{2 - T_s\omega_b}{2 + T_s\omega_b} y(k-1) + \frac{T_s\omega_b}{2 + T_s\omega_b} u(k) + \frac{T_s\omega_b}{2 + T_s\omega_b} u(k-1), \tag{4-1}$$

where in this case $y(k)$ is the filtered rotor speed, $u(k)$ is the unfiltered rotor speed and ω_b the filter cut-off frequency. The drawback of this simple filter is its gentle roll-off in the stop band. Jonkman et al. in [77] considered other linear low-pass filters, such as Butterworth, Chebyshev, Elliptic, and Bessel filters. However, none were found to give superior performance in the overall system response, so they did not warrant the added complexity of implementation.

4-2-3 Control strategy defined on the torque-rotational speed plane

The DOT500 control strategy is depicted on the torque-rotational speed plane in Figure 4-4. Once the wind is above $V_{\text{cut-in}}$, a start-up sequence will be performed between the points O and B. In region 2 the turbine is operated along the $C_{p,\max}$ locus between the points B and C, as will be discussed in Section 4-3.

As proposed by Bossanyi in [30], a torque-speed ramp strategy is implemented in the transition region $2\frac{1}{2}$ between the points C and D. In above-rated wind speeds, the pitch angle is controlled in order to keep the turbine operating at point D.

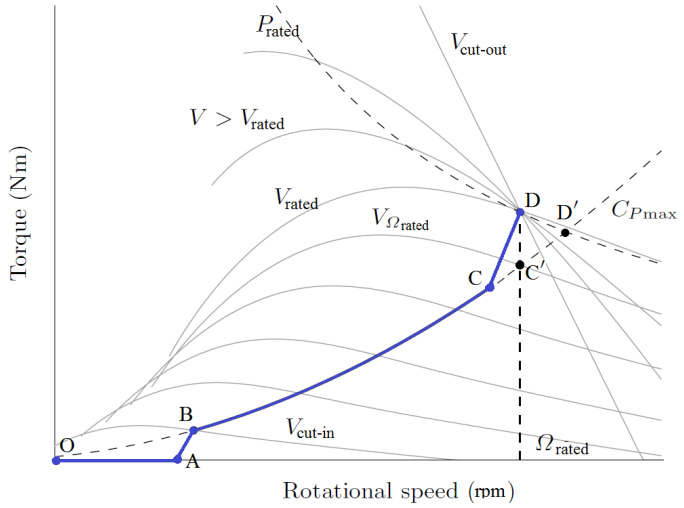

Figure 4-4: DOT500 turbine control strategy, adopted from Bianchi [75]

Due to the rated rotor speed restriction, the point D is used instead of the ideal point D'. Furthermore, a slightly higher energy capture could have been obtained by following the $C_{\text{p,max}}$ locus up to the point C', but this would require a PI-control strategy between C'-D. The latter is however infeasible with the current spear valves, due to insufficient bandwidth in the spear valve position to rotor speed system in this operating region.

4-3 Spear valve torque control

The DOT system torque is based on fluid pressure regulation and is controlled by adjusting the spear valve positions, which are located at the end of the high-pressure water line. Where in conventional turbines the required system torque is directly regulated by the generator torque demand, the relation between spear valve travel position (effective water flow area) and system torque of the DOT500 turbine is still unknown.

In region 1, during start-up, the spear valves are opened as wide as possible. In this configuration the system torque is minimised to allow for rotor spin-up. On the other hand, in region 3, the spear valves are nearly closed in order to maximize energy capture.

The real difficulty arises in region 2, where the system torque should match the aerodynamic rotor torque at varying rotor speed, while maintaining the optimal tip-speed ratio. This relation will be discussed first in Section 4-3-1, followed by the relation between spear valve position and system torque in Section 4-3-2.

4-3-1 Standard torque control

The region 2 objective is to maximize energy capture from the available wind. Energy capture efficiency can be expressed by the power coefficient C_{p}, which is defined as the ratio of the

aerodynamic rotor power P to the power P_{wind} available from the wind, that is,

$$C_{\text{p}} = \frac{P}{P_{\text{wind}}}, \tag{4-2}$$

where the available power from the wind is given by

$$P_{\text{wind}} = \frac{1}{2}\rho A V^3, \tag{4-3}$$

where ρ is the air density, A is the rotor swept area and V is the rotor effective wind speed, which is assumed to be uniform across the rotor swept area. The aerodynamic rotor power P in Equation 4-2 is given by

$$P = \tau_{\text{aero}}\omega, \tag{4-4}$$

where τ_{aero} is the aerodynamic rotor torque and ω is the rotor speed. The aerodynamic torque of a rotor with radius R is given by

$$\tau_{\text{aero}} = \frac{1}{2}\rho A R^3 \omega^2 \frac{C_p(\lambda, \beta)}{\lambda^3}. \tag{4-5}$$

The C_{p} in Equation 4-5 is a nonlinear function of Tip-Speed Ratio (TSR) λ and pitch angle β, that can be altered via torque and/or blade pitch control. Figure 4-5 shows a typical turbine C_{p} surface. Since turbine power is proportional to the power coefficient, the turbine is ideally operated at the peak of the surface, which is often denoted by $C_{\text{p,max}}$.

As the tip-speed ratio continuously changes, and because the wind changes speed more quickly than the turbine rotor speed, there does not exist a static relationship between wind speed and turbine power in dynamic conditions. However, under steady-state conditions, a static relationship exists [78]. Thus, region 2 control is primarily concerned with varying the rotor speed to maintain the optimal TSR, resulting in $C_{\text{p,max}}$.

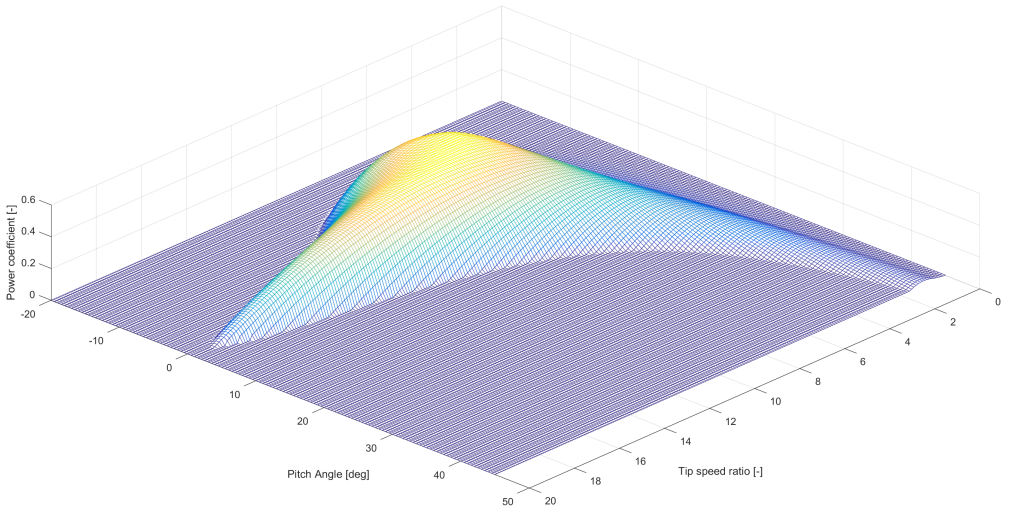

Figure 4-5: Typical wind turbine C_p-λ-β curve

Since maximum C_p is achieved at the turbine's fine-pitch angle, the region 2 objective should be solely met by system torque control. The region 2 control law is is given by

$$\tau_\mathrm{sys} = K\omega^2, \tag{4-6}$$

where the optimal torque mode gain K is given by

$$K = \frac{1}{2}\rho A R^3 \frac{C_\mathrm{p,max}}{\lambda_*^3}, \tag{4-7}$$

where R is the rotor radius, and λ_* is the tip-speed ratio at which the maximum power coefficient $C_\mathrm{p,max}$ is located. From Newton's second law of motion, a first-order model of the turbine is given by

$$\dot{\omega} = \frac{1}{J}\left(\tau_\mathrm{aero} - \tau_\mathrm{sys}\right), \tag{4-8}$$

hence, by substituting Equation 4-5 through 4-7 into 4-8, the following relation is obtained

$$\dot{\omega} = \frac{1}{2J}\rho A R^3 \omega^2 \left(\frac{C_\mathrm{p}(\lambda,\beta)}{\lambda^3} - \frac{C_\mathrm{p,max}}{\lambda_*^3}\right). \tag{4-9}$$

Since the rotor inertia J, the air density ρ, the rotor swept area A, the rotor radius R, and the squared rotor speed ω^2 are all non-negative, the sign of the angular acceleration $\dot{\omega}$ depends on the sign of the subtraction in Equation 4-9. When the tip-speed ratio $\lambda > \lambda_*$ and the fact that $C_\mathrm{p} \leq C_\mathrm{p,max}$, it follows from Equation 4-9 that $\dot{\omega}$ is negative and the rotor decelerates toward $\lambda = \lambda_*$. On the other hand, when $\lambda < \lambda_*$ and

$$C_\mathrm{p} > C_\mathrm{p,max}\frac{\lambda_*^3}{\lambda^3}, \tag{4-10}$$

it follows that $\dot{\omega}$ is positive. Above control strategy is often referred to as the *standard* torque control [78]. The torque control loop thus regulates the rotor speed ω towards the turbine's optimal $C_\mathrm{p,max}$ in region 2.

4-3-2 Relation between spear valve position and standard torque control

The required addition to the standard torque control strategy for hydraulic control of the DOT500 turbine is the translation between the required system torque (Equation 4-6) and the associated spear valve position. In order to find this mapping, steady-state tests on the hydraulic drive train system are performed in Section 5-1-2. The current section explains the theoretical control framework and its implementation.

According to the control law given in Equation 4-6, the optimal torque is a function of rotor speed in the below-rated region. Given a detailed mapping of the system torque over the rotor-speed-versus-spear valve-position plane, the identified system torque is matched to the optimal torque. This is depicted in Figure 4-6, where the system torque is given in *red* and the optimal below-rated rotor torque in *blue*.

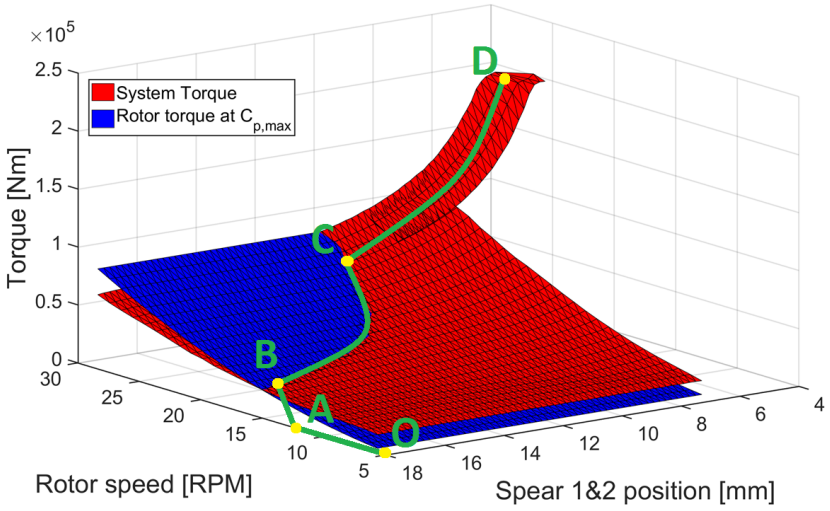

Figure 4-6: Optimal torque control path for DOT500. The intersection between the rotor torque at $C_{\mathrm{p,max}}$ (blue) and the system torque (red), denoted by B-C, results in optimal aerodynamic efficiency of the rotor. The region O-B describes a start-up procedure, while in C-D the turbine is ramped up to the rated operating point D.

Based on the experiments, the optimal control path for DOT500 is depicted in Figure 4-6. Between points O and A, the rotor is accelerated from standstill by pitching the blades to 45 deg. When sufficient rotor speed is measured, such that point A is passed, the system torque is linearly ramped up until point B is reached and the pitch angle is directed towards fine-pitch. From there on the rotor is in region 2, between points B and C, with maximum energy capture as the objective.

The turbine operates at its highest aerodynamic efficiency point $C_{\mathrm{p,max}}$ at a specific fine-pitch angle and tip-speed ratio. The pitch angle is easily maintained at the optimally efficient vine-pitch angle. However, tip-speed ratio depends on the incoming wind speed and is therefore continually changing. Hence, region 2 control is primarily concerned with varying the rotor speed to track a constant tip-speed ratio [79].

To find the relation between measured rotor speed and required spear valve setting, a parametrisation of the intersection between the rotor and system torque plane is identified (see Figure 4-7). For this purpose, a third order polynomial fit is applied to the intersection projected on the x-y plane, which now directly relates the rotor speed to the optimal spear valve settings (see Figure 4-8). The polynomial fit to the projected fit is calculated in the form

$$s(\omega) = a_3\omega^3 + a_2\omega^2 + a_1\omega + a_0, \tag{4-11}$$

where s is the desired spear valve position in [mm] at rotor speed ω, and a_{i} the polynomial coefficients. The polynomial fit function now provides a feedforward reference signal to the spear valves for optimal system torque at the operating rotor speed. When the rotor accelerates, the spear valves close and vice versa. This concept replaces the direct generator torque control normally used in standard wind turbines.

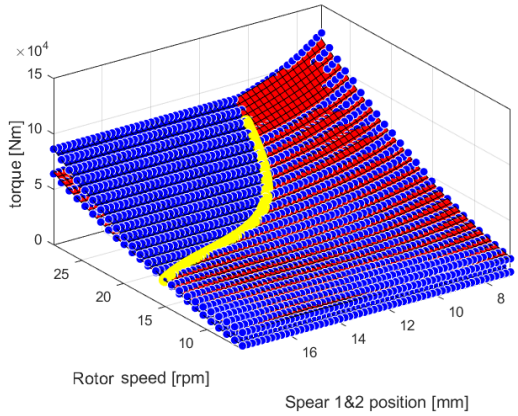

Figure 4-7: Intersection (yellow) between rotor (blue) and system torque (red) plane

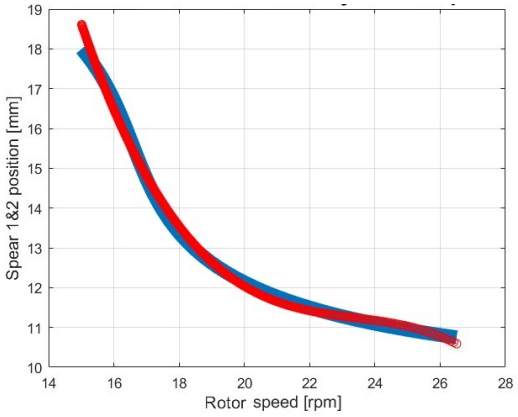

Figure 4-8: Polynomial fit (red) to parametrization of the intersection (blue)

When nearing rated rotor speed, from point C in Figure 4-6 onwards, the spear valve controller deviates from the optimal $C_{\mathrm{p,max}}$ plane and increases torque up to rated power. This transition corresponds to region $2^1/_2$ in Figure 4-2. By evaluation of spear valve actuation characteristics, with the bandwidth required for active tracking of the rotor speed in this region, it is concluded that the spear valve actuators are too slow for active speed guidance once the slope is further increased. More advanced techniques could be developed for this intermediate region, once the current controller stabilizes the turbine.

Finally, point D then corresponds to region 3, where rated rotor speed is reached and the system torque is held constant. From here on blade pitch control takes over the speed regulation and the objective to maintain rated turbine power, by continuous adjustment of the rotor aerodynamic characteristics.

4-3-3 Pelton turbine rotational speed regulation

The spear valves convert the high-pressure, low-speed flow into a low-pressure, high-speed water jet (V_{jet}), i.e. hydrostatic to hydrodynamic power. This hydrodynamic power is harvested by the Pelton turbine. The nominal pressure in the Pelton feed water pipeline determines the nominal speed of the water jet exiting the spear valves according to

$$V_{\mathrm{jet}} = \sqrt{\frac{2\Delta p_{\mathrm{feed}}}{\rho_{\mathrm{water}}}}, \tag{4-12}$$

where ρ_{water} is the water density and Δp_{feed} the pressure difference over the spear valve. The relation between the jet speed and the free run rotational speed V_{freerun} of the turbine is based on the Pitch Circle Diameter (PCD) of the Pelton turbine according to

$$V_{\mathrm{freerun}} = V_{\mathrm{jet}} \frac{30}{\pi} \frac{2}{\mathrm{PCD}}. \tag{4-13}$$

Based on Euler's turbo machinery equation [80], maximum power extraction is attained when the speed of the Pelton bucket (V_{b}) is half the jet velocity

$$V_{\mathrm{b}} = \frac{V_{\mathrm{freerun}}}{2}. \tag{4-14}$$

Note that the Pelton turbine wheel is mechanically coupled to the generator, whereas the hydrodynamic power transfer between spear valves and Pelton wheel is mechanically decoupled. Hence, by substituting Equation 4-12 through 4-14, the following relation between the generator rotational speed setpoint and the nominal water pressure in the Pelton feed is obtained

$$\omega_{\mathrm{gen}} = K\sqrt{\Delta p_{\mathrm{feed}}}, \tag{4-15}$$

where K is defined as the generator speed control gain and consists of

$$K = \sqrt{\frac{2}{\rho_{\mathrm{water}}}}\frac{30}{\pi}.\frac{1}{\mathrm{PCD}} \tag{4-16}$$

Based on the theoretical parameters required in Equation 4-12 through 4-14, this gain is found to be approximately 0.495. Later, in Chapter 7, this gain is experimentally tuned with Extremum Seeking Control.

4-4 Blade pitch speed control

Like in conventional wind turbines, the DOT500 uses pitch control to maintain a near constant rotor speed in above-rated wind conditions. This section starts with a general overview of the blade pitch control functionality in the different regions of operation. Then, in Section 4-4-2, the model derivation and gain scheduling will be explained.

4-4-1 Pitch control requirements

Rotor start-up

In the below-rated regions, blade pitch control is obtained by simple case logic. When the cut-in wind speed threshold is exceeded and the system is released from its idling state, the system moves into a start-up procedure, wherein the blade pitch angle is set to 45 deg. In Figure 4-9, the rotor torque is measured, keeping the rotor at standstill on parking brake, while a stair-case input signal is applied to the blade pitch angle. Around the 45 deg configuration the blades clearly obtain maximum torque, which is beneficial to accelerate the rotor.

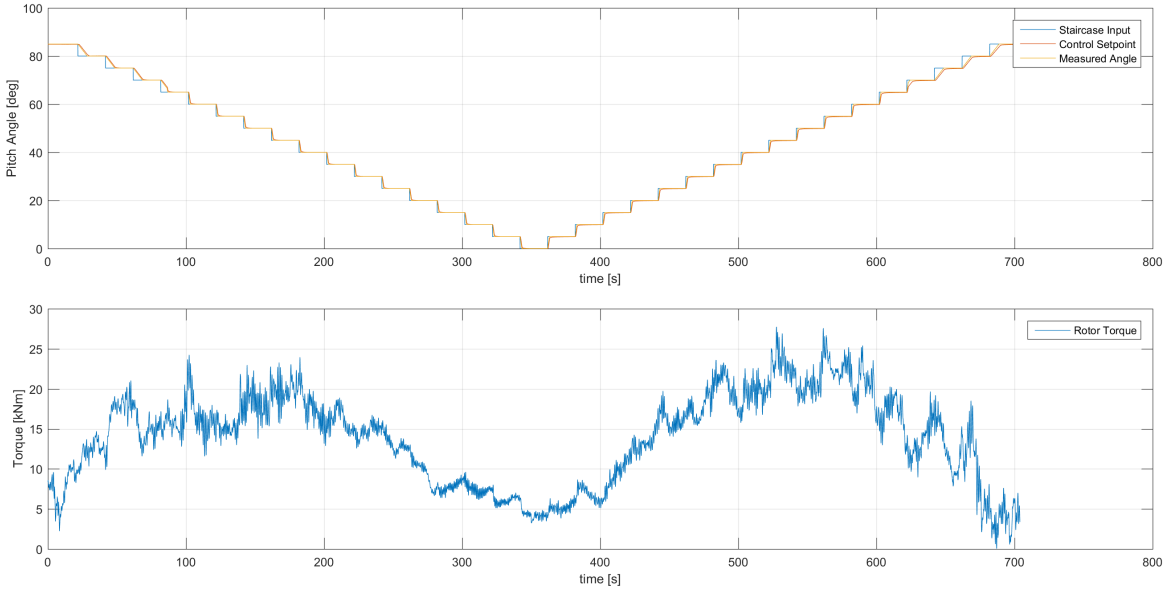

Figure 4-9: Rotor torque measurements at different pitch angles at standstill. Results indicate that maximum start-up torque is obtained around the 45 deg configuration.

Below-rated operation

When the rotor gained sufficient start-up speed, the blades are ramped with a constant rate to their fine-pitch angle. In the below rated regions, maximum power capture is obtained by keeping the rotor blades fixed at the fine-pitch angle. As stated earlier, little information on rotor performance characteristics are available for the acquired Vestas V44 turbine. Therefore, the DOT500 fine-pitch angle is assumed to be 0 deg, but will be further investigated by data-driven tuning in a later stage of this thesis.

Rated operation

Active blade pitch control is primarily used to limit the aerodynamic power in above-rated wind speeds, in order to keep the turbine within the design limits formulated in Section 4-2-1. In most commercial wind turbines, pitch control in region 3 is performed using the proportional-integral-derivative (PID) collective pitch control law

$$\beta_c(t) = K_{\mathrm{P}}\omega_{\mathrm{e}}(t) + K_{\mathrm{I}}\int_0^t \omega_{\mathrm{e}}(\tau)d\tau + K_{\mathrm{D}}\frac{d\omega_{\mathrm{e}}(t)}{dt}, \tag{4-17}$$

where $\omega_{\mathrm{e}} = \omega_{\mathrm{d}} - \omega$ is the rotor speed error and the desired rotor speed is ω_{d}. Because of its sensitivity to measurement noise, the derivative term is often combined with a low-pass filter or set to $K_D = 0$, leaving just a PI pitch controller. The latter method is applied to DOT, and a flowchart of its configuration is depicted in Figure 4-10.

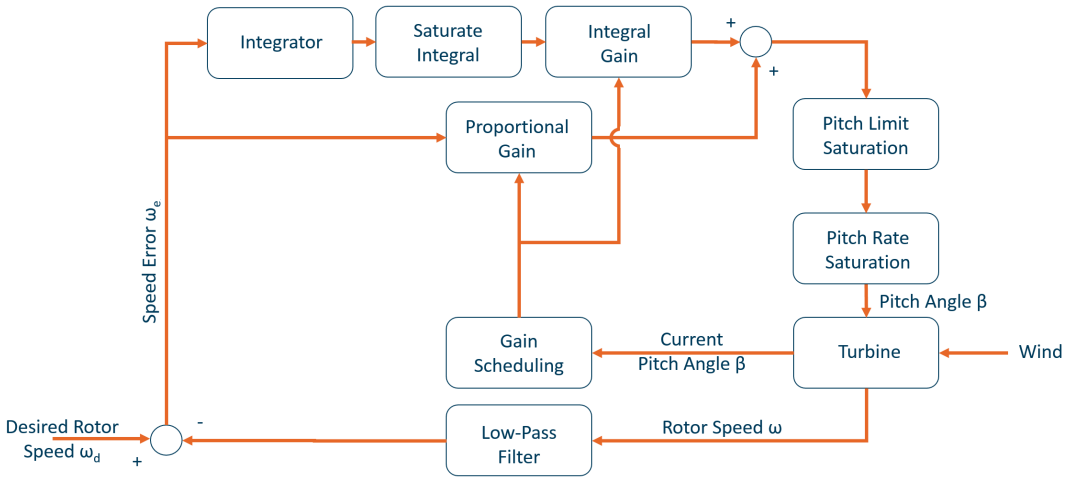

Figure 4-10: Flowchart of PI pitch control system for the DOT500

The pitch angle is limited by saturation between fine-pitch and feather position. At below-rated rotor speeds, the pitch angle is forced to the fine-pitch limit, as the rotor speed error becomes negative.

In addition, the pitch rate is saturated during start-up until either the fine-pitch angle or rated speed is obtained. This saturation allows for a smoother start-up procedure and reduces rotor speed overshoot during rotor start-up at rated wind speeds. After the start-up procedure, the maximum pitch rate of 8 deg/s is used, so the controller reacts adequate (near) rated speed.

Finally, the pitch rate saturation is lowered to 0.65 deg/s above 66 deg, since excessive loads were noticed when more aggressive rates were used around feather position. This rate limitation is also visible in the measured pitch angle line in Figure 4-9, at pitch angles between 66 and 88 deg.

4-4-2 Modelling of blade pitch control

Modelling of the blade pitch control system is done in three subsequent steps. First, an initial control design has been carried out using classical first-principles control design methods. Second, the derived initial design is applied to a high-fidelity model of the actual turbine at a number of operating points. This closed-loop data is used to obtain linear models of the turbine using subspace identification. In the third and final step, loop shaping techniques are applied to the obtained linear models.

Step 1: Initial controller design

Since accurate data of the Vestas V44 turbine was unavailable, a scaled version of a Vestas V66 turbine model is used in the high-fidelity wind turbine simulation software package `GH Bladed v4.5`. Both turbines originate from the same manufacturer and product series, and therefore are assumed to be similar in behaviour. However, in order to stabilise the wind turbine model at different operating points, an initial controller design is required.

The initial design of the required controller is based on the NREL baseline blade pitch controller described by Jonkman et al. in [77]. The derivation of this controller is based on a simple single-degree-of-freedom model and is given in Appendix B. Jonkman et al. use the following direct expressions for calculating the PI gains,

$$K_{\mathrm{P}}(\beta) = \frac{2J\Omega_0\zeta_\phi\omega_{\phi\mathrm{n}}}{N_{\mathrm{gear}}\left[-\frac{\partial P}{\partial \beta}(\lambda,\beta)\right]}, \tag{4-18}$$

and

$$K_{\mathrm{I}}(\beta) = \frac{J\Omega_0\omega_{\phi\mathrm{n}}^2}{N_{\mathrm{gear}}\left[-\frac{\partial P}{\partial \beta}(\lambda,\beta)\right]}, \tag{4-19}$$

where J is the rotor moment of inertia, Ω_0 the rated rotor speed, and N_{gear} the gearbox ratio. The desired natural frequency $\omega_{\phi\mathrm{n}}$ and damping ratio ζ_ϕ are taken as 0.6 rad/s and 0.65 respectively. Finally, the sensitivity of aerodynamic power to rotor-collective blade pitch $\delta P/\delta\beta$ is derived from the $C_{\mathrm{p}}\left(\lambda,\beta\right)$ relation of the Vestas V66 (see Figure 4-11). Both turbines are from the same manufacturer and product series, and therefore the power coefficient plane is assumed to be similar in shape.

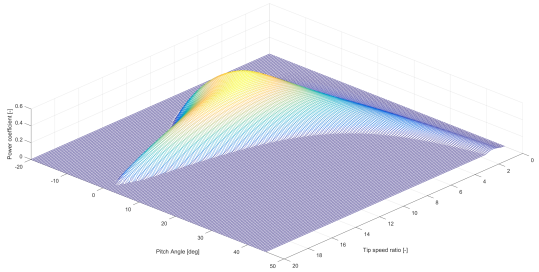

Figure 4-11: $C_p - \lambda - \beta$ relation for the Vestas V66 (see Figure 4-5 for enlarged version)

Above surface is related to the aerodynamic power P according to

$$P = \frac{1}{2}\rho A V^3 C_{\mathrm{p}}\left(\lambda, \beta\right), \tag{4-20}$$

where A is the rotor swept area of the Vestas V44 and the power coefficient $C_{\mathrm{p}}\left(\lambda, \beta\right)$ is a non-linear function depending on blade pitch angle β and tip-speed ratio λ. The blade pitch angle sensitivity $\delta P/\delta\beta$ is hence an aerodynamic property of the rotor that depends on the wind speed V, the blade pitch angle β and tip speed ratio λ according to

$$\frac{\partial P}{\partial \beta}\left(\lambda, \beta\right) = \frac{1}{2}\rho A V^3 \frac{\partial C_{\mathrm{p}}}{\partial \beta}\left(\lambda, \beta\right). \tag{4-21}$$

The change in power coefficient depends on the local gradient of the power coefficient surface and this gradient clearly varies with the operating point. This is shown in Figure 4-12.

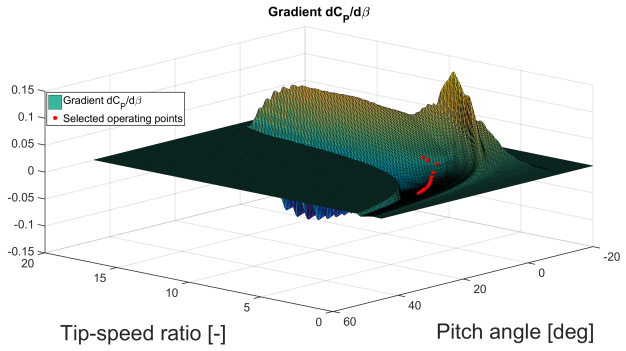

Figure 4-12: De graph of the $\partial C_p/\partial\beta$ relation for the Vestas V66. The *red* star markers indicate the selected operating points at wind speeds between 11 and 20 m/s.

Hence, the control authority of the pitch input varies with the current operating point. Taking the latter into account by a simple gain scheduling on the measured pitch angle, the initial K_{P} and K_{I} described by Equation 4-18 and 4-19 are now ready to use in the next design step.

Step 2: Derivation of linear input-output turbine models

The PI controller, with the derived initial K_{P} and K_{I} scheduled on the measured pitch angle β_{meas}, is implemented in `MATLAB/Simulink` and used as an external controller in the high-fidelity wind turbine simulation software tool `GH Bladed v4.5`. Bladed simulations are performed to obtain the pitch angle required to keep the rotor speed at rated speed Ω_0, for wind speeds between 11 m/s and 20 m/s, with intervals of 1 m/s.

This linearisation analysis involved perturbing the blade pitch angle at each wind speed and measuring the resulting variation in rotor speed. For persistent excitation, a Generalized Binary Noise (GBN) perturbation is applied on top of the controller blade pitch angle, with an amplitude of 1° and a bandwidth of 20 rad/s.

Then closed-loop LTI system identification using the Predictor-Based Subspace IDentification ($\mathrm{PBSID}_{\mathrm{opt}}$) [81] method is applied to the retrieved closed-loop input-output data from Bladed. The obtained linear models relate blade pitch angle to rotor speed around the specified operating points. The open-loop Bode diagrams of the models are given in Figure 4-13.

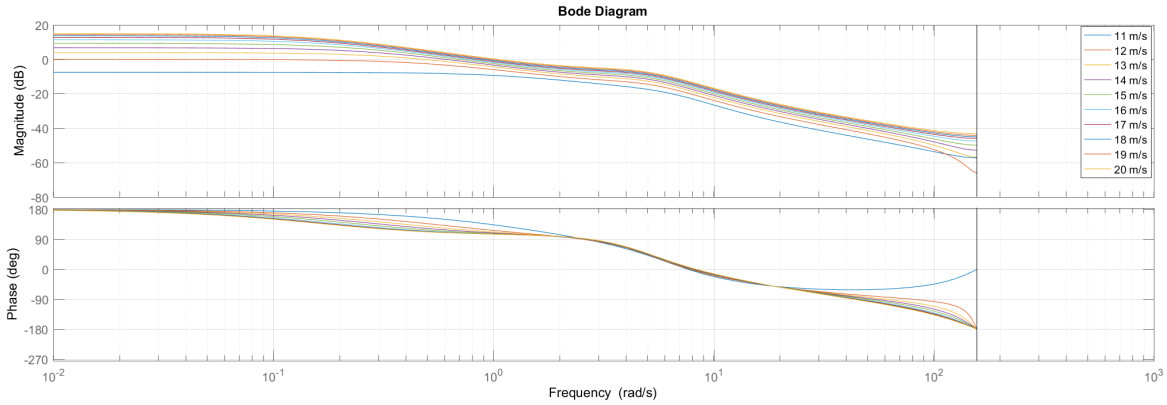

Figure 4-13: Bode and phase plots of the identified open-loop turbine models using the $\text{PBSID}_{\text{opt}}$ method. Plots are given for different wind speed operating points between 11 and 20 m/s.

Step 3: Control loop shaping

In this final step, loop-shaping techniques are applied to the derived linear models in order to construct a gain-scheduled PI pitch controller. The controller is designed for every model to attain a bandwidth of 0.5 rad/s and a phase margin of 75 deg in closed loop, to ensure that the controller is robust against uncertainties. Loop shaping is done with the `MATLAB pidtune` function, of which the results are shown in Figure 4-14. The corresponding closed-loop step responses are presented in Figure 4-15.

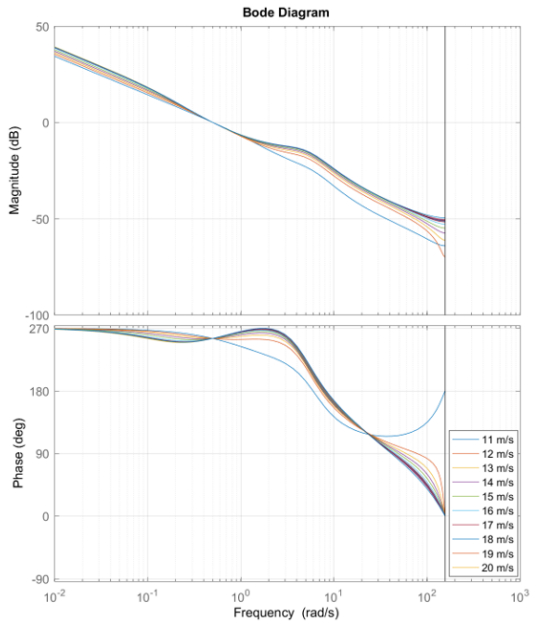

Figure 4-14: Bode and phase plot of the open-loop system times controller (CG), with a designed 0.5 rad/s bandwidth and 75 deg phase margin.

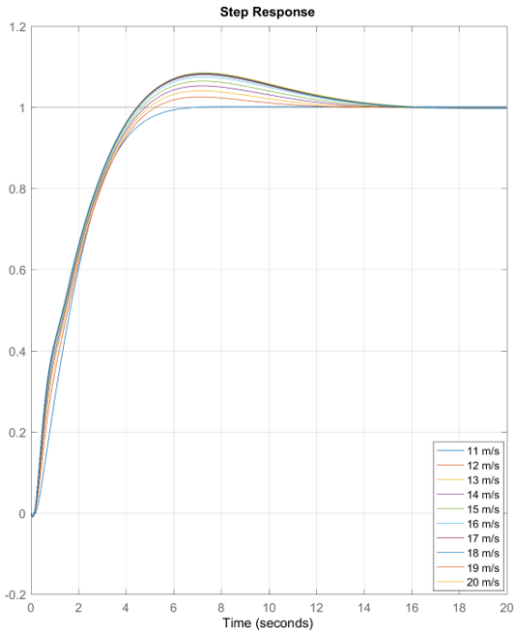

Figure 4-15: Closed-loop rotor speed step response at different wind speeds between 11 and 20 m/s.

The required PI gains K_P and K_I are summarized for every wind speed in Table 4-2.

Wind Speed [m/s]	**Pitch Angle [°]**	K_P	K_I
11.0	1.4046	0.4669	1.2464
12.0	5.4143	0.6401	0.5936
13.0	8.2134	0.6148	0.4114
14.0	10.5279	0.5903	0.3218
15.0	12.5707	0.5642	0.2626
16.0	14.4295	0.5420	0.2241
17.0	16.1599	0.5149	0.2007
18.0	17.7898	0.4854	0.1852
19.0	19.3353	0.4571	0.1733
20.0	20.8081	0.4321	0.1639

Table 4-2: Required controller gains at different wind speeds and corresponding pitch angles.

From Table 4-2 it is observed that constant PI gains are not adequate for effective speed control, since they vary considerably over region 3. Close to rated, since the fine-pitch angle is selected to maximize power, it follows that the blade pitch sensitivity is very small. Thus a much larger controller gain is required here than at higher wind speeds, where a small change in pitch can have a large control effect. Hence, in order to change the controller gains according to the current turbine operating point, a gain-scheduling is required. The gain scheduling is based on the current pitch angle and modelled with a data polyfit in the form

$$GK(\beta) = a_2\beta^2 + a_1\beta + a_0, \tag{4-22}$$

for both K_P and K_I separately. The parameters in Equation 4-22 are given in Table 4-3.

Gain	a_2	a_1	a_0
K_P	6.2255	-1.9824	0.9586
K_I	-10.9638	24.2432	0.0759

Table 4-3: Gain scheduling parameters, used in the polynomial given by Equation 4-22.

The K_P (0.4469) and K_I (1.2464) at 11 m/s are then divided by the gain scheduling in Equation 4-22, which is presented in Figure 4-16. The choice of controller gains is crucial to the performance of the controller. With too little overall gain the turbine will wander around the setpoint, while too high chosen gain can make the system completely unstable. Therefore, the controller is first verified in conjunction with the pitch actuators in a hardware-in-the-loop configuration in Chapter 5.

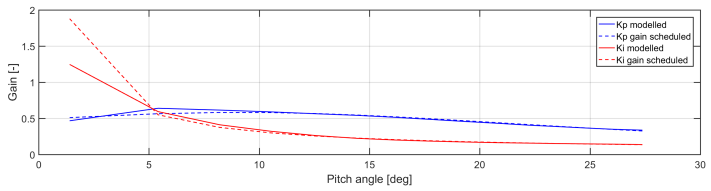

Figure 4-16: Gain scheduled (dashed) en modelled version (solid) of K_P (blue) and K_I (red).

4-5 Yaw controller design

A yaw orientation system is used to keep the DOT500 rotor aligned with the dominant wind direction. The primary component is a large bearing that connects the nacelle frame to the tower. An active yaw drive, containing two yaw motors, drives a pinion gear against a bull gear attached to the yaw bearing (see Figure 4-17). The turbine is said to have a yaw error if the rotor is not aligned to the wind, which implies that a lower share of the available wind energy will be able to be captured by the rotor. The NREL CART3 yaw system, described in [82], is used as basis for the DOT yaw control design.

The goal of the yaw controller is to keep the turbine oriented upwind using non-continuous corrections of yaw angle. The yaw error, which is the difference between the measured wind direction and the yaw angle of the turbine, is measured by the wind vane mounted at the rear of the nacelle. This error is filtered by two low-pass filters in parallel, one with a time constant τ of 60 seconds, and the other 1 second, producing slowly and a more quickly changing measurement of error respectively, presented in Figure 4-18 for clarification. The quickly changing measurement is integrated and monitored. When the integrated error (notated AccErr for accumulated error) reaches a value such that it has been off by 10 deg for 10 min (or much less time for larger errors due to the squaring of the error) the turbine is rotated to the location given by the slowly changing measurement of the error. Finally, the turbine operates within a yaw cone, since the turbine can only yaw two rounds clock and counter clockwise. The ends of this cone are monitored by an encoder. Prior to yawing it is checked whether the desired location is within the allowable cone. If the latter is not the case, the nacelle will rotate in reversed direction to the desired location.

Figure 4-17: One of the two yaw motors driving the small pinion gear against the large bull gear

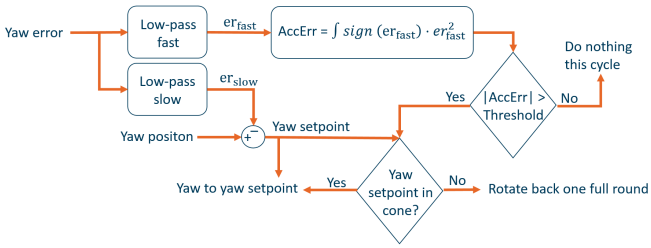

Figure 4-18: Schematic overview of the DOT500 yaw controller design, adapted from [82]

Yaw control is slower than generator torque control and blade pitch control. Since the yaw rate of the DOT nacelle is 0.48 deg/s, investigation of advanced controllers for yaw control provide less potential for improvement compared to controllers for the remaining actuators. This is typically the case for wind turbines, as stated by Pao and Johnson in [79]. Due to its slowness, yaw control is often considered of less interest to control engineers [78]. The effects of yaw misalignments on the loads of the non-rotating turbine parts and the power production are studied in [83]. An improvement of the yaw alignment can be accomplished by using a rotor speed dependent correction factor on the nacelle direction measurement, as explained by Kragh et al. in [82], but this is considered to be out of the scope of this thesis.

4-6 Control software implementation

The operational controllers derived earlier in this chapter now determine how the DOT500 turbine achieves its control objectives in region 2 to 3. On a higher level, supervisory control is introduced in Section 4-6-1. Flowcharts of sub-system controllers are presented in Section 4-6-2. Finally, emergency procedures are addressed in Section 4-6-3.

4-6-1 Global State Machine (GSM) overview

This section outlines the supervisory control of the DOT500, named the Global State Machine (GSM). The top-level control determines when the turbine starts and stops in response to changes in operating conditions or human operator inputs, and also monitors the health of the turbine. Furthermore it manages individual sub-systems, such as the generator and boost pressure systems, which have their own individual controllers. For the DOT500 several global states are introduced, as presented in Figure 4-19.

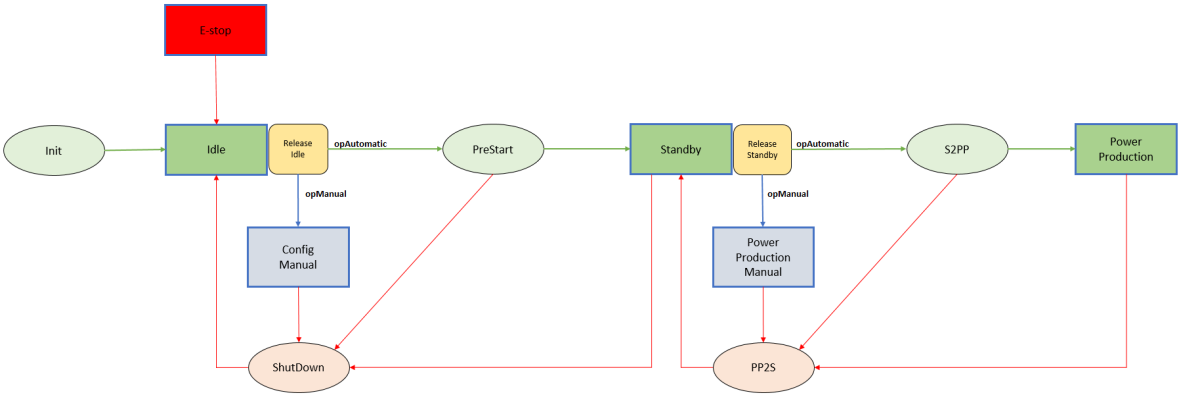

Figure 4-19: Global State Machine of DOT500

The three main states of interest, indicated by the green boxes in Figure 4-19, are:

- **Idle**: the software is initialised.
- **Standby**: all boost systems are running and the turbine is ready to operate.
- **PowerProduction**: the turbine is fully operational in automatic mode.

Forward switching between the three main states is initiated by operator input, indicated by the yellow boxes in Figure 4-19. Backward switching is initiated either trough operator input, or after automatic fault detection. Since the Idle state is considered the safest state, the turbine is always brought back to Idle after fault detection or emergency stops.

Transient states, indicated by circles, are used to switch between the three main states:

- **Init**: Initialisation of software

- **PreStart**: switch on boost and electrical systems in a predefined order (Section 4-6-2)
- **ShutDown**: switch off boost and electrical systems in a predefined order (Section 4-6-2)
- **Standby-to-PowerProduction (S2PP)**: performs rotor start-up sequence.
- **PowerProduction-to-Standby (PP2S)**: performs rotor stopping sequence.

The elapsed time while in a transient state is monitored. Exceeding the allowed forward switching time brings the system back in the previous main state, while exceeding the backward switching time will trigger the emergency stop sequence. In addition, since the DOT500 turbine is an experimental prototype, two manual modes (shown by blue boxes in Figure 4-19) are introduced for manual handling of the turbine's sub-systems:

- **ConfigManual**: manually switch on/off boost systems, without rotor movement.
- **PowerProductionManual**: manually operate all operational controllers of the wind turbine (spear valves, pitch, yaw), under the condition that all boost systems are running. Rotor movement is allowed in this state.

As is observed in Figure 4-19, it is not possible to switch to the next main state via the manual states. For switching between main states it is required to run through the automatic sequence and corresponding safety barriers. This extra safety procedure is inserted to overcome human operator error. Finally, in the Global State Machine the machine health is continuously monitored. Three fault detection levels are used:

- **Code Yellow**: warning only.
- **Code Orange**: automatically return back to Idle.
- **Code Red**: emergency procedures activated.

All alarms require a manual reset from the operator, before the system can switch again forward to the next main state. Code Orange triggers a two-stage stopping procedure. First priority is to bring the rotor to a full stop through the PP2S state. Once the rotor is at standstill, the turbine is brought to Idle via the ShutDown transient state. Emergency stop procedures will be discussed in Section 4-6-3.

Finally, the function of the derived operational controllers earlier in this chapter is defined for every global state. Yawing of the nacelle is allowed in all stable states, except Idle. In this way, the rotor is always aligned with the dominant wind direction before automatic power production, or moved from the wind when required during manual operation. The rotor start-up sequence is performed in the transient state S2PP. In power production the DOT500 rotor is controlled with both spear valve and pitch control, as described earlier in Section 4-3 and 4-4, enabling variable speed operation below rated wind speed and blade pitch control to limit power between rated and cut-out wind speed [84]. The PP2S state main objective is stopping the rotor, which is done by pitching the blades to their feather position during normal operation or by the emergency stop procedures described in Section 4-6-3.

4-6-2 Individual State Machine (ISM) of turbine sub-systems

In addition to the Global State Machine (GSM) described in the previous section, several sub-systems have their Individual State Machine (ISM). The ISM controls the specific sub-system and monitors its status. The ISM configuration is outlined in Figure 4-20.

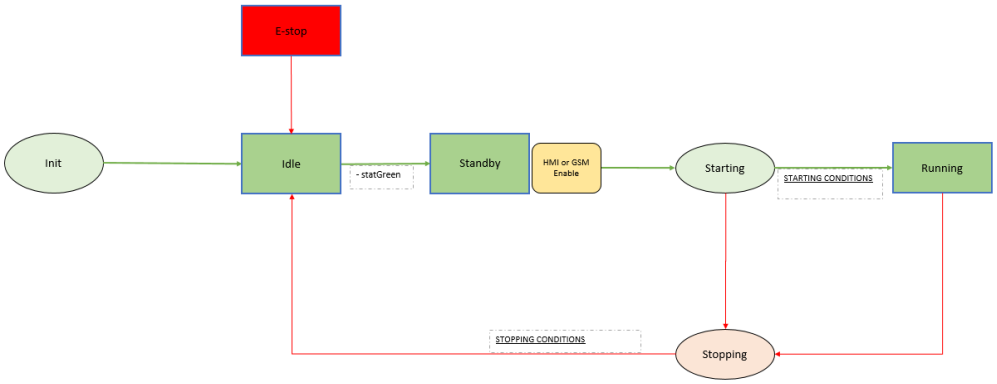

Figure 4-20: Individual State Machine of DOT500 sub-systems

Three main stable states are defined in each ISM, which are indicated by the green boxes in Figure 4-20.

- **Idle**: sub-system is initialised and waiting for operator to reset alarms.
- **Standby**: sub-system is warning free and ready for operation.
- **Running**: sub-system is fully operational.

Forward switching between the Idle and Standby state is controlled automatically, solely based on the system health. This threshold requires the operator to check and reset all alarms, before sub-systems are able to operate. Releasing the ISM Standby state requires automatic activation from the GSM or manually from the operator. The sub-system transient states, indicated by circles, are:

- **Starting**: sub-system is waiting for transition to Running state until starting conditions are fulfilled
- **Stopping**: sub-system is waiting for transition to Idle state until stopping conditions are fulfilled

Three main sub-systems are defined: the generator (ELEC), the water boost pressure system (WATER), and the Hydraulic Power Unit (HPU) of the oil loop. Each sub-system has its own starting and stopping conditions, which are summarized in Table 4-4. The sub-system has to fulfill all starting conditions once its starting timer has elapsed, otherwise the turbine is brought back to the Idle state according to the GSM. In contrast, the sub-systems are held in their stopping state until it is considered safe to switch them off.

Sub-system	Starting Conditions	Stopping Conditions
HPU	Starting timer elapsed Oil boost pump 1 ON Oil boost pump 2 ON Oil pump feed pressure > low threshold	Rotor at standstill ELEC in Idle or Standby GSM in Shutdown, Config or Estop
ELEC	HPU running Starting timer elapsed Brake resistor fan ON Generator ON	WATER in Idle or Standby GSM in Shutdown, Config or Estop
WATER	ELEC running Starting timer elapsed Water boost pump ON Water pump feed pressure > low threshold	Kamat water pump OFF Water feed pressure < threshold GSM in Shutdown, Config or Estop

Table 4-4: Starting and stopping conditions for Individual State Machines

4-6-3 Fault detection and emergency stop procedures

The DOT500 software design includes an extensive alarm list, which links fault detection measurements to the corresponding alarm level. Most turbine fault detection is done by comparing measured states to allowable limits (thresholding) and by comparing related sensors. Failure detection of safety-critical sensors is carried out by using redundant sensors; e.g. the rotor speed is measured with two different speed sensors, of which one is used as control input and the other is used for fault detection only. Three fault detection levels are used:

- **Code Yellow**: warning only.
- **Code Orange**: automatically return back to Idle.
- **Code Red**: emergency procedures activated.

The first alarm level, Code Yellow, is only used to warn the human operator that a measured state nears a critical value. Once the measured state exceeds its threshold value, a Code Orange procedure is activated in order to stop the turbine. The Code Orange shutdown procedure is identical to normal turbine shutdown and runs through the states PP2S-Standby-Shutdown of the global state machine, to return to the turbine Idle state. An example of a normal turbine shutdown procedure is given in Figure 4-21.

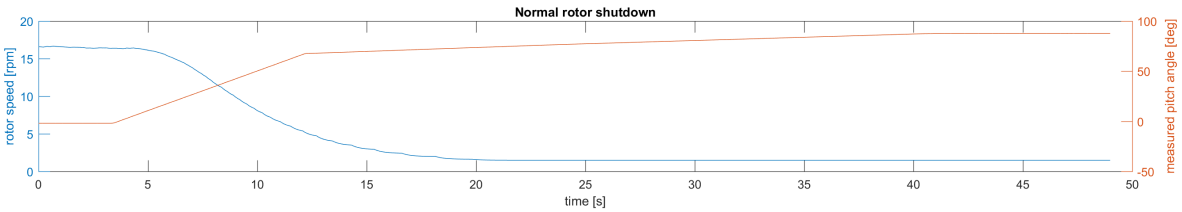

Figure 4-21: Normal rotor shutdown procedure after 3 s: blades are pitched to feather position, with a lower pitch rate saturation of 0.65 deg/s between 66 - 88 deg in order to reduce loads.

In Figure 4-21, a Code Orange alarm is triggered after 3 s. A rotor shutdown is subsequently enforced by pitching the blades to their feather position (displayed in red). This is first done

with a pitch rate of 8 deg/s, until the measured pitch angle is 66 deg. Thereafter, the blades are returned to feather with a lower pitch rate of 0.65 deg/s, in order to reduce loads on the pitch actuator. Finally it is observed that after 20 s the rotor is in standstill position, while it takes about 35 s to fully pitch the turbine to feather (88 deg).

A Code Red alarm is triggered either when the turbine rotor or sub-systems failed to stop during normal shutdown, after an unsuccessful Code Orange procedure, directly at several dangerous threshold exceedances, or by the human operator. Code Red alarms bring the turbine in its emergency stop procedure, which is executed in three sequential steps. In the first step, a pitch emergency stop is enforced. An example of this is given in Figure 4-22.

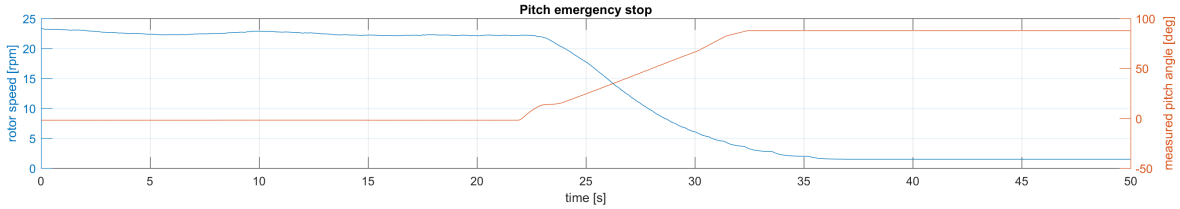

Figure 4-22: Pitch Emergency stop: blades are pitched to feather position at full pitch rate.

Once the pitch emergency stop is triggered, rotor deceleration is monitored by the global state machine. The main difference between normal and emergency shutdown is the rate of shutdown. Emergency shutdown slows the turbine as fast as possible by pitching all blades to feather at the maximum pitch rate (8 deg/s). When no deceleration is detected after 5 s, or when the rotor is not in standstill position after 45 s, a hydraulic emergency stop is enforced as back-up option in the second emergency step. This is done by choking the high-pressure oil line, of which an example is given in Figure 4-23.

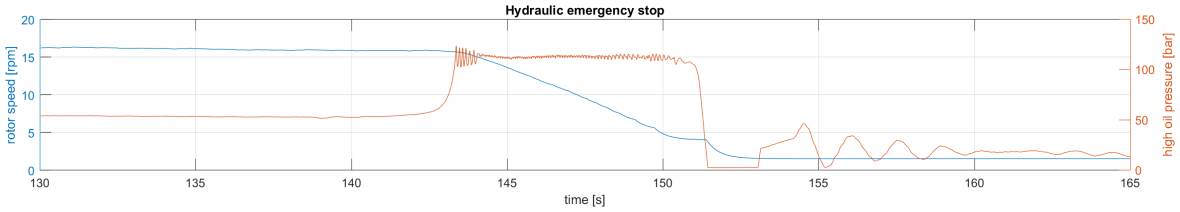

Figure 4-23: Hydraulic Emergency stop at 140 s: choking the high-pressure oil line results in increased system braking torque, which decelerates the rotor to standstill.

In Figure 4-23, an hydraulic emergency stop is enforced at approximately 140 s. The high-pressure oil line is choked, which is observed by the pressure build-up in the high-pressure oil line (displayed in red). This results in increased system braking torque, which decelerates the rotor to standstill position at 153 s (displayed in blue). The hydraulic emergency stop only serves as a back-up option to the pitch emergency stop, but its functioning appeared reliable during multiple tests (of which the data is attached in Appendix C).

Once the rotor is at standstill, the system switches to the final Estop ALL state in which all hardware is turned off as fast as possible. This state also functions as a last resort, while having a rotating rotor, once the other mentioned stopping methods where ineffective. The latter is however highly undesirable and should only be used once all the aforementioned methods are insufficient.

Chapter 5

DOT500 preliminary experiments

This chapter describes the preliminary experiments, which are used to design and test controllers for the DOT500 turbine. The main objective is to identify the steady-state Power Transmission System (PTS) characteristics, which are used in the spear valve torque controller implementation. In addition, a hardware-in-the-loop rotor model is developed, to gain experience with both the PTS system and blade pitch actuators in a controlled transient environment.

First, in Section 5-1, the steady-state mapping of the PTS response is examined. Next, in Section 5-2, a theoretical estimation of the turbine rotor mass moment of inertia is validated through experiments. This estimation is required in Section 5-3 for the development of a rotor model, which is used to simulate dynamic load cases on the power transmission in a hardware-in-the-loop configuration. Finally, in Section 5-4, dynamic load cases are performed on the pitch actuators at a stationary rotor.

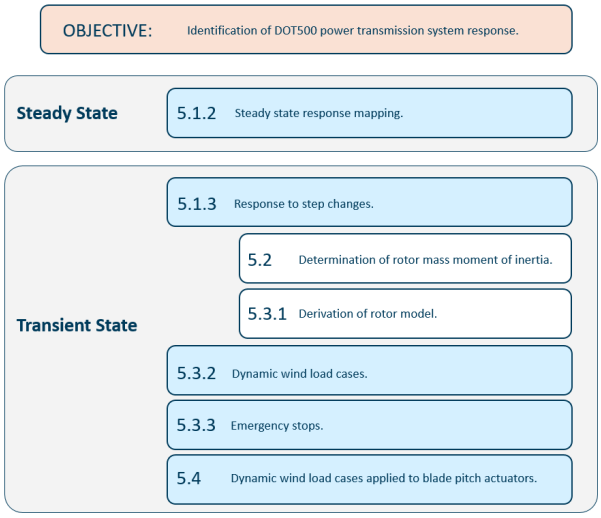

Figure 5-1: Chapter outline

5-1 DOT500 Power Transmission System (PTS) response

As described in Chapter 4, the hydraulic PTS torque mapping on the rotor-speed-versus-spearvalve-position plane is essential to construct the below-rated torque control law. This section summarizes the steps taken to obtain this mapping. First, in Section 5-1-1, the power transmission test set-up is explained. Then, in Section 5-1-2, the steady-state tests are outlined. Finally, in Section 5-1-3, transient stair-case tests are conducted on the transmission.

5-1-1 Transmission set-up overview

The complete hydraulic transmission system is constructed and tested separately in the form of an indoor set-up, in which a 500 kW electro-motor is used to simulate the rotor. This set-up allows for close observation of the transmission system in a more controlled environment. A simplified hydraulic diagram is given in Figure 5-2, a photo is presented in Figure 5-3.

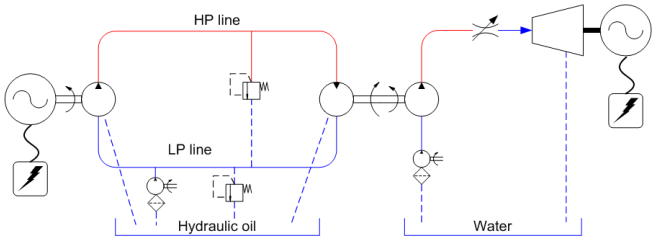

Figure 5-2: Simplified hydraulic diagram of the power transmission system [1]

The original Vestas V44 gearbox is attached backwards to the electro-motor, in order to decrease the input rotation speed and increase the input torque, which drives the Hägglunds CB840 oil pump. The oil pump then drives the Rexroth A6VLM oil motor by means of a hydrostatic transmission. The oil motor is mechanically linked to the Kamat water pump, which pressurizes the water inlet flow. The high-pressure water line is controlled by two adjustable spear valves, which transmit the fluid power to the Pelton turbine by means of hydrodynamic transmission. Finally, a Motec 400kW electro-motor, connected to the Pelton turbine, is used as electrical generator.

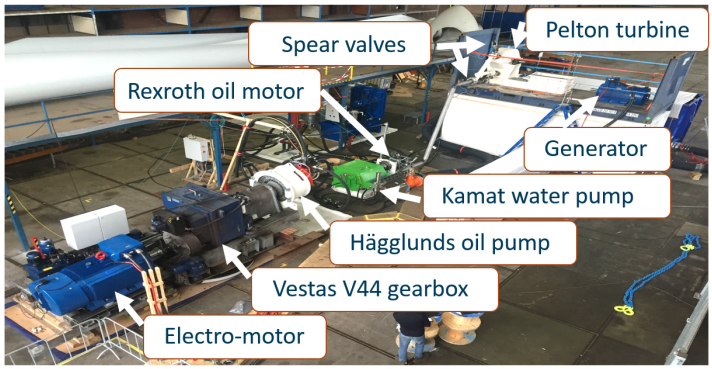

Figure 5-3: Photo of the power transmission system test set-up. The electro-motor, in combination with the reversed Vestas V44 gearbox, simulates the rotor.

Inputs

The test set-up can be controlled with a number of input parameters, of which two are chosen as the variable parameters for the tests described in the remainder of this section. These are:

- Rotor-motor speed setpoint [RPM]: the electro-motor is tasked to maintain an adjustable rotation speed, and is allowed to use 100% of its available torque. The maximum setpoint is 1500 RPM, the minimum setpoint is 0 RPM.
- Spearvalve travel setpoints [mm]: the two spearvalve setpoints can be adjusted separately to alter the nozzle diameter. The maximum spear travel setpoint is 26 mm (fully open), and the minimum is 0 mm (completely closed). Lowering the spear valve travel setting leads to a decreasing effective nozzle area/diameter. The relation between spear valve travel position and the effective nozzle area is given in Figure 5-4 and 5-5.

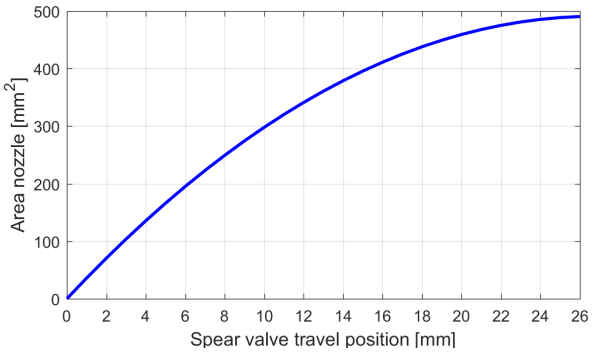

Figure 5-4: Relation between spear valve travel position and nozzle area

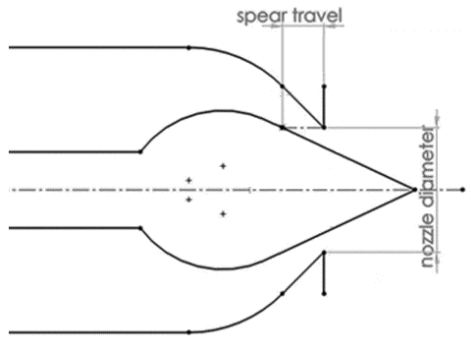

Figure 5-5: Schematic visualisation of spear valve configuration

Outputs

The main outputs that are used in the indoor PTS tests are:

- Hägglunds (rotor) speed [RPM]
- Hägglunds feed oil pressure [bar]
- Hägglunds discharge oil pressure [bar]
- Spearvalve measured position [mm]
- Kamat discharge water pressure [bar]

where the Hägglunds speed represents the rotor speed measurement. As the torque readings from the electro-motor appeared to give unreliable measurements, the system torque is calculated from the pressure difference over the Hägglunds oil pump by

$$\tau_{\mathrm{p}} = \frac{\Delta p_{\mathrm{p}} V_p}{\eta_{\mathrm{m}}(\omega)}, \tag{5-1}$$

where Δp_{p} is the measured pressure difference over the oil pump in [Pa], V_{p} the volumetric displacement in [m^3/rad] and $\eta_{\mathrm{m}}(\omega)$ represents the mechanical efficiency of the pump. The pump efficiency is provided by the manufacturer and is a function of the rotational speed ω.

5-1-2 Steady state system response

In this section, the system torque is evaluated over a grid of available rotational speeds and spear valve settings. This grid search based result is used to augment the standard torque control law. With the latter in mind, a distinction in operation area is made between (1) the area around maximum C_p-tracking of the Vestas V44 rotor torque characteristics in below-rated conditions and (2) around the rated-speed operation range. The grid search is performed according to the following 4 steps:

1. Set the electro-motor to a predetermined rotational speed.
2. Apply a stair-case signal over the desired spear valve position range.
3. Measure the pressure over the Hägglunds oil pump, which is translated to torque using Equation 5-1.
4. Repeat step 1-3 for the whole set of desired rotational speeds.

The range of rotational speeds is kept bounded by the rated-speed (28 RPM) of the Vestas V44 rotor. Due to practical limitations of the electro-motor, the minimum speed was 5.7 RPM, which is well below the expected operational speed of the DOT500 turbine after start-up.

Below-rated rotor speed

To gather some first insights, one spear valve was incrementally opened whereas the second remained closed in the first test. The minimum spear valve position was restricted by the torque limit the electro-motor could deliver and was opened in steps of approximately 0.5 mm until the maximum 26 mm setpoint. The rotor speed is taken in steps of 2 RPM. In Figure 5-6 the system torque results are displayed in *red* and compared to the theoretical maximum attainable torque from the Vestas V44 rotor at the maximum power coefficient in *blue*.

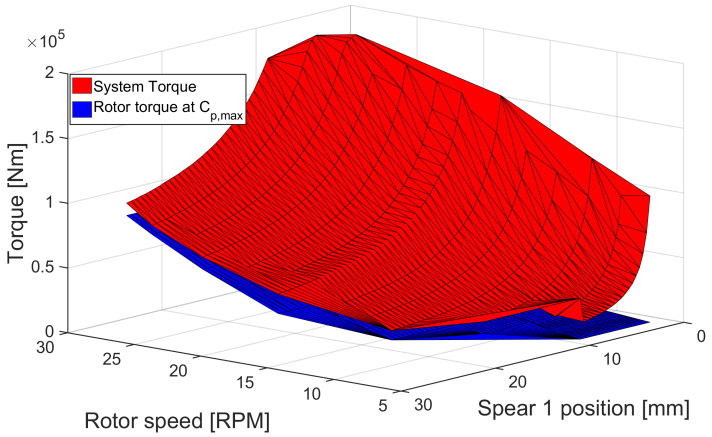

Figure 5-6: System torque response with 1 varying spear valve in *red*, as a function of rotor speed and spear valve position. The second spear valve is remained closed. Results are compared to the theoretical maximum attainable torque from the Vestas V44 rotor at fine-pitch in *blue*.

From Figure 5-6 it is clear that when only 1 spear valve is used, the system torque is always larger than the maximum attainable rotor torque at fine-pitch, meaning that it is not possible to operate at $C_{\mathrm{p,max}}$. As mentioned in Section 4-4, higher rotor torques are obtained at different pitch angles. Deviating from $C_{\mathrm{p,max}}$ by choosing a different fine-pitch angle would thus allow the turbine to start and operate, but at reduced rotor power efficiency. Therefore, in the second test both spear valve setpoints are varied simultaneously and identically in order to allow for a larger effective nozzle diameter. The results of this second test are presented in Figure 5-7.

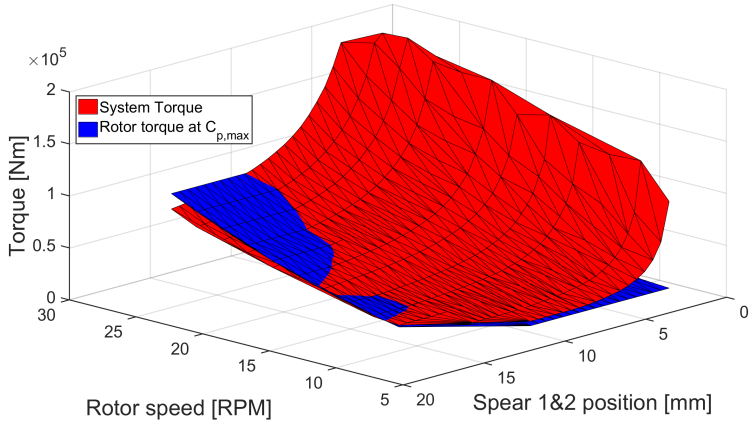

Figure 5-7: System torque response with 2 spear valves varying simultaneously in *red*, as a function of rotor speed and spear valve position. Compared to the theoretical maximum attainable torque from the Vestas V44 rotor at fine-pitch in *blue*.

In comparison with the first experiment more useful results are observed in Figure 5-7, since this time an intersection between the system and rotor torque plane is present. This intersection is examined in more detail in the third test, this time with a more accurate rotor speed step size of 1 RPM and a spear valve step size of 0.2 mm. The results of this finer grid search are presented in Figure 5-8.

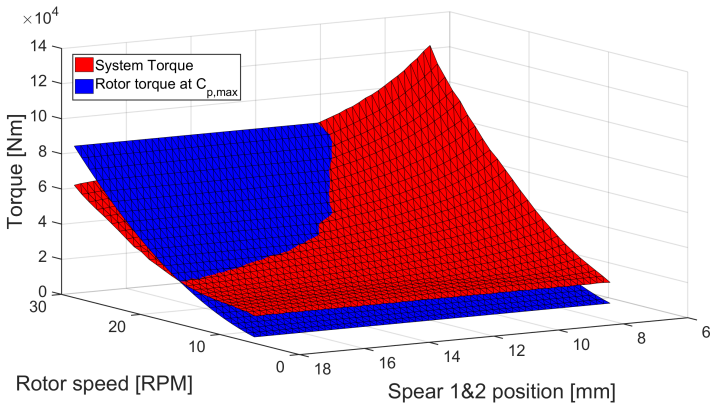

Figure 5-8: System torque response with 2 spear valves varying simultaneously around the $C_{\mathrm{p,max}}$ plane intersection, this time using a smaller grid size in order to increase accuracy.

Rated rotor speed

Once the rotor approaches rated speed, it is allowed to further increase its torque until rated power is obtained. In the fourth and final test, a similar mapping is made around the rated RPM of the rotor. The rotor speed is ramped from 25.5 to 28.5 RPM in steps of 0.5 RPM. The spear valve position is varied with steps of 0.17 mm. The results are depicted in Figure 5-9. The results were limited by the rotor-motor torque limitation and/or pressure relief valve, which is visible in the rounding of the system torque at spear valve settings lower than 5 mm.

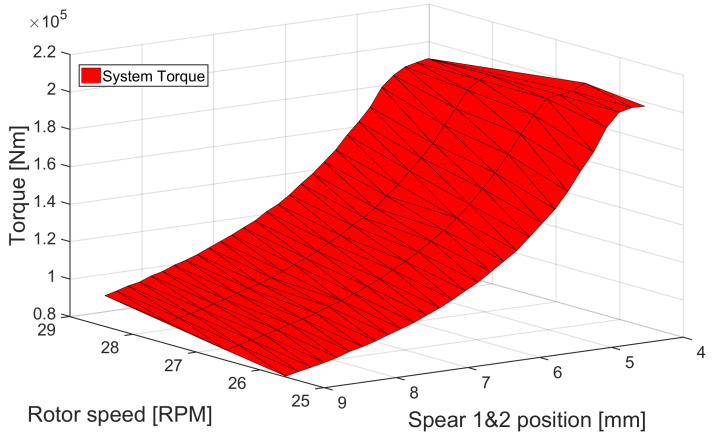

Figure 5-9: System torque response with 2 spear valves varying simultaneously, at different rotor RPM setpoints around maximum rotor speed.

Above results are combined in Figure 5-10, which shows the system response torque over the Vestas V44 operating range to the extend possible with the indoor test set-up. From this figure it is derived that the system is able to operate at its maximum rotor efficiency from 15 RPM (which corresponds to a wind speed of 4.6 m/s at a tip-speed ratio of 7.55), followed by maximum C_{p}-tracking along the intersection of the two planes, and finally moving to rated power by further torque increase while deviating from the $C_{\mathrm{p,max}}$ intersection.

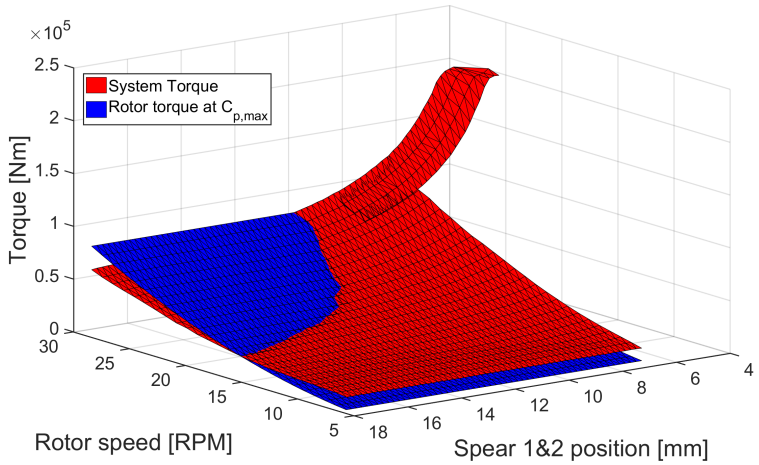

Figure 5-10: Combined system torque response with 2 spear valves varying simultaneously, mapped over the Vestas V44 operating range to the extend possible on the indoor test set-up.

5-1-3 Transient state system response

The goal of the transient state tests is to obtain first insights in the spear valve tracking capability and the transient effect on the system pressures. This first transient state test consists of measuring the system response to an immediate stair-case setpoint change of the two spear valves. The rotational speed is kept fixed during the test at a predefined RPM. Tests are repeated at different rotational speeds, but results show similar time-domain characteristics as for the 22 RPM case, which is presented in Figure 5-11.

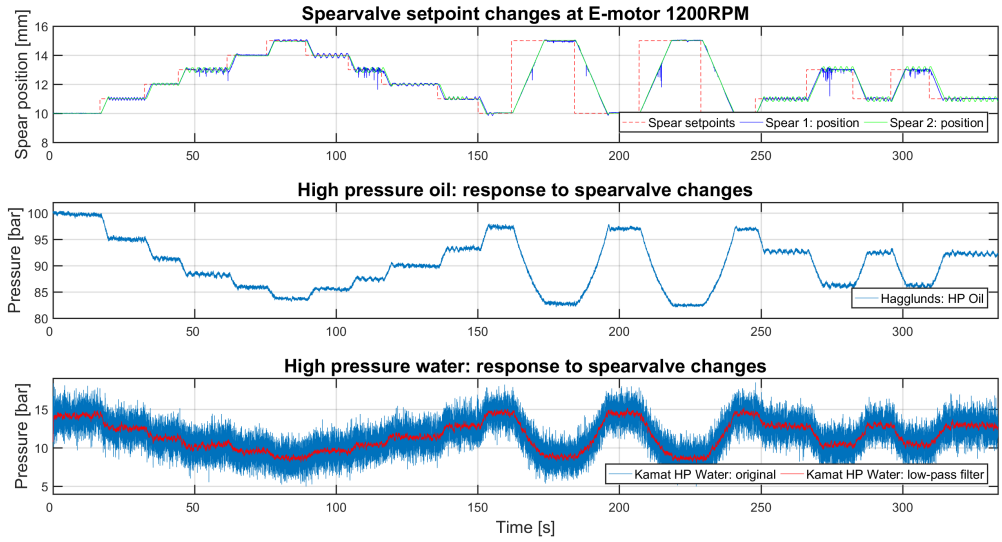

Figure 5-11: *Top*: transient response of spear valves to setpoint changes; *middle*: transient response of high-pressure oil; *bottom*: transient response of high-pressure water.

From Figure 5-11 it is observed that the spear valves are only able to track a setpoint change with a maximum rate of 2.4 mm/s, which is in line with the spear actuator data sheet. Furthermore, the high-pressure water measurement is noisy, caused by the use of a high-range, low-resolution sensor. This led to the use of a low-pass filter for better evaluation of the signal. Finally, in Figure 5-11, small fluctuations around steady states are found in both the spear valve positions, the high-pressure oil line and the high-pressure water line.

The reason for these resonances was found in the constant on and off-switching of the spear valve actuators, to keep their position near the given setpoint. To overcome this problem, a deadband around the spear valve setpoint is implemented, as depicted in Figure 5-12. The spear valve now only reacts when its position is located outside the deadband, and switches on in the direction of the setpoint until the setpoint is crossed.

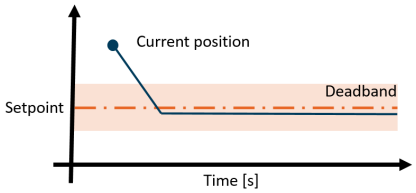

Figure 5-12: Spearvalve deadband implementation

5-2 Estimation of rotor mass moment of inertia

In order to simulate more realistic transient scenarios than the step responses of the previous section, a turbine rotor model is developed based on Newton's second law of rotation. This model, however, requires an estimation of the DOT500 rotor mass moment of inertia. Therefore, a theoretical approximation of this parameter is derived in Section 5-2-1, which is afterwards compared to DOT500 field data in Section 5-2-2.

5-2-1 Theoretical approximation

The rotor mass moment of inertia has an important influence on the time response of pressure and rotational speed, leading to a slower but smoother response of the system. The rotor inertia acts as a low-pass filter to high-frequent wind speed variations on the rotor speed, dampens pressure changes and allows active pressure control by spear valves [1]. Dynamic analysis in [85] showed that the parameter that sets the main characteristics of a wind turbine is the aerodynamic rotor with its large inertia. The rotor inertia and associated damping is therefore an important parameter to include in turbine simulations. Rodriquez et al. presented in [86] a method to estimate the inertia constant J for a generic blade using the turbine blade mass and length with the formula:

$$J = K_J M L^2, \tag{5-2}$$

where M and L are the blade mass and length respectively. $K_\mathrm{J} \approx 0.212$ is an empirical constant, for which in [86] a distribution is given based on blade length. The distribution gives rise to $K_\mathrm{J} = 0.222$ (20 meter blade) and $K_\mathrm{J} = 0.197$ (for a 62 meter blade).

Equation 5-2 is applied to several known turbines and compared to their actual mass moment of inertia. The resemblance with the inertia from data sheets is given in:

Turbine	**Blade Length [m]**	**Resemblance [%]**
NREL 5MW	61.5	112
Vestas V90	43	96.6
Vestas V80	38.75	103.9
Vestas V66	32.15	121.6
Vestas V44	21.7	-
CART3 (600kW)	20	122.9

Table 5-1: Resemblance between actual blade mass moment of inertia and the proposed method.

To go from a single blade inertia to full rotor inertia, the inertia in Equation 5-2 is multiplied by the amount of blades and an extra 10% is added to include for hub and shaft inertia. The overall inertia resemblance for the CART3 turbine then becomes 103.5%.

Since for the DOT500 turbine only the blade mass and length are known, which are both in the same order of magnitude as the CART3 turbine, the above method is used to get an estimate of the DOT500 rotor mass moment of inertia. This inertia is approximated by $6.6 \cdot 10^5\,\mathrm{kgm}^2$. This theoretical result is validated with field recorded data in the next section.

5-2-2 Experimental approximation

The purpose of the experimental test in this section is to determine the mass moment of inertia of the DOT500 turbine rotor. The inertia constant is derived from Newton's second law of motion, with the use of field recorded measurements. The relevant measurement data is obtained during emergency stop tests. Results are compared with the theoretically derived result of the previous section.

Test Outline

The rotor mass moment of inertia J is the parameter of interest. The rotor speed ω and pressure difference over Hägglunds pump Δp_{p} are obtained through measurements. The rotor shaft torque τ_{shaft} is measured through load pins, which are located between the pump and its support structure (forces acting on the load pins are denoted by F_{L} in Figure 5-13). The pump volumetric pump displacement $V_{\mathrm{p}} = 0.0084\,\mathrm{m}^3/\mathrm{rad}$ is taken from manufacturer data.

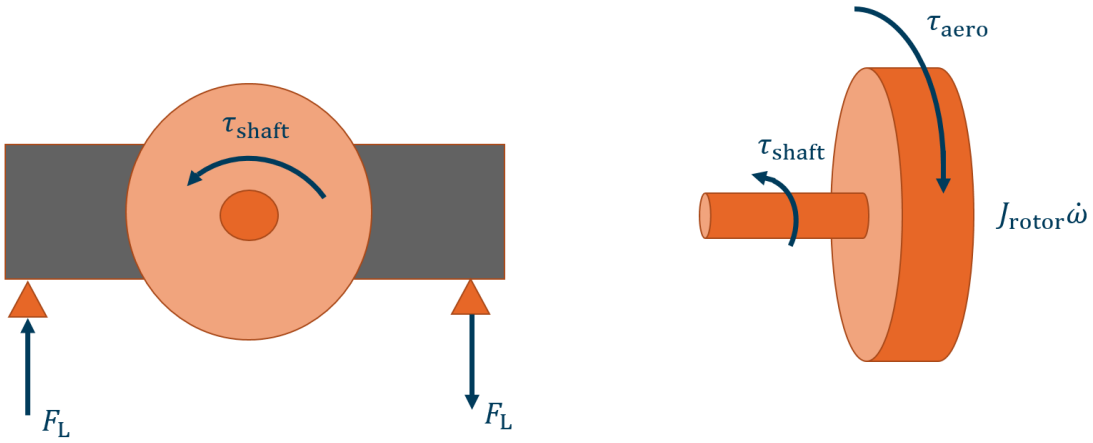

Figure 5-13: Free body diagram of *left* the Hägglunds pump and *right* the DOT500 rotor

The relation between between the rotor aerodynamic torque and the measured shaft torque is depicted on the *right* of Figure 5-13 and derived from Newton's second law of motion

$$J\dot{\omega} = \tau_{\mathrm{aero}} - \tau_{\mathrm{shaft}}, \tag{5-3}$$

which suggests that the shaft and rotor torque are equal in steady state, once the rotor acceleration $\dot{\omega}$ is equal to zero. Hence, in steady state, the aerodynamic rotor torque is measured from the load pins. Furthermore, in steady state, the system torque acting on the Hägglunds support structure should be equal to the shaft torque. If the latter would not be the case, the Hägglunds pump would rotate. A theoretical expression for the system reaction torque is derived from the pressure difference over the Hägglunds pump and given by

$$\tau_{\mathrm{system}} = \frac{\Delta p_{\mathrm{p}} V_{\mathrm{p}}}{\eta_{\mathrm{m}}}. \tag{5-4}$$

The mentioned steady state assumption, that the system torque should be equal to the aerodynamic torque, is used to derive the pump efficiency η_m at the steady state operating point. Finally, the relation between aerodynamic and system torque is given by

$$J\dot{\omega} = \tau_{\text{aero}} - \tau_{\text{system}}, \tag{5-5}$$

and is approximated by

$$J\frac{\Delta\omega}{\Delta t} = \tau_{\text{aero}} - \tau_{\text{system}}, \tag{5-6}$$

which is rewritten in order to obtain the required rotor mass moment of inertia

$$J = \frac{(\tau_{\text{aero}} - \tau_{\text{system}})\Delta t}{\Delta\omega}. \tag{5-7}$$

In Equation 5-7 the aerodynamic rotor torque is now assumed constant at the measured steady state value, whereas the system torque is measured from the system pressures according to Equation 5-4.

Hydraulic emergency stop tests are conducted by choking the high-pressure oil line. An example is of this experiment is given in Figure 5-14, where at 142 s the choking is applied. The result is an increase of pressure and thereby system braking torque. Once the system braking torque becomes greater than the aerodynamic torque, the rotor speed decreases. The rotor deceleration is presented in the lower plot of Figure 5-14. The data required for Equation 5-7 is highlighted.

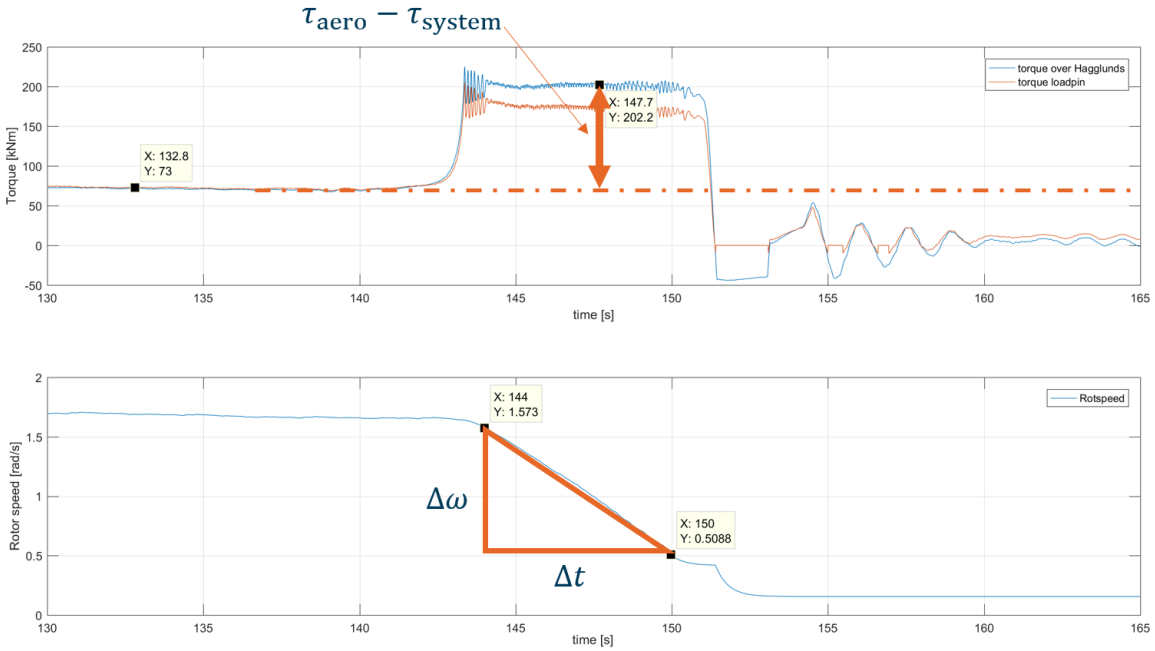

Figure 5-14: Data and calculation example of rotor mass moment of inertia test.

Results

The mentioned test is repeated eight times, of which the data and calculations are attached in Appendix C. The results of this appendix are summarized in Table 5-2.

Test number [-]	**1**	**2**	**3**	**4**	**5A**	**5B**	**6**	**7**	**8**
Inertia [$\times 10^5$ **kgm^2**]	5.9	11.3	6.6	5.6	7.8	6.0	7.0	6.1	7.2

Table 5-2: Calculation results of rotor mass moment of inertia tests

In test number 5 the calculation was repeated on two different sections, due to a jump in both the deceleration and pressure measurement. Averaging the results of Table 5-2 leads to a mass moment of inertia of $7.1 \cdot 10^5\,\mathrm{kgm}^2$.

Finally, the result of test 2 is believed to be higher due the fact that the test did not start from an exact steady state. Data of this test is given in Appendix C. Leaving test 2 out of the results would even lead to an average mass moment of inertia of $6.5 \cdot 10^5\,\mathrm{kgm}^2$. Either way, the experimental derived mass moment of inertia is in the same order of magnitude as the theoretical calculated value of the previous section.

It should be noted that both the constant aerodynamic torque assumption and the inertia calculations are very imprecise. They do show however that the theoretical calculated value of the previous section is in the same order of magnitude as the experimentally derived rotor mass moment of inertia and the rough estimation therefore seems reasonable to use in the rotor model.

5-3 Dynamic load cases on transmission with rotor model simulations

As the indoor power transmission system (PTS) set-up is driven by an electro-motor, the system response to actual rotor dynamics is unavailable. The purpose of applying a rotor model to the PTS set-up is to gain experience with the system under realistic wind scenarios.

To simulate environmental conditions and rotor characteristics on the indoor test set-up, a rotor-model is derived in Section 5-3-1. This model calculates the required rotational speed of the low-speed rotor shaft, while using the system state and a predefined wind signal as inputs to the model. In Section 5-3-2 dynamic wind load simulations are outlined. Furthermore, in Section 5-3-3, emergency stop simulations are performed.

5-3-1 Rotor model with hardware-in-the-loop configuration

An aerodynamic wind turbine simulation model is constructed to perform a hardware-in-the-loop simulation on the indoor test set-up. The model is implemented in `Python` [87] and data is exchanged with the Programmable Logic Controller (PLC) using the ModBUS communication protocol [88]. The implementation of the rotor model in-the-loop configuration is given in Figure 5-15, and its derivation is given in a series of relations below.

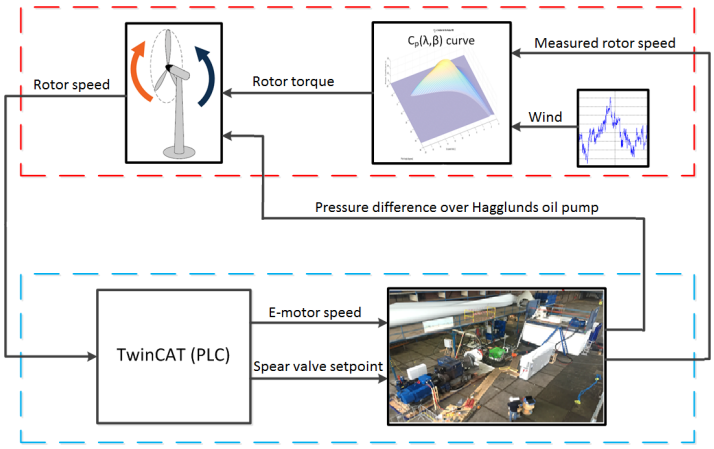

Figure 5-15: Rotor model-in-the-loop implementation scheme. The red box contains all rotor model software components, including Newton's second law for rotation, power coefficient evaluation and wind speed input. The blue box includes all hardware components of the PTS system, interacting with the PLC software.

The system torque is calculated from the pressure difference over the Hägglunds oil pump by

$$\tau_{\mathrm{p}}[k] = \frac{\Delta p_{\mathrm{p}}[k] V_{\mathrm{p}}}{\eta_{\mathrm{m}}(\omega)}, \tag{5-8}$$

where k is represents the index value of the fixed time step simulation, Δp_{p} is the measured pressure difference over the oil pump, V_{p} the volumetric displacement and $\eta_{\mathrm{m}}(\omega)$ represents the mechanical efficiency of the pump. The pump efficiency is provided by the manufacturer and is a function of the measured rotor speed ω.

The simulated tip-speed ratio λ is calculated using

$$\lambda[k] = \frac{\omega[k]R}{V[k]}, \tag{5-9}$$

where R represents the DOT500 rotor radius and V a simulated wind signal. Using this tip-speed ratio, the aerodynamic rotor torque τ_{aero} is evaluated by

$$\tau_{\text{aero}}[k] = \frac{1}{2}\rho_{\text{air}} V[k]^2 \pi R^3 \frac{C_p(\lambda[k])}{\lambda[k]}, \tag{5-10}$$

where ρ_{air} represents the air density and $C_{\text{p}}(\lambda)$ the rotor power coefficient as function of the tip-speed ratio λ only, taken from a lookup function at a fixed fine-pitch angle. Finally, a discretized version of Newton's second law of motion rotation is used for calculation of the required rotational speed for the next time step according to

$$\omega[k+1] = J^{-1}(\tau_{\text{aero}}[k] - \tau_{\text{system}}[k])\Delta t + \omega[k], \tag{5-11}$$

where J is the rotor mass moment of inertia estimate, which was derived in Section 5-2. The rotational speed setpoint is given to the electro-motor that drives the PTS test set-up. The derived rotor model, schematically depicted in the *red* box in Figure 5-15, is hence based on the following measured signals and system property data:

1. Simulated wind signal V;
2. Current rotor speed from measurements ω;
3. Pressure difference over the Hägglunds pump, taken from measurements Δp_{p};
4. System properties: rotor radius R, moment of inertia J, volumetric pump displacement V_{p}, pump efficiency η_{m}, air density ρ_{air}, power coefficient C_{p} and tip-speed ratio λ.

The model configuration as derived above is valid for below-rated operation, due to the fixed fine-pitch angle assumption in Equation 5-10. The modularity of the model, however, makes it possible to easily adjust to other configurations. This is done e.g. in Section 5-4, where the model is applied in a hardware-in-the-loop configuration with the DOT500 pitch actuator.

Simulation results are presented in subsequent sections. During these experiments, the main purpose was to gain first experience with the closed-loop system under realistic transient scenarios. In this way, bugs and errors were quickly identified and fixed, without taking the risk of damaging the actual wind turbine by unexpected behaviour. In addition, emergency stop scenarios are simulated on the indoor set-up. Simulation of these scenarios contributed to the design of the emergency stopping procedures, prior to the start of the outdoor DOT500 field tests. Finally, the experimental results are also compared to the actual behaviour of the DOT500, in order to improve the derived model for later use.

5-3-2 Dynamic wind load simulations

In this section two types of simulations are considered. First, a turbulent wind signal is applied to the power transmission system, using passive spear valve control only. This simple example illustrates the effects of the spear valve setpoint on the system dynamics and performance. Second, the effect of the modelled rotor mass moment of inertia on the system dynamics is evaluated and compared to field recorded data of the DOT500.

Turbulent wind with passive nozzle control

The working principle of the hardware-in-the-loop configuration is observed during 10 min of operation. In this test, a turbulent wind signal is applied to the power transmission system according to the method explained in the previous section. The transient system response is evaluated, while using passive spear valve setpoints. Two cases are considered, with a fixed spear valve setpoint of 6 mm and 8 mm respectively. The results are shown in Figure 5-16, where on the left the turbulent wind signal, rotor speed and C_p-trajectory are given. On the right of Figure 5-16, the oil and water high pressure measurements are presented.

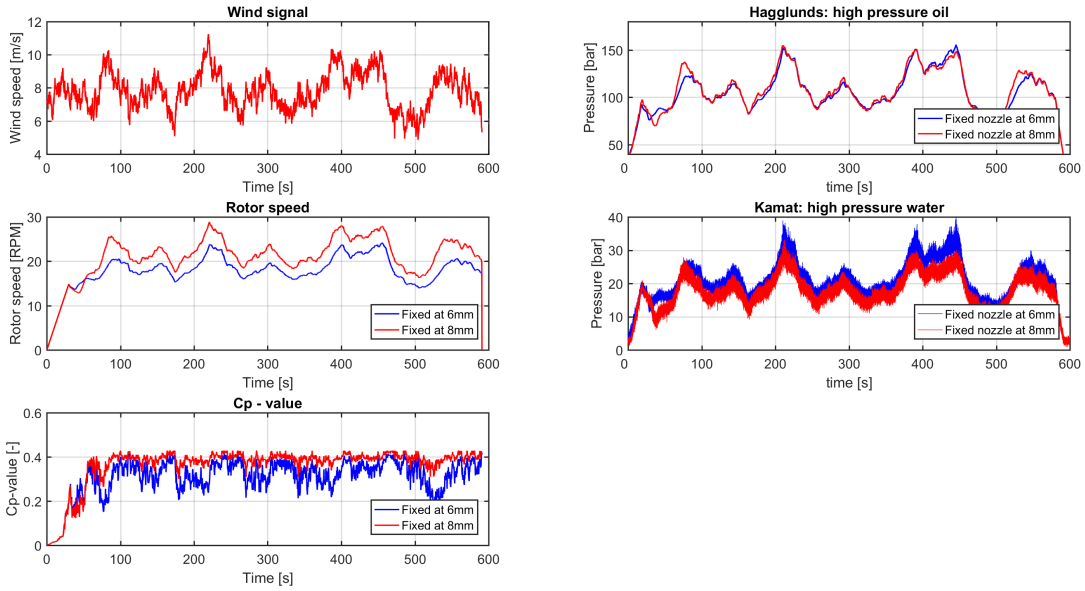

Figure 5-16: Power transmission system response to a simulated wind signal, with fixed spear valve setpoint (6 mm in *blue*, 8 mm in *red*). Lowering the spear valve setting results in higher pressures in the system, resulting in a higher system torque and hence in a lower rotor speed.

First, it is observed in Figure 5-16 that the rotor indeed acts as a low-pass filter to the reaction of the rotor speed to high-frequent wind speed variations. More important, the figure shows that closing the spear valves setting results in increased pressures in the system, resulting in a higher system torque and hence a lower rotor speed. Furthermore, the fixed setpoint at 8 mm results in a higher average C_p-value, but this is correlated to the applied wind signal: using a wind speed with a higher average speed would show results in favour of the 6 mm setpoint. The C_p-graph does show however the importance of choosing the correct spear valve setpoint in attaining the optimal rotor power coefficient.

Effect of mass moment of inertia on system dynamics

In the following test the effect of choosing a different rotor moment mass of inertia is shown. The nominal (*large*) inertia is compared to an inertia (*small*) that is 10 times smaller than the nominal value of $1.4 \cdot 10^5\,\mathrm{kgm}^2$. The same turbulent wind speed signal is applied as model input in both cases. Results are depicted in Figure 5-17.

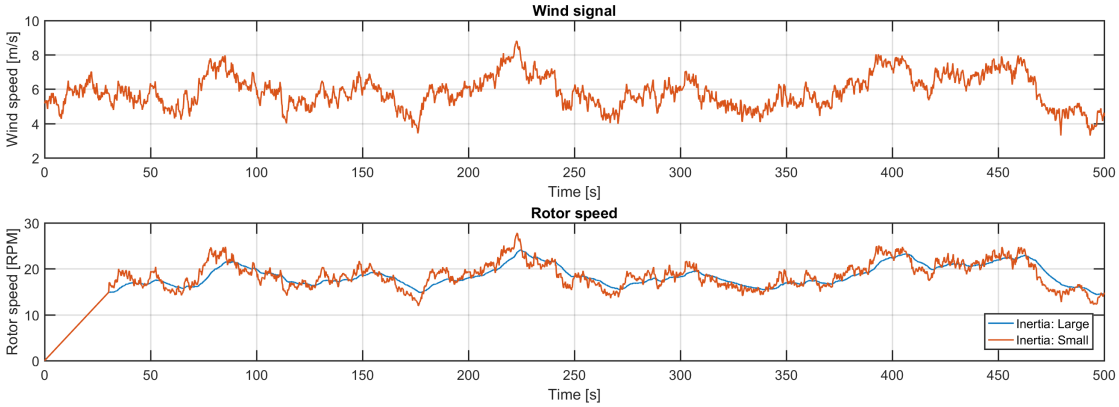

Figure 5-17: Damping effect of rotor mass moment of inertia on modelled rotor speed.

The filtering effect of the rotor mass moment of inertia is observed in Figure 5-17. The mass moment of inertia behaves as the filter cut-out frequency, meaning that a larger inertia adds more damping to wind speed variations. It is therefore important to compare the hardware-in-the-loop results with actual DOT500 rotor dynamics, in order to improve the model.

The inertia relevance is also found in Figure 5-18, where the spear valve responses to the turbulent wind signal are depicted for both the small and large inertia. When the rotor speed changes rapidly, the spear valve actuator bandwidth is insufficient to actively follow the setpoint generated by the rotor speed driven feedforward control law. This is the case for the small inertia in the upper plot of Figure 5-18, where the spear valve position runs continuously behind its setpoint. A larger mass moment of inertia is thus beneficial for the tracking capabilities of the spear valve actuators to the controller setpoints.

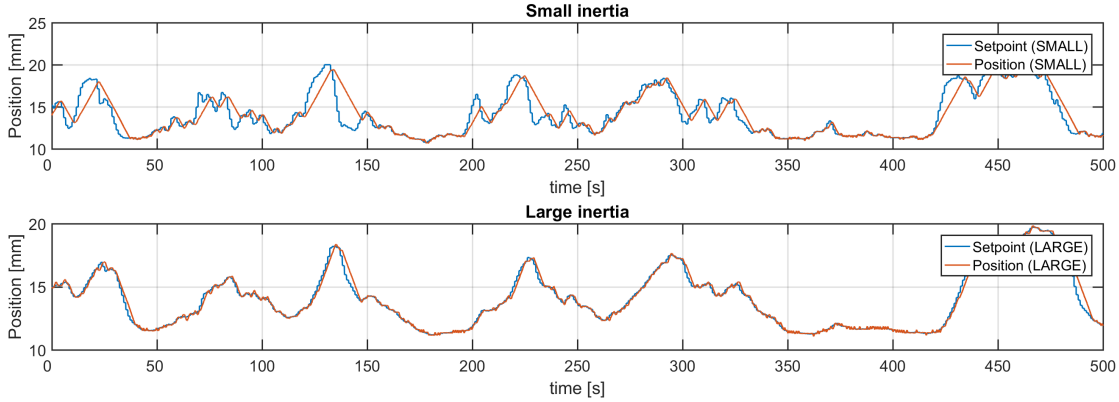

Figure 5-18: Spear valve response with above a *small*, and below a *large* mass moment of inertia. In the upper plot the spear valves are lagging their setpoint, whereas below tracking is possible.

Comparison between rotor model and DOT500 field data

Actual DOT500 field data is used afterwards to validate the hardware-in-the-loop system dynamics. A field recorded data set of equal length and similar wind conditions as in Figure 5-17 is selected, which is depicted in Figure 5-19.

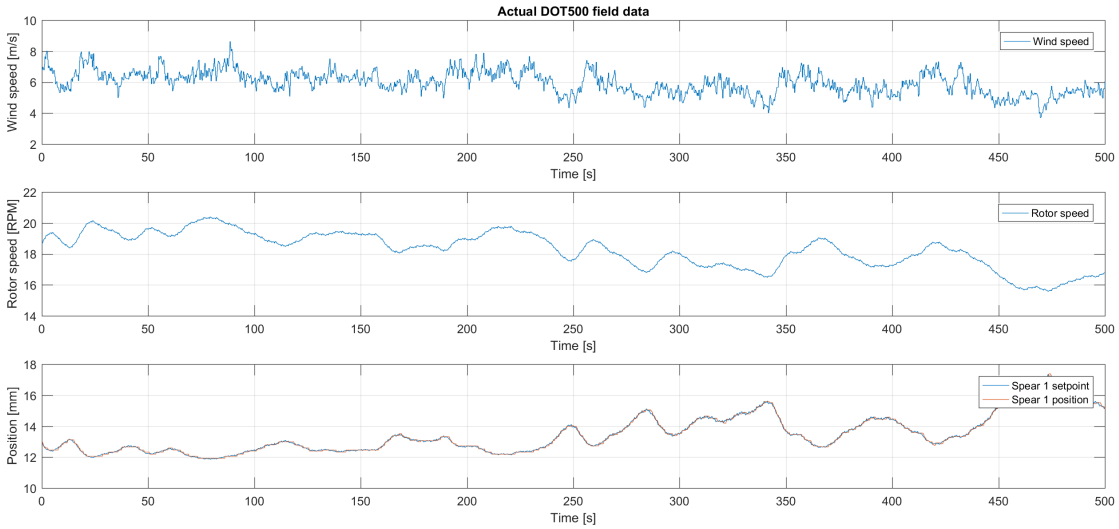

Figure 5-19: Field data of the DOT500, for comparison with hardware-in-the-loop configuration.

A normalized version of the wind speed and rotor speed is given in Figure 5-20, with *left* the large rotor model case and *right* the actual field data. From Figure 5-20 it is appears that the mass moment of inertia in this rotor model test is smaller than the actual inertia. This is in line with the calculations made in Section 5-2, where the inertia estimate was found to be five times higher than the nominal one used in the tests depicted in Figure 5-17. This new inertia estimate is taken into account in the pitch actuator-in-the-loop, described in Section 5-4.

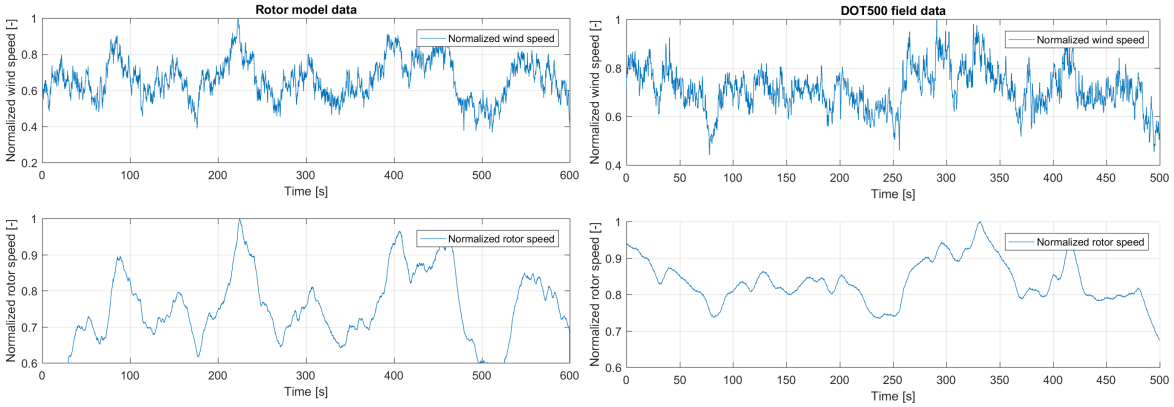

Figure 5-20: Comparison between normalized rotor model (*left*) and the smoother field data (*right*) indicates that the inertia used in the rotor model was lower than actual DOT500 inertia.

Finally, it is observed in the lower plot of Figure 5-19, that the actual DOT500 rotor mass moment of inertia is large enough to allow the spear valves to track their setpoints. Hence, it is possible to use active spear valve control in the below-rated region.

5-3-3 Emergency stop simulations

The most important feature of wind turbine control is the ability to stop the rotor at all times. Since new control algorithms are written and tested on the DOT500, emergency stopping scenarios are included in the design phase. First a pitch emergency stop is simulated on the power transmission system. In addition, since their was no prior experience with the pitch mechanism, an alternative spear valve method is discussed as back-up option.

Pitch emergency stop

As common in industry, emergency shutdown of the DOT500 turbine is achieved by pitching away the blades into their vane position. In the next test series, pitching away to vane is simulated by lowering the wind speed instantaneously to 0 m/s after 25 s. This simplified model does not take blade stall effects into account, which results in a longer stopping time then expected during actual field operation. The results are depicted in Figure 5-21, where a distinction is made between simultaneously opening (*red*), closing (*blue*) and leaving the spear valves untouched (*green*).

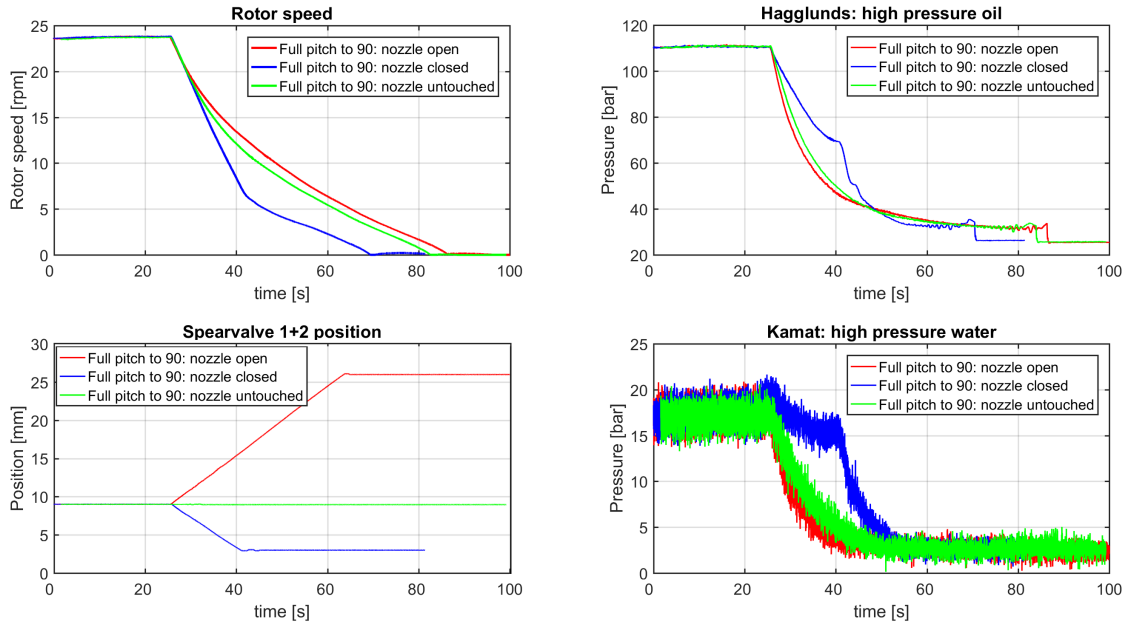

Figure 5-21: System response of instantaneously lowering the wind speed to 0 m/s, while simultaneously opening (*red*), closing (*blue*) and leaving the spear valve positions untouched (*green*)

From Figure 5-21 it is observed that leaving the spear valve positions untouched while lowering the wind speed to 0 m/s, results in a stopping time of 58 s; opening the spear valves results in a near similar response and stopping time of 61 s. In both cases the system torque is already close near its minimum.

In contrast, active closing of the spear valves results in a faster slowdown of the system, with a stopping time of 43 s. The higher pressure build-up in the system results in a higher system torque and therefore faster slowdown. More details on the effects of spear valve controlled system slowdown is given in the following test.

Spear valve emergency stop

Due to a lack of experience with the implemented pitch controlled stop, a back-up emergency stop which closes the spear valves in the water circuit is considered. The spear valve setpoint is after 15 s instantly decreased to 1 mm and 2 mm, respectively, in two distinct experiments on the power transmission system. The results are depicted in Figure 5-22.

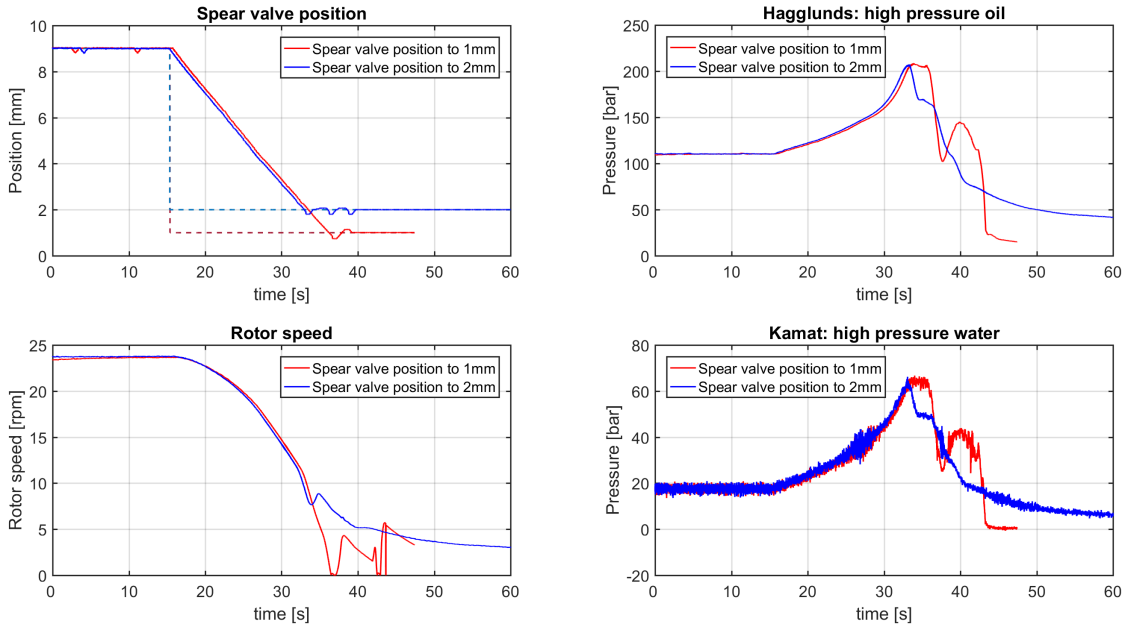

Figure 5-22: System response to an emergency stop enforced by decreasing the spear valve settings: setpoint decreased to 1 mm (*red*), setpoint to 2 mm (*blue*)

From Figure 5-22 it is again observed that the spear valves are limited by their positioning speed of 2.4 s/mm. Moreover, after the spear valves reach their new setpoint, an overshoot occurs followed by ringing. This spear valve ringing results in large pressure fluctuations in both the high-pressure oil and water line, since in this region small position changes have a large effect on the effective nozzle area, and thus system pressure (see Figure 5-4).

The spear valve ringing is found to be related to the fluctuations in rotor speed. In the 2 mm case (*blue*), this leads to 3 saddle points that are also observed in the high-pressure lines. Thereafter the rotor speed stabilizes to a new steady state around 3 RPM. However, in the 1 mm case (*red*), the initial spear valve position overshoot resulted in a complete standstill of the system at approximately 37 s. The spear valve ringing subsequently causes unwanted start-up acceleration and deceleration.

A solution to the ringing problem was given in Section 5-1-3, however these tests were performed before implementation of this deadband solution. Nevertheless, from the tests discussed in this section it is concluded that decreasing rotor speed by lowering spear valve setpoints up to standstill is possible, but full spear valve closure tests require more research considering safety and wear of the system. Until then the spear valve emergency stop is considered too risky, and a more suitable alternative is developed which chokes the high-pressure oil line. This method was described earlier in Section 4-6-3 and was used in Section 5-2, where field data of this emergency stop was used to derive the rotor mass moment of inertia.

5-4 Preliminary validation of pitch control

In this section a slightly modified version of the rotor model from the previous section is used, in order to test the pitch controller implementation on the actual pitch cylinder and rotor of the DOT500. The main purpose of the tests described in this section is to verify the implementation of the pitch controller at rotor standstill, as a last check before the controller is tested in above-rated wind conditions. In this way, bugs and errors were quickly identified and fixed, without taking the risk of damaging the turbine by unexpected behaviour.

During the pitch actuator tests, the rotor position is locked using the rotor parking brake. Hence, instead of using the actual rotor speed and assumed fine-pitch angle, the rotor torque is now based on the calculated rotor speed and actual measured pitch angle. A schematic representation of the implementation is presented in Figure 5-23, and is given in a series of relations below.

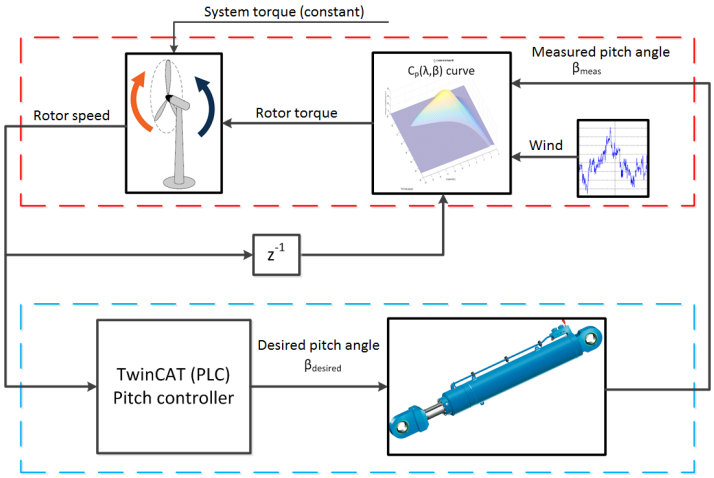

Figure 5-23: Hardware-in-the-loop implementation scheme. The red box contains all software components, including Newton's second law for rotation, power coefficient evaluation, and wind speed input. The blue box includes all hardware components interacting with the simulation software, such as the PLC and pitch actuator.

Since the rotor is locked, there is no pressure build-up in the system. However, because the pitch controller is only active in the above-rated region, the system torque is now taken as a constant input to the model

$$\tau_{\text{system}} = \frac{P_{\text{rated}}}{\omega_{\text{rated}}}, \tag{5-12}$$

where P_{rated} and ω_{rated} are the rated rotor power and rotational speed, which are taken as 500 kW and 28 RPM, respectively. The rotor torque induced by a wind signal is evaluated by

$$\tau_{\text{aero}}[k] = \frac{1}{2}\rho_{\text{air}} V^2[k] \pi R^3 \frac{C_{\text{p}}\left(\lambda[k], \beta[k]\right)}{\lambda[k]}, \tag{5-13}$$

where k represents the index value of the fixed time step simulation, ρ_{air} the air density, V the rotor effective wind speed, R the rotor radius, and λ the current tip-speed ratio. The

power coefficient C_p is again evaluated for each interval using a power curve obtained from the scaled wind turbine model, but is now a function of both the tip-speed ratio λ and the actual measured blade pitch angle β.

Finally, using Equation 5-12 and 5-13, the following discretized version of Newton's second law for rotation is used for calculation of the new simulated rotor speed

$$\omega[k+1] = J^{-1} \left(\tau_{\text{aero}}[k] - \tau_{\text{system}}\right) \Delta t + \omega[k], \tag{5-14}$$

where J is the combined rotor mass moment of inertia estimate of the rotor and low-speed shaft, taken $6.6 \cdot 10^5\,\text{kgm}^2$ as derived in Section 5-2. The main difference with Equation 5-11 is that now the system torque is considered as a constant. The rotor speed setpoint is sent to the PLC, using the ModBUS communication protocol [88], from where the pitch cylinder is actuated.

5-4-1 Blade pitch step response at standstill

This test incorporates a stair-case wind signal to evaluate the transient response of the closed-loop system. The stair-case wind signal (displayed in *red*) ranges from 15 to 24 m/s with steps of 1 m/s and time intervals of 50 s, and results are presented in Figure 5-24.

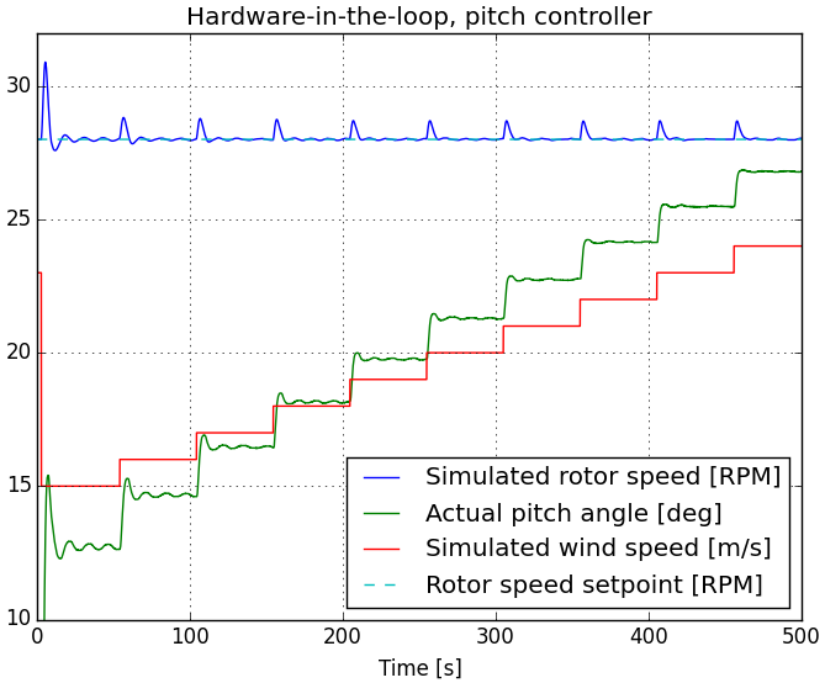

Figure 5-24: Response to step changes in the wind from 15 to 24 m/s

After an initial overshoot, caused by the initialization of the hardware-in-the-loop simulation, it is observed that the rotor speed is actively controlled to the reference rotor speed setpoint of 28 RPM. The rotor speed transient after each step in wind speed shows similar characteristics (*blue*), which is a result from the gain-scheduled PI-controller at different operating conditions, as described in Section 4-4. The corresponding measured pitch angle is displayed in *green*.

5-4-2 Pitch actuator hardware-in-the-loop with rotor model simulations

In this final preliminary test, the rotor model is used in combination with a turbulent wind signal to evaluate real-world performance of the controller. The turbulent wind signal ranges from 16 to 24 m/s with a duration of 500 s, and results are depicted in Figure 5-25.

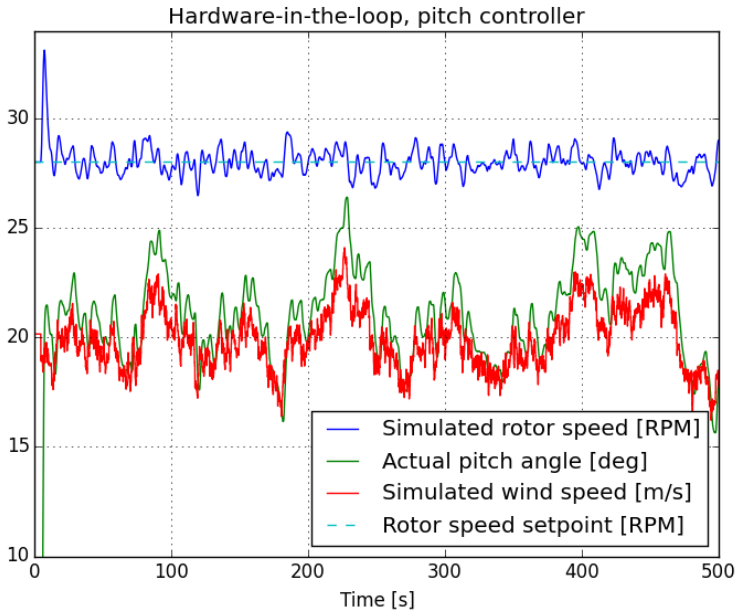

Figure 5-25: Hardware-in-the-loop for evaluation of the pitch control implementation, simulating rotor speed and actuating the pitch cylinder

It is observed that the pitch controller is able to stabilize the wind turbine in this realistic turbulent wind field, with a maximum overshoot of approximately 1 RPM. It should be noted that the wind signal average was actually taken too high, resulting in wind speeds above the turbine cut-out speed of 20 m/s. However, this test demonstrated the functioning of the pitch controller design, and the controller was sufficiently trusted for subsequent tests with a rotating rotor.

Chapter 6

Experimental validation of individual and integrated controllers

The objective of this chapter is to validate the control strategy that was designed in Chapter 4. First, in Section 6-1, validation of the individual controllers is performed. Field recorded data of the DOT500 is used to check controller performance. Then, in Section 6-2, nominal performance of the DOT500 with integrated control is evaluated.

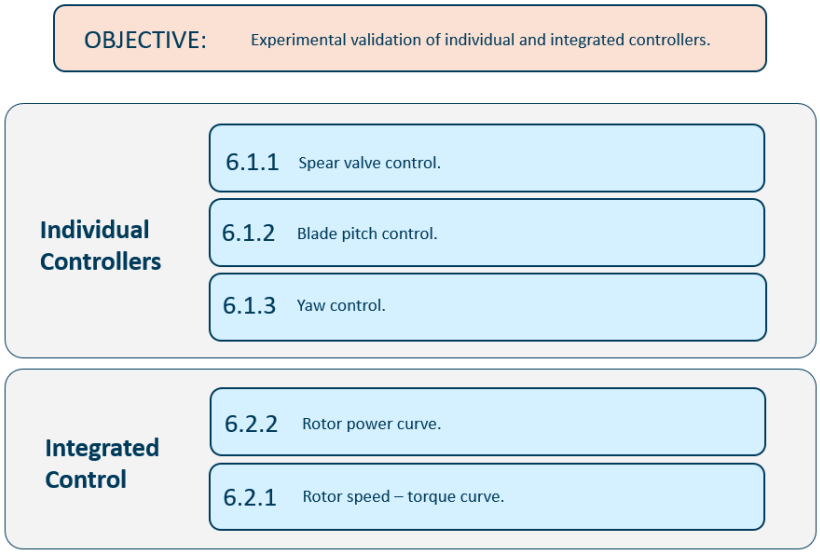

Figure 6-1: Chapter outline

6-1 Validation of individual controllers

This section evaluates the individual controllers during field operation. First, in Section 6-1-1, field recorded data related to the spear valve torque controller is introduced. The same is done for the blade pitch and yaw controllers in Section 6-1-2 and 6-1-3, respectively.

6-1-1 Spear valve control

In Figure 6-2a, one hour of active spear valve control is presented. The upper plot shows the wind speed measurement, the middle plot the measured rotor speed. In the lower plot, both the spear valve setpoint and position are presented. Data is recorded during a single test, the two data gaps around 1200 and 2400 s are due to the start of a new log file. A zoomed-in version, to show the spear valve tracking capability, is given in Figure 6-2b.

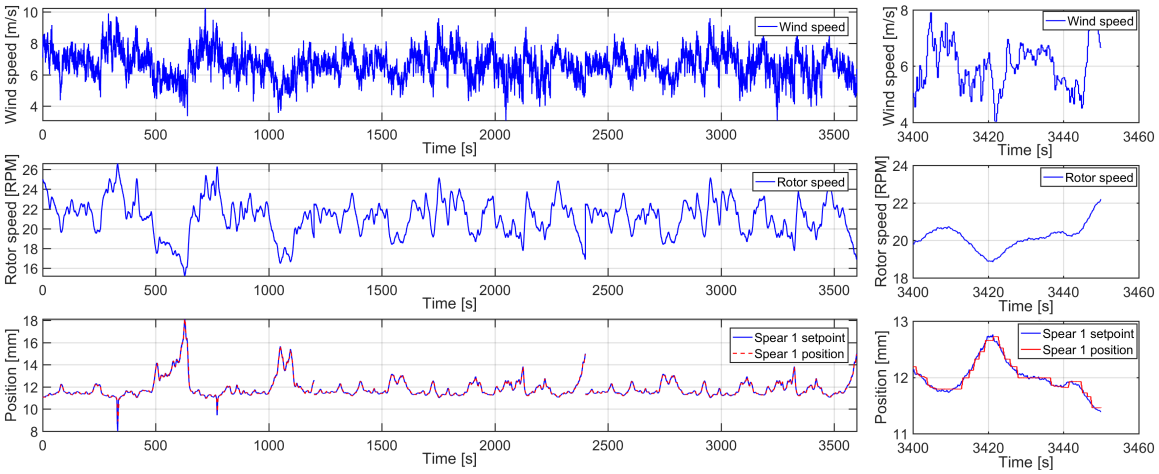

(a) One hour of field recorded data of the DOT500. **(b)** Zoomed-in version.

Figure 6-2: Spear valve movement during below-rated operation.

The average wind speed is 6.3 m/s and the goal in this below-rated region is to achieve the maximum power coefficient $C_{\mathrm{p,max}}$, which corresponds to a theoretical tip-speed ratio of 7.55 at fine-pitch. Figure 6-3 presents the actual tip-speed ratio during the experiment. During this hour of operation, an average tip-speed ratio of 7.43 is obtained, which is 1.6 % below the theoretical optimum. The high peaks in Figure 6-3 are caused by wind drops below the cut-in wind speed of 4.6 m/s (see Figure 6-2a), which is too low for operation at $C_{\mathrm{p,max}}$.

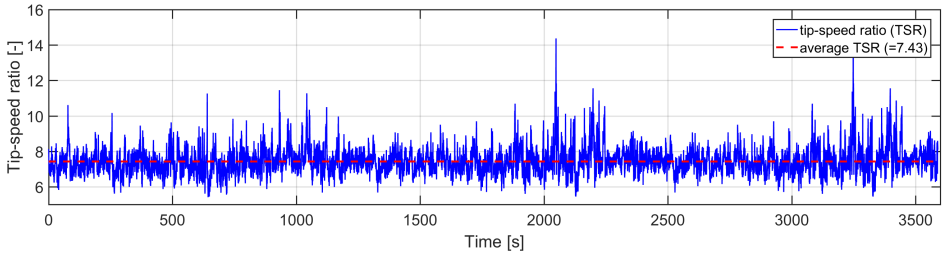

Figure 6-3: Tip-speed ratio (TSR) during one hour of operation.

Determination of spear valve position in above-rated region

This section aims to determine the spear valve setpoint in the above-rated region, from DOT500 field recorded data. In this region rotor speed is regulated and kept constant by blade pitch control only, and a fixed spear valve position is used to attain the torque required for rated power. As stated in Section 5-1-2, identification of the indoor power transmission system was not possible around the rated operating region, due to both torque limitations of the electro-motor and the pressure relieve valve, and therefore field recorded data of the DOT500 is used to update this parameter setting. Figure 6-4 presents the rated rotor power output, measured at different spear valve setpoints.

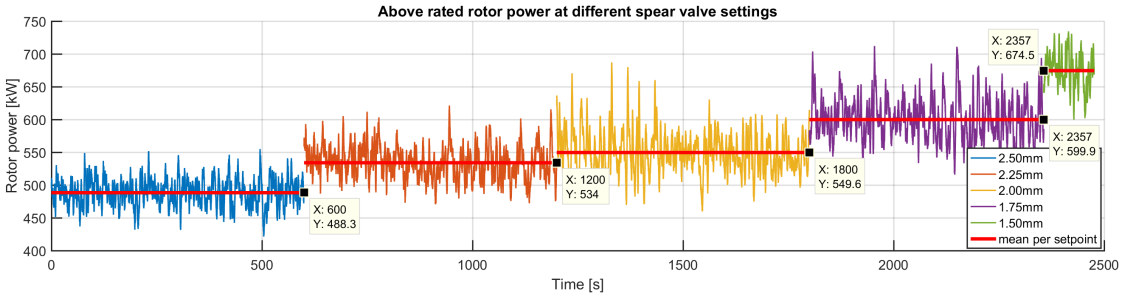

Figure 6-4: Experimental relation between spear valve position and rated rotor power. A spear valve setpoint of 1.75 mm results in the desired average rotor power of 600 kW for the DOT500.

From Figure 6-4 it is derived that a spear valve setpoint of 1.75 mm results in the desired average rotor power of 600 kW. The duration of the 1.50 mm test is shorter than the others, since the measured average 675 kW was probably outside the design limits of the V44 turbine and therefore considered unsafe to proceed for a longer period of time.

Figure 6-5 displays a zoomed-in version of Figure 5-5 from Section 5-1-1, and shows a near linear relation between the spear valve needle position and nozzle area in the region of interest. Furthermore, the nozzle area A_{nozzle} is supposed to have an inversely quadratic relation to the high water pressure drop Δp according to the following relation [1]

$$\Delta p = \frac{\rho_{\text{water}}}{2} \cdot \left(\frac{1}{C_{\text{d}} \cdot A_{\text{nozzle}}} \right)^2 \cdot Q \cdot |Q|, \tag{6-1}$$

where ρ_{water} is the water density, Q the volumetric flow and C_{d} the discharge coefficient which considers pressure losses depending on geometry and Reynolds number. The resulting high water pressure is linearly proportional to the system torque and, since the turbine operates at a constant rotational speed in the above-rated region, to the rotor power.

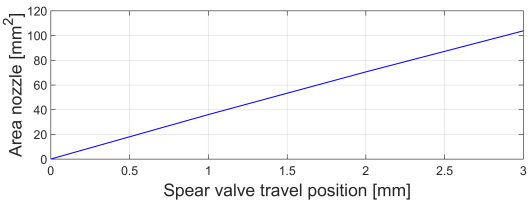

Figure 6-5: Relation between spear valve position and nozzle area.

However, this trend between spear valve position and power is not clear from Figure 6-4, in particular not around the 2.25 mm setpoint. The reason for this deviation is found in the second spear valve position, of which the position did not settle exact at the required setpoint. This is shown in Figure 6-6. The offset between position and setpoint matches with the non-proportionality in Figure 6-4 and also shows the sensitivity to spear valve changes in this rated region.

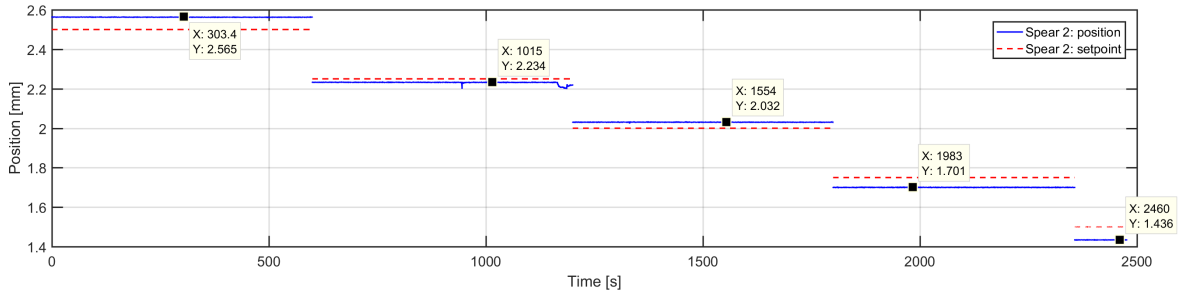

Figure 6-6: Difference between second spear valve setpoint and position

The use of spear valves to regulate fluid pressure to vary the system torque, as opposed to the industry standard generator torque control, is not seen in any other of the existing hydraulic wind turbine concepts discussed in Chapter 2. The results in this section show that spear valve control is a feasible solution in both below- and above-rated regions.

6-1-2 Blade pitch control

The blade pitch controller performance is presented in Figure 6-7. The upper plot shows the wind speed measurement, the middle plot the measured rotor speed. In the lower plot, both the blade pitch setpoint and position are depicted. Data is recorded during a single test with a duration of 10 minutes.

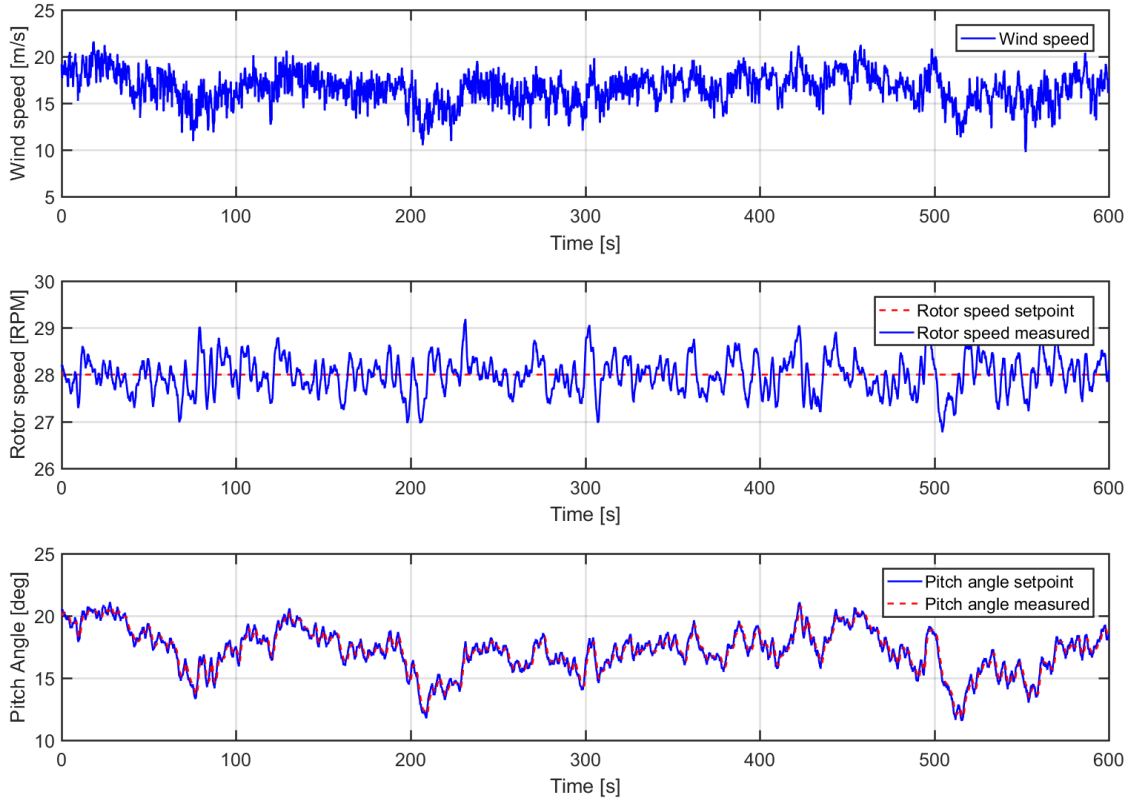

Figure 6-7: Blade pitch control operation in the above-rated wind speed region, with the control objective to maintain a rotor speed of 28 RPM. Ten minutes field recorded data of the DOT500.

During this test an average wind speed of 16.6 m/s was present, which is well in the above-rated wind speed region. Note that the wind speed exceeds the cut-out wind speed of 20 m/s several times, but just not long enough to pass the designed 30 s threshold that would trigger the CodeOrange stopping procedure described in Section 4-6-3.

It is observed in the middle plot of Figure 6-7 that the blade pitch controller keeps the DOT500 rotor speed at 28 RPM within 1 RPM overshoot during these rough wind conditions. This is in line with the preliminary pitch actuator-in-the-loop simulations described in Section 5-4 and the control objective stated in Section 4-4. The combination of a fixed spear valve setpoint and the use of active blade pitch control, to maintain rated torque and speed respectively, leads to the desired rated power output in the above-rated region.

6-1-3 Yaw control

When the turbine is turned on after some offline time, the nacelle often has an initial misalignment with the dominating wind direction. In Figure 6-8 the yaw controller was enabled, while the nacelle position had a 80 deg offset to the wind direction. Due to this large offset, the accumulated error threshold is passed almost instantaneously and starts yawing counter clockwise. The overshoot is counteracted by a clockwise yaw motion. After 314 seconds the nacelle is aligned and no further yaw control actions are required.

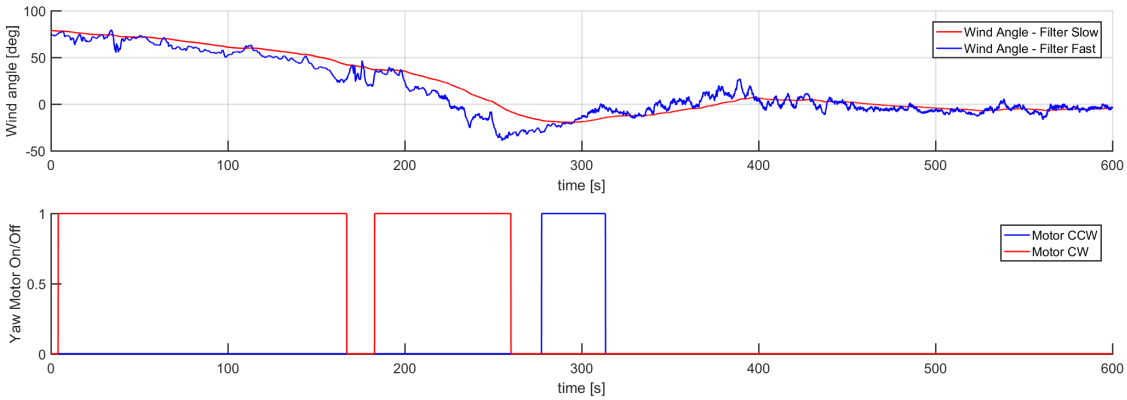

Figure 6-8: Yaw start-up: from 80 deg offset to nacelle alignment with dominant wind direction.

After the startup procedure has completed, the goal of the yaw controller is to keep the nacelle aligned in the wind. An example of the steady state performance of the yaw controller is depicted in Figure 6-9. The effect of the quadratic term in the accumulated error, described in Section 4-5, is observed around 346 seconds. The offset in the fast filtered wind signal, visible in the upper plot, results in brief motor action. Lowering the accumulated error threshold would result in smaller deviations around aligned position. However, this would also imply more motor activation and the risk of overreacting to instantaneous wind direction changes.

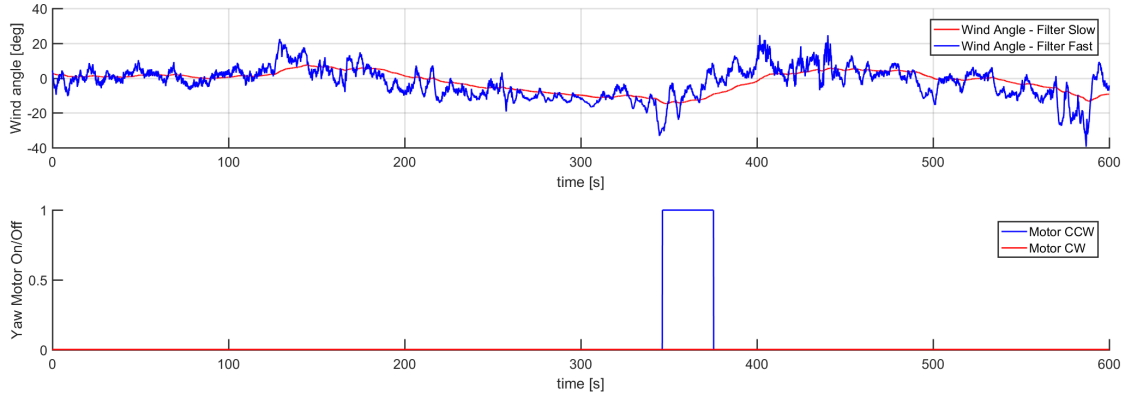

Figure 6-9: Effect of quadratic term in the accumulated error threshold. The high offset in the fast filtered wind signal around 346 s results in an immediate yaw correction.

Finally, in Figure 6-10, the yaw controller is evaluated for a full hour. It is observed that the yaw controller keeps the nacelle aligned around zero with no offset, the slow filtered signal stays within 10deg amplitude and only 4 moderate motor actions are required.

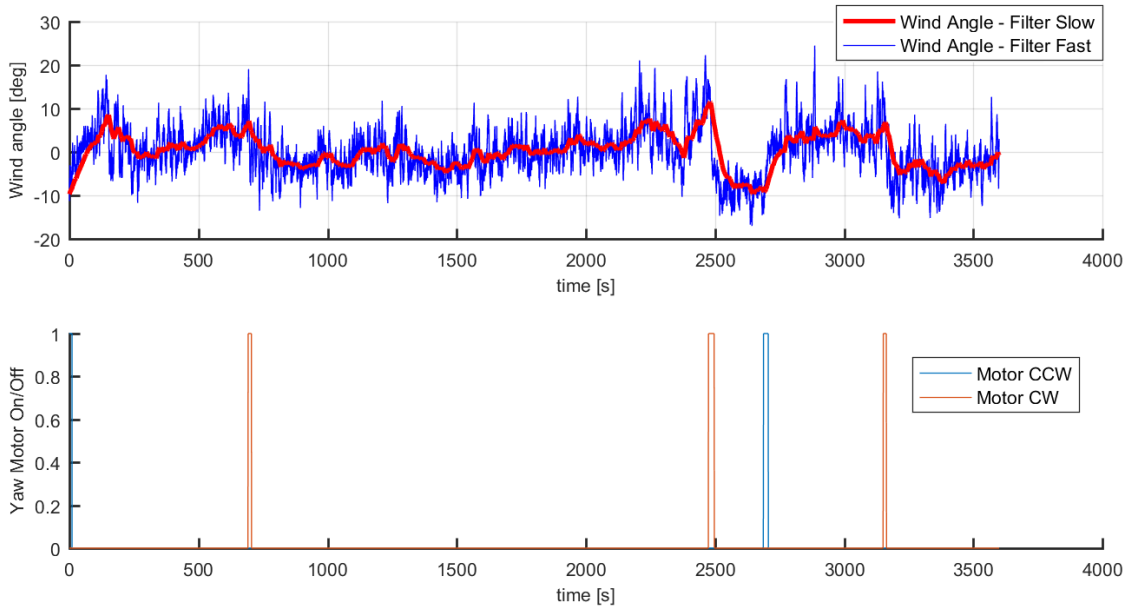

Figure 6-10: Yaw action during one hour of operation of the DOT500. The controller keeps the slow filtered wind angle within 10 deg misalignment. Four brief yaw corrections are required.

6-2 Integrated controller performance during normal operation

In this section, the integrated control strategy for the DOT500 turbine is validated. The field derived rotor power curve is presented in Section 6-2-1. Next, in Section 6-2-2, the rotor speed - torque curve is outlined.

6-2-1 Experimental rotor power curve

The experimentally derived rotor power curve of the DOT500 is presented in Figure 6-11. The *grey* dots represent field recorded data points, which are binned per 0.5 m/s wind speed in the *blue* line. The obtained rotor power curve is compared to the power curve originating from the Vestas V44 data sheet (Appendix A), which is represented by the *red* line. Furthermore, the *green* line shows the theoretical maximum attainable curve, derived from the designed maximum power coefficient $C_{\mathrm{p,max}}$ and the ideal tip-speed ratio of the Vestas V44 rotor, up to the maximum allowable rotor power of 600 kW.

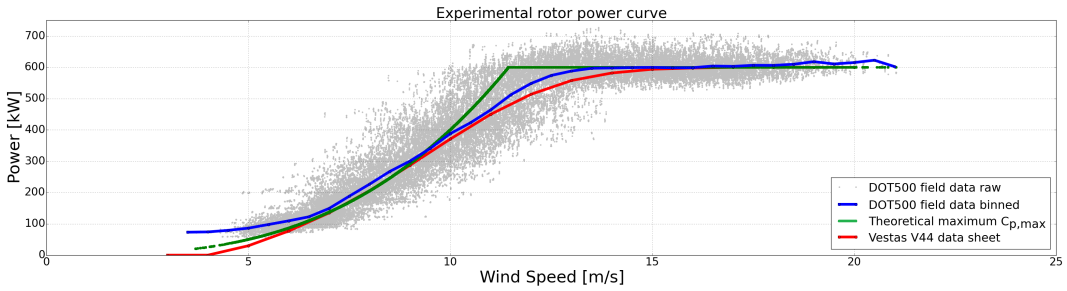

Figure 6-11: Experimentally derived rotor power curve of the DOT500 turbine. The *grey* dots represent field recorded data, binned per 0.5 m/s wind speed in the *blue* line. Results are compared to the Vestas V44 data sheet (*red*) and theoretical maximum power at $C_{\mathrm{p,max}}$ (*green*).

The DOT500 is able to start from a cut-in wind speed of around 4.5 m/s. Furthermore, the turbine operates with active spear valve control near $C_{\mathrm{p,max}}$ up to a wind speed of approximately 9 m/s. This wind speed corresponds to control point C, whereafter the turbine deviates from the $C_{\mathrm{p,max}}$-curve and is ramped up to rated power. A C_{p}-curve at a fixed 0 deg fine-pitch angle is also experimentally derived and presented in Figure 6-12.

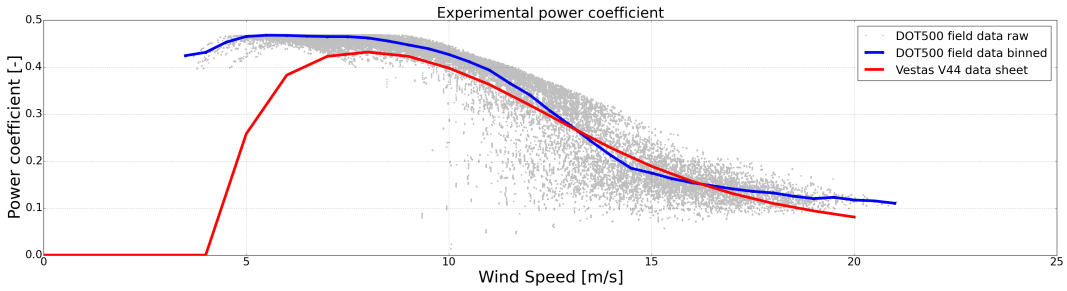

Figure 6-12: Experimentally derived power coefficient of the DOT500 turbine (raw in *grey* and binned per 0.5 m/s in *blue*). Results are compared to the original Vestas V44 data sheet (*red*).

The C_p of every measurement (*grey*) in Figure 6-12 is calculated with the $C_p(\lambda, \beta)$-relation from a scaled V66 model, using field measurements of the rotor speed, wind speed and pitch angle. The same is done for the *blue* line, but in this case the data points are binned per 0.5 m/s wind speed. Finally, in *red*, the curve obtained from the Vestas V44 data sheet.

As the experimental power coefficient is based on the theoretic $C_p(\lambda, \beta)$-relation, it is merely meant to indicate the trend line. Note e.g. the below-rated operation at constant C_p, the deviation from this C_p at 9 m/s and the clear transition point between below- and above-rated operation around a wind speed of 14 m/s, caused by the decoupled control strategy.

In a similar manner the thrust coefficient is obtained, and is presented in Figure 6-13. The exclusion of thrust force reduction in the control objective is noticeable in the control transition region in Figure 6-11; as it results in a power curve that differs from the Vestas V44 curve and is closer to the theoretical maximum. This outcome is also found in the experimentally derived thrust force in Figure 6-14, which indicates a 10 % higher maximum thrust force in this area. The possible unfavourable consequences of this result, however, remain open for further research.

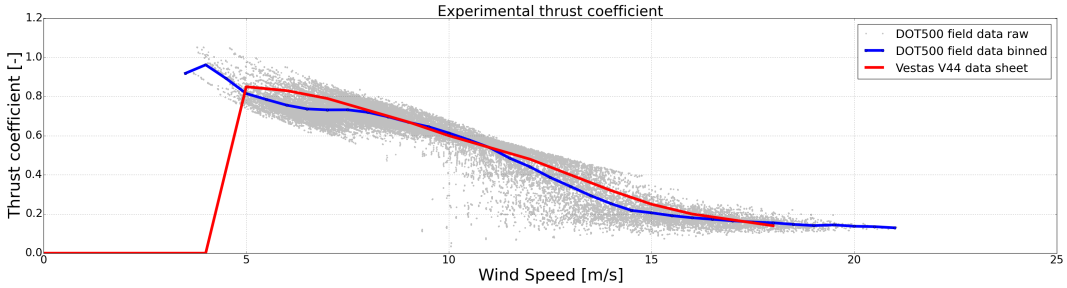

Figure 6-13: Experimentally derived thrust coefficient of the DOT500 turbine (raw in *grey* and binned per 0.5 m/s in *blue*). Results are compared to the original Vestas V44 data sheet (*red*).

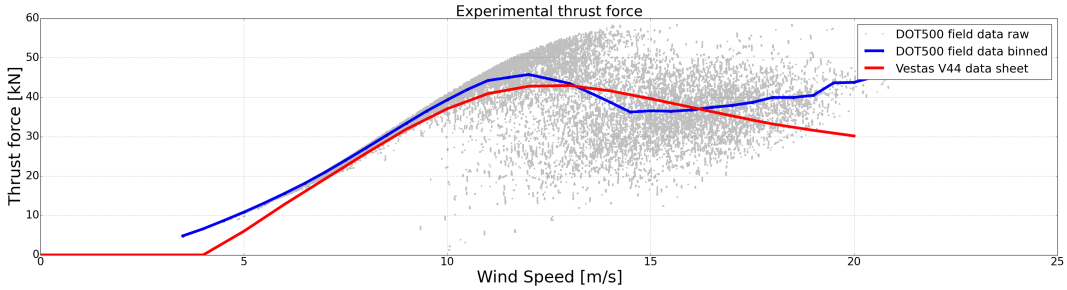

Figure 6-14: Experimentally derived thrust force of the DOT500 turbine (raw in *grey* and binned per 0.5 m/s in *blue*). Results are compared to the original Vestas V44 data sheet (*red*).

With the current control strategy, the DOT500 reaches its nominal power output at a rated wind speed of 14 m/s. Between rated and cut-out wind speed the turbine is kept at rated power by a fixed spear valve setpoint and active blade pitch control. Supervisory control, described in Section 4-6, takes operation restrictions such as rated speed and cut-out wind speed into account. The developed software design includes starting and (emergency) stopping procedures.

6-2-2 Rotor speed - torque curve

Figure 6-15 shows in *grey* DOT500 field data projected on the rotor speed - torque plane. The *blue* line displays a binned version, where the raw data is collected in bins of 0.5 RPM. In *red* the region 2 control law is depicted, derived from the maximum power coefficient $C_{\mathrm{p,max}}$ and the ideal tip-speed ratio of the Vestas V44 turbine rotor (as was given by Equation 4-6).

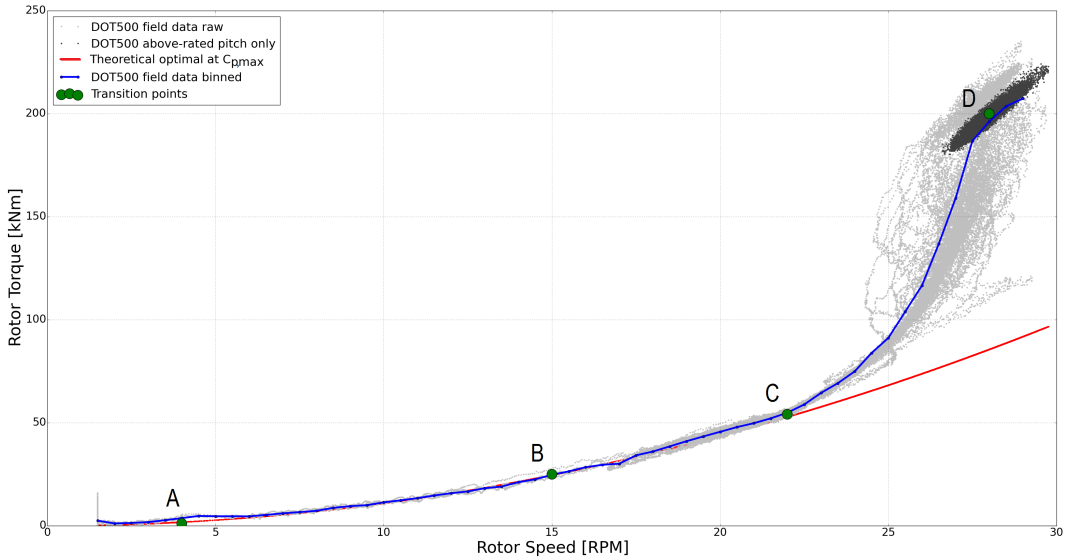

Figure 6-15: Experimental torque - speed curve of the DOT500 turbine.

In the start-up procedure, where the blades are pitched toward their fine-pitch angle, the rotor accelerates as shown in the lower left of Figure 6-15. Since the turbine requires a minimum cut-in wind speed of 4.5 m/s, the rotor accelerates immediately to point B at 15 RPM to obtain the optimal tip-speed ratio of 7.55. Performance data is therefore mainly available from this rotor speed and higher. Between the transition points B and C, the turbine operates along the region 2 control law (described in Section 4-3-2).

After point C, which corresponds to 22 RPM at the rotor, the spear travel setpoint is linearly ramped up to achieve rated power. This leads to the quadratic torque increase between the points C and D in Figure 6-15, as the system pressure varies quadratically with the effective nozzle area according to Equation 6-1. Finally, at above-rated wind speeds, the objective becomes to maintain rated power. Data from three above-rated experiments is visualized in *dark grey* in Figure 6-15, to indicate decoupled pitch controller operation.

A higher rotational speed at point C would lead the turbine longer along the *red* optimal torque line, but then the linear travel slope becomes too steep for the spear actuators to follow. This effect becomes visible in the increased spread of data points between the transition points C and D. Performance in this region could be improved by using faster spear valves, or a Multi-Input Multi-Output (MIMO) control strategy that includes a saturation overlap of the two controllers. The latter requires identification of the actual turbine in a stable configuration, for which the current strategy is suitable.

Furthermore, the current Vestas V44 rotor is not designed to match the hydraulic drive train optimal efficiency envelope that is used in the DOT500 turbine. Performance tests, that were performed outside the scope of this thesis, indicate that operating at a far lower tip-speed ratio could result in a higher overall turbine efficiency in the below-rated region. Operation at this lower tip-speed ratio results in reduced flows at higher system pressures, which increases the pressure sensitivity to small spear valve positions. This results in a higher torque requirement at every below-rated rotor speed, and hence a more gentle transition between the points C and D in Figure 6-15. This result, however, is highly correlated to the partial load efficiencies of the individual drive train components and requires further research.

The current decoupled strategy, however, does prove that maximum power coefficient control is achieved in the below-rated region with the current spear valve actuators. Furthermore, it stabilizes the DOT500 system above-rated and functions as a baseline control strategy for further research at DOT.

Chapter 7

Tuning of DOT500 with Extremum Seeking Control

This chapter outlines the data-driven performance optimization routines that are performed on the DOT500 with Extremum Seeking Control, in order to optimize several of its control parameters. This is first performed on the turbine's fine-pitch angle in Section 7-1. In Section 7-2 this method is used for optimization of the generator speed feedforward control law. Finally, in Section 7-3, future parameters that could be relevant to update with data-driven techniques are discussed.

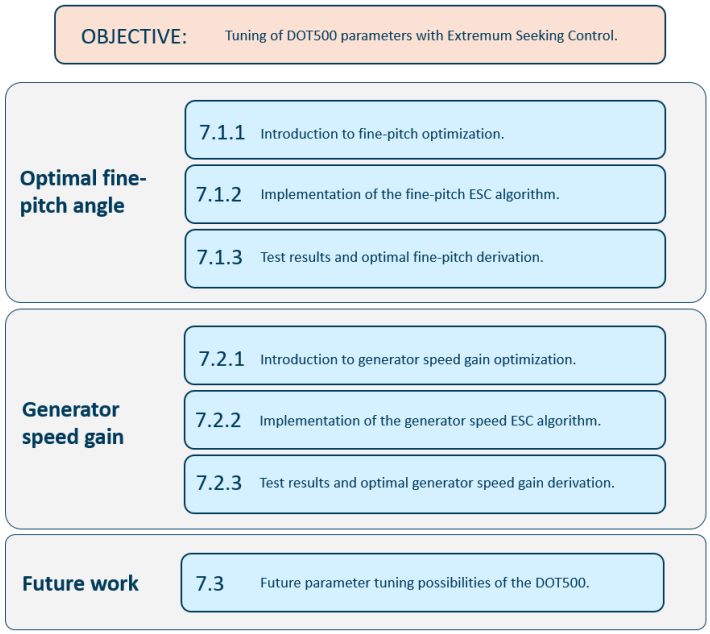

Figure 7-1: Chapter outline

7-1 Optimal blade fine-pitch angle

This section starts with a brief introduction to fine-pitch optimization. Then the Extremum Seeking Control (ESC) algorithm implementation is outlined. Finally, test results are given and a conclusion on the optimal fine-pitch angle is derived.

7-1-1 Introduction to fine-pitch optimization

As stated several times in this thesis, exact information on the Vestas V44 blade geometry and thus aerodynamic rotor characteristics of the turbine were unavailable during the controller design process. Hence, as a consequence, the fine-pitch angle used for maximum power extraction in the below-rated region was assumed to be equal to 0 deg. However, operating at a non-optimal fine-pitch angle results in reduced rotor power capture and therefore the aim of this section is to find the pitch angle for maximum power extraction.

Figure 7-2 shows the difficulty to distinguish the effect of the fine-pitch angle from wind fluctuations in the measured rotor power. In this test the fine-pitch angle was varied over a stair-case input signal and the effect on the rotor performance was measured, but this effect seems more related to the poor Signal-to-Noise Ratio (SNR) caused by large wind fluctuations.

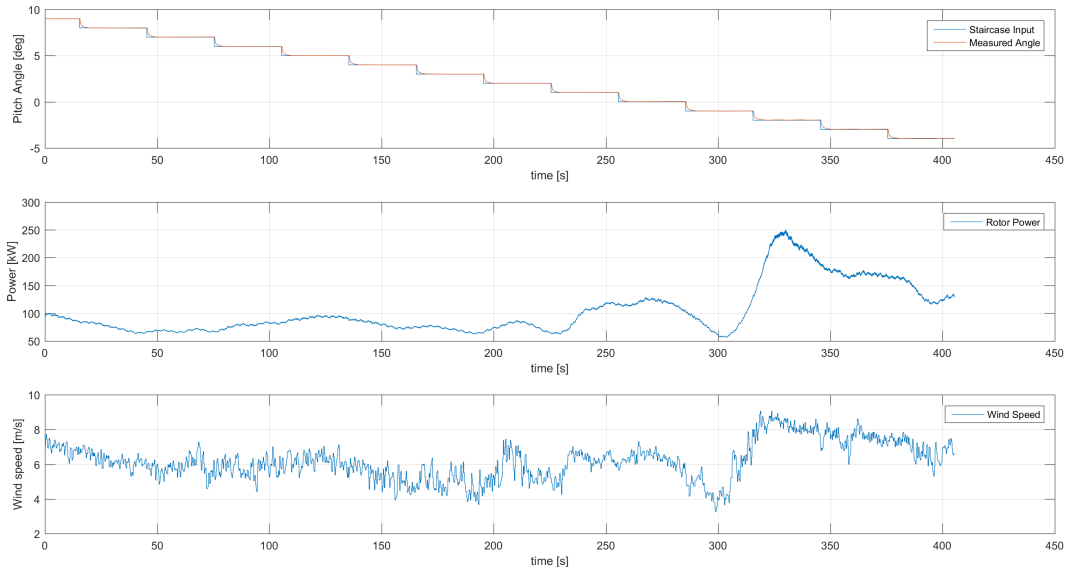

Figure 7-2: The top plot shows a stair-case on the fine-pitch angle during below-rated operation. The corresponding rotor power measurements are given in the middle plot, and below the wind speed measurement is depicted. Note the increase in power after 300 s which is most likely an effect of the sudden large wind fluctuation.

Therefore, Extremum Seeking Control (ESC) is employed on the fine-pitch angle during field tests, to find the pitch angle for maximum rotor power extraction in the below-rated region. Extremum Seeking Control is a control algorithm that searches online the input signal for optimization of a predefined cost function, without the need for a system model. The theoretic framework is adapted from Xiao et al. in [63], for the derivation of the mathematical framework of the ESC algorithm the reader is referred to [70]. A general description of the method is also included in Section 3-2-3.

7-1-2 Implementation of the fine-pitch ESC algorithm

In the implementation described in this section, ESC optimizes the DOT500 effective rotor power $P_{\text{rotor}} = f(\beta)$ as a function of the blade pitch angle β. The rotor power is obtained using load pins, located in the suspension of the pump connected to the rotor, measuring the effective rotor torque. The algorithm is based on a dither-demodulation scheme, by periodic excitation at a single frequency on a turbine input: in this case the pitch angle β in the below-rated region of operation. It optimizes the power signal by finding the input β that results in a gradient $\partial P/\partial\beta$ that goes to zero. A schematic overview of the implementation is given in Figure 7-3, of which the theoretical framework was given in Section 3-2-3.

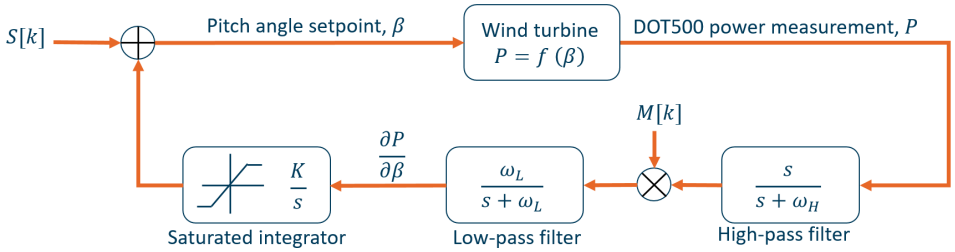

Figure 7-3: Schematic overview of the ESC implementation for maximizing the rotor power P, with the blade pitch angle β as the decision variable. An integrator saturation is included, preventing infeasible pitch actuator setpoints.

For tuning parameters needed by the ESC scheme, the design guidelines as described in [63] are used. The optimization scheme is excited by the sinusoidal dither and demodulation signals $S[k]$ and $M[k]$, for which both the dither frequencies should be within the bandwidth of the system input-output dynamics, and the dither amplitude must provide a significant Signal-to-Noise Ratio (SNR) for the dithered output. To identify the dither frequency, the simulated open-loop step response tests from Section 5-4-1 are used. In these tests, transient characteristics of the rotor speed after a step change on the pitch angle showed a maximum time constant τ of 25 seconds, resulting in a dither frequency of 0.04 rad/s.

The low- and high-pass filter cut-off frequencies ω_{L} and ω_{H} should be chosen such that they sufficiently suppress and include dither related harmonics on the dither frequency, respectively. They are chosen as 0.0230 and 0.0205 rad/s, such that at the dither frequency the input signal is subjected to a gain of -6 and -1 dB, respectively. This is in correspondence with the derivation in Section 3-2-3 and shown in the Bode plot in Figure 7-4.

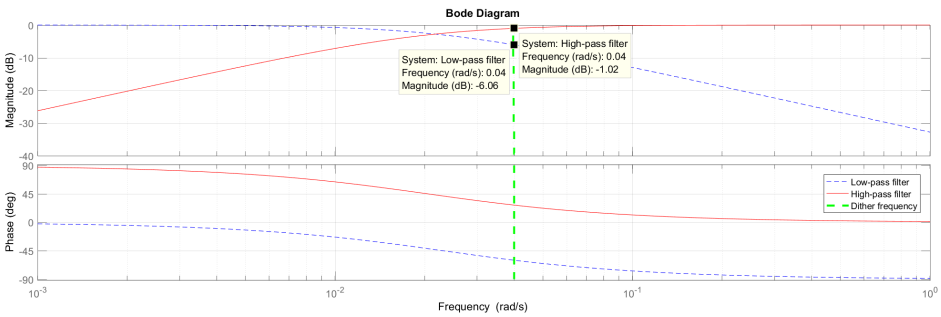

Figure 7-4: Bode plots of low-pass filter (blue), high-pass filter (red) and dither frequency (green)

After simulation of the ESC scheme on a high-fidelity wind turbine model under turbulent wind conditions, a dither amplitude of 2 deg is considered to have a significant SNR at the dither frequency, with respect to measurement noise and the external wind disturbances.

The integrator gain K determines the algorithm convergence rate, and is initially taken as $2 \cdot 10^{-4}$. In general a larger integrator gain results in a faster convergence speed, but a too large gain could destabilize the ESC optimization algorithm. In addition to the standard implementation, an integrator saturation on the lower bound (-5 deg) of the pitch angle is included. This saturation prevents the pitch setpoint to attain values that are infeasible for the pitch actuator. Finally, the phase shift between the signals $S[k]$ and $M[k]$, which compensates for the phase change in the ESC scheme, is chosen as 0.5 rad. The mentioned parameters are summarized in Table 7-1.

Parameter	Value
Dither amplitude	2 deg
Phase-offset	0.5 rad
Dither frequency	0.04 rad/s
Low-pass filter cut-off frequency	0.0230 rad/s
High-pass filter cut-off frequency	0.0205 rad/s
Integrator gain	$2 \cdot 10^{-4}$

Table 7-1: Tuning parameters of the ESC scheme for fine-pitch optimization

7-1-3 Test results and optimal fine-pitch derivation

Field recorded experiments are performed on the DOT500 turbine, according to the aforementioned implementation. Results of the first ESC fine-pitch optimization experiment are presented in Figure 7-5. The algorithm is started from the hitherto assumed fine-pitch angle of 0 deg and converges to -2.5 deg after 2000 s.

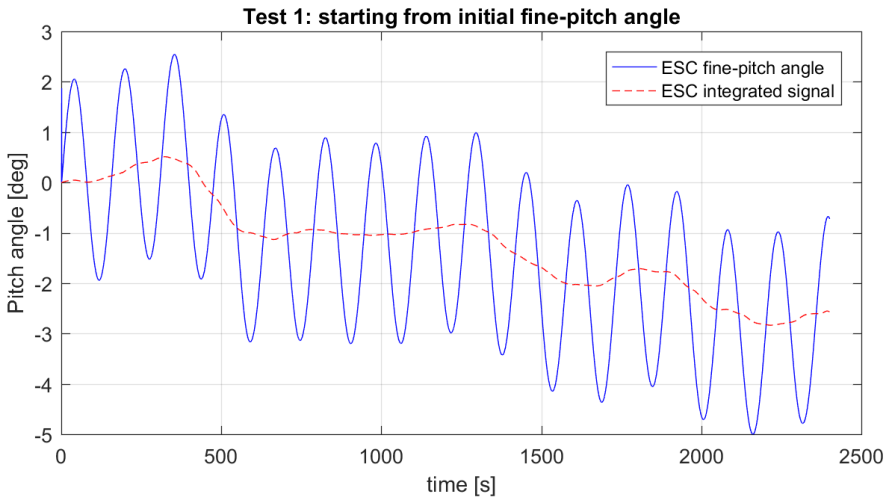

Figure 7-5: First ESC experiment to optimize the fine-pitch angle for below-rated operating conditions, starting from initial fine-pitch angle of 0 deg and converging to -2.5 deg after 2000 s.

In order to reduce the possibility that the derived result is a local minimum, a second experiment is performed from a large initial offset. This time, the algorithm is started form an initial pitch angle of 5 deg. Results of this experiment are presented in Figure 7-6. The algorithm quickly shows a downward trend and, as in the previous experiment, converges again towards a setpoint of -2.5 deg.

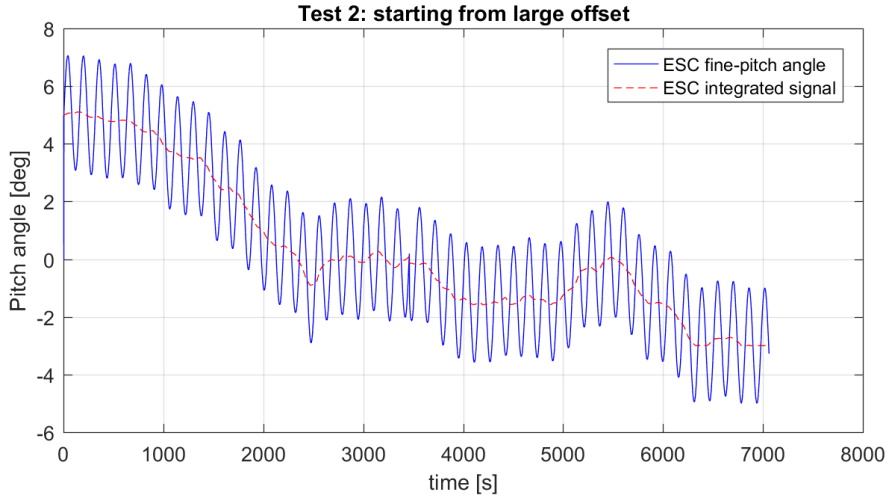

Figure 7-6: Second ESC experiment to optimize the fine-pitch angle for below-rated operating conditions, starting from initial fine-pitch angle of 5 deg to ensure global optimization.

Finally, a third experiment is started from the newly found fine-pitch angle. As observed in Figure 7-6, the previous experiment neared the integrator saturation lower bound of -5 deg. Therefore, a slightly smaller dither amplitude of 1.5 deg is chosen in this final experiment, of which the results are presented in Figure 7-7.

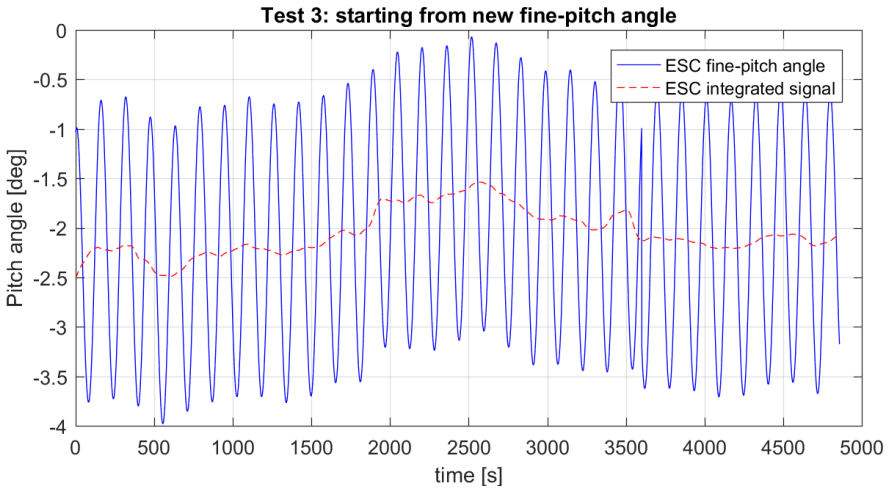

Figure 7-7: Third ESC experiment to optimize the fine-pitch angle for below-rated operating conditions, starting from the angle obtained from the previous two tests. This time a lower dither amplitude of 1.5 deg is used.

Figure 7-7 indicates that the ESC algorithm stabilizes around a fine-pitch angle of -2 deg. Therefore, this angle is considered the new fine-pitch angle of the DOT500 turbine.

Finally, the derived result is compared to the theoretical approximation based on the Vestas V66 C_p-curve. Figure 7-8 indicates that maximum power extraction indeed occurs at a fine-pitch angle between -2 and -2.5 deg. The derived fine-pitch angle should therefore result in a slightly higher (3.6 %) power extraction relative to the initial fine-pitch of 0 deg. However, more data needs to be collected to support this statement. Note also, in Figure 7-8, how far off the initial 5 deg fine-pitch angle was in the second experiment. Still, the ESC algorithm was able to find the optimum.

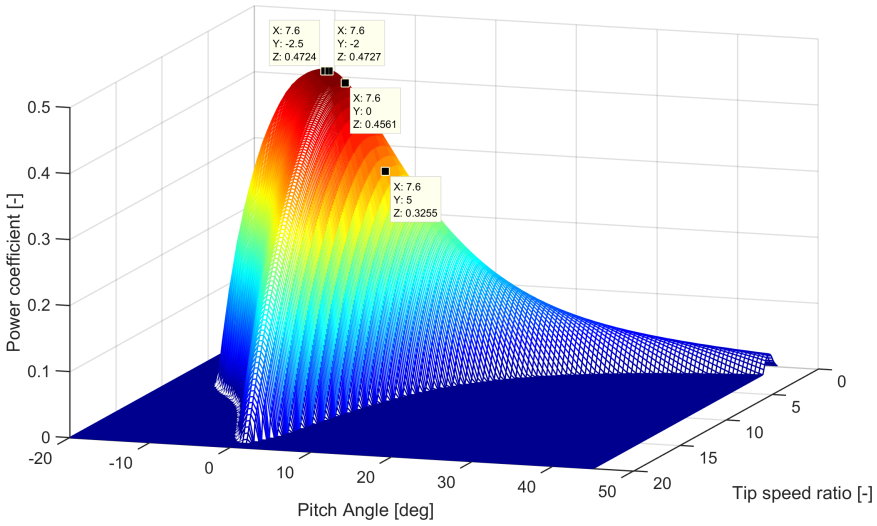

Figure 7-8: Selected fine-pitch angles on the Vestas V66 C_p-curve. The data points show the power coefficient (Z) for different combinations of tip-speed ratio (X) and fine-pitch angle (Y).

Finally, in Figure 7-9, a power coefficient curve from field recorded data under normal operation with the new fine-pitch angle is compared to the previous derived curve (which was presented in Figure 6-12). The result indicates that the new fine-pitch angle indeed results in a slightly higher C_p during below-rated operation. However, as stated earlier, more data needs to be collected to support this statement.

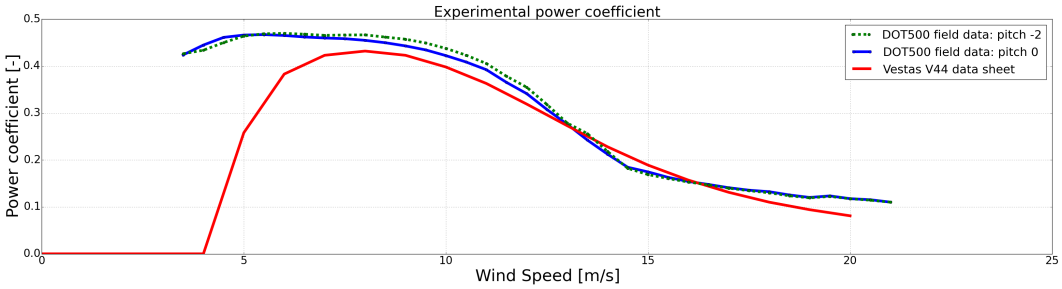

Figure 7-9: Comparison of experimentally derived power coefficient at fine-pitch -2 deg (green), fine-pitch 0 deg (blue) and the Vestas V44 data sheet (red).

The current example shows rotor power optimization from different initial conditions. However, the effective power increase between a fine-pitch angle of 0 and -2 deg remains difficult to distinguish with limited operational data. Therefore, the example in the next section is used to illustrate a more significant improvement by the ESC algorithm.

7-2 Generator Speed Control

This section starts with a brief introduction of the generator speed feedforward control law. Then the Extremum Seeking Control (ESC) algorithm implementation on this controller is outlined. Finally, test results are given and a conclusion on the optimal generator speed gain is derived.

7-2-1 Introduction to generator speed gain optimization

The spear valves convert the high-pressure, low-speed water flow into a low-pressure, high-speed water jet, i.e. hydrostatic to hydrodynamic power. This hydrodynamic power is harvested by the Pelton turbine, which is mechanically coupled to the generator. In Section 4-3-3, the relation between the generator rotational speed setpoint ω_{gen} and the water pressure in the Pelton feed was modelled as

$$\omega_{\text{gen}} = K\sqrt{\Delta p_{\text{feed}}} \qquad \text{where} \quad K = \sqrt{\frac{2}{\rho_{\text{water}}}}\frac{30}{\pi}\frac{1}{\text{PCD},} \tag{7-1}$$

where K was defined as the generator speed control gain. Hence, the generator speed is determined by a feedforward function evaluation based on the Pelton feed pressure in the hydrostatic flow. A theoretic approximation of the gain K was derived and resulted in a gain of 0.495. In this section the generator speed gain is optimized by an Extremum Seeking Control algorithm, to verify the correctness and optimality of the theoretical value on the practical set-up (see Figure 7-10).

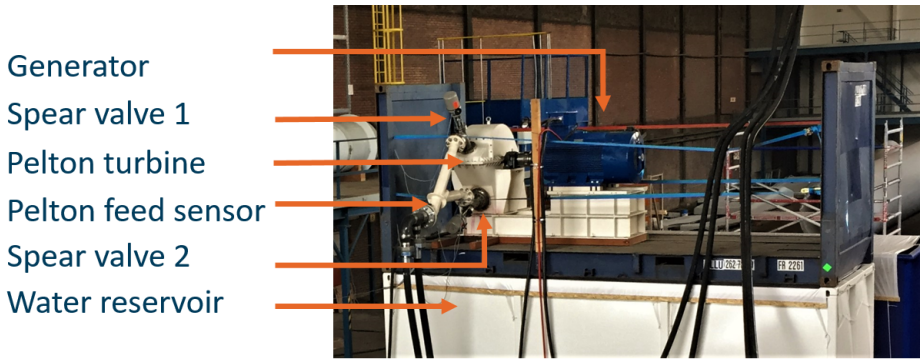

Figure 7-10: Overview of the mechanically coupled Pelton turbine and generator. The two variable spear valves are pointed towards the Pelton turbine buckets (located in the white housing). The Pelton feed pressure sensor is located near the mounting between the two flexible high-pressure water hoses and the steel Pelton piping.

7-2-2 Implementation of the generator speed ESC optimization

In the implementation described in this section, ESC optimizes the DOT500 effective generator power $P_{\text{gen}} = f(K)$ as a function of the generator speed K. The generator power is obtained through direct measurements from the generator. The algorithm is based on a dither-demodulation scheme, by periodic excitation at a single frequency on a turbine input: in this case the generator speed controller gain K. It optimizes the signal by finding the input Kthat results in a gradient $\partial P/\partial K$ that goes to zero. A schematic overview of the implementation is given in Figure 7-11.

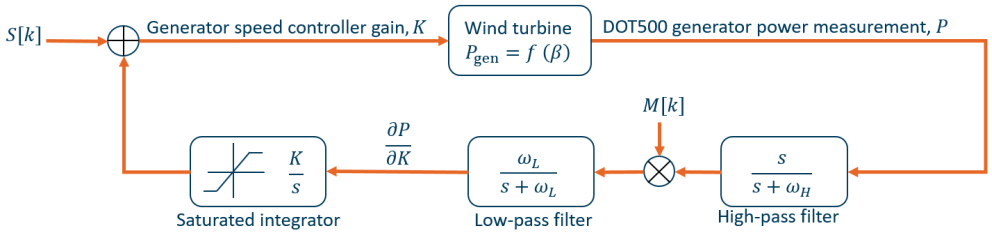

Figure 7-11: Schematic overview of the ESC implementation for maximizing the generator power P, with the generator speed controller gain K as the decision variable. An integrator saturation is included in order to prevent generator damage.

The most crucial parameter for the ESC algorithm is the dither frequency, which should be within the bandwidth of the input-output dynamics of the considered system [63]. As the system bandwidth from K to P_{gen} is higher than the one from β to P_{rotor}, the slow varying sinusoidal dither signal from the previous fine-pitch experiment automatically meets this requirement. This assumption significantly reduced computation time of the low- and high-pass filter cut-off frequencies ω_{L} and ω_{H}; which where already designed to remove wind disturbances and to sufficiently suppress and include dither related harmonics on the dither frequency, respectively. In order to abtain a significant SNR at the dither frequency, a dither amplitude of 0.03 is used.

The integrator gain K determines the algorithm convergence rate, and is taken as $1 \cdot 10^{-3}$. This integrator gain proved to result in a acceptable convergence speed, without destabilizing the ESC process. Finally, the phase shift between the signals $S[k]$ and $M[k]$, which compensates for the phase change in the ESC scheme, is set at 6 deg. The mentioned parameters are summarized in Table 7-2.

Parameter	Value
Dither amplitude	0.03
Phase-offset	6 deg
Dither frequency	0.04 rad/s
Low-pass filter cut-off frequency	0.0230 rad/s
High-pass filter cut-off frequency	0.0205 rad/s
Integrator gain	$1 \cdot 10^{-3}$

Table 7-2: Tuning parameters of the ESC scheme

7-2-3 Test results and optimal generator speed gain derivation

Results of the ESC generator speed gain optimization are presented in Figure 7-12. The ESC optimization is initiated from the theoretic approximated value 0.495. The algorithm shows a downward trend and fast convergence from 0 to 2000 s. Thereafter, the ESC algorithm stabilizes around a generator speed gain of 0.425, yielding maximum generator power.

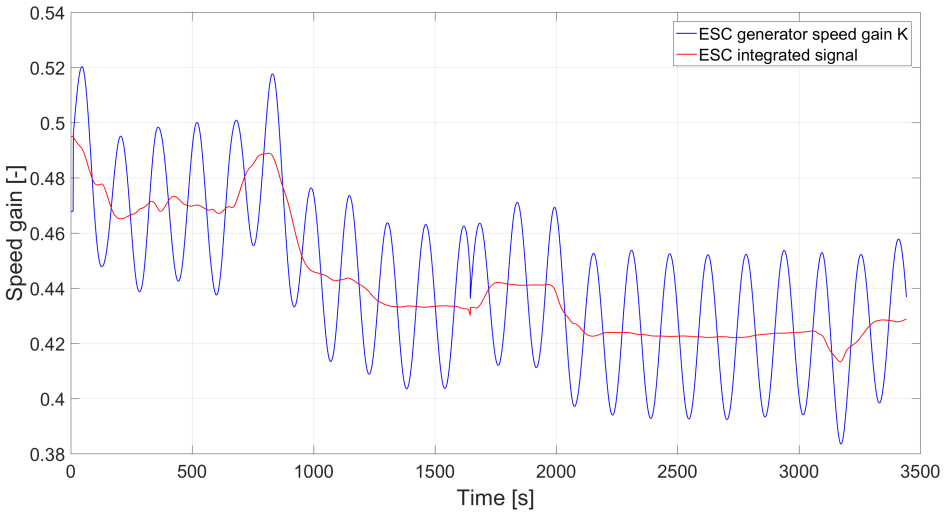

Figure 7-12: Extremum Seeking Control implemented to optimize the gain of the generator speed controller, maximizing the measured generator power

The improved performance with the new generator speed gain is shown in Figure 7-13. The figure shows both wind speed and generator power, with on left the theoretic approximated gain and on right the gain found with ESC. From the figure it is observed that the gain found with ESC results in a higher average generator power, even under a lower average wind speed.

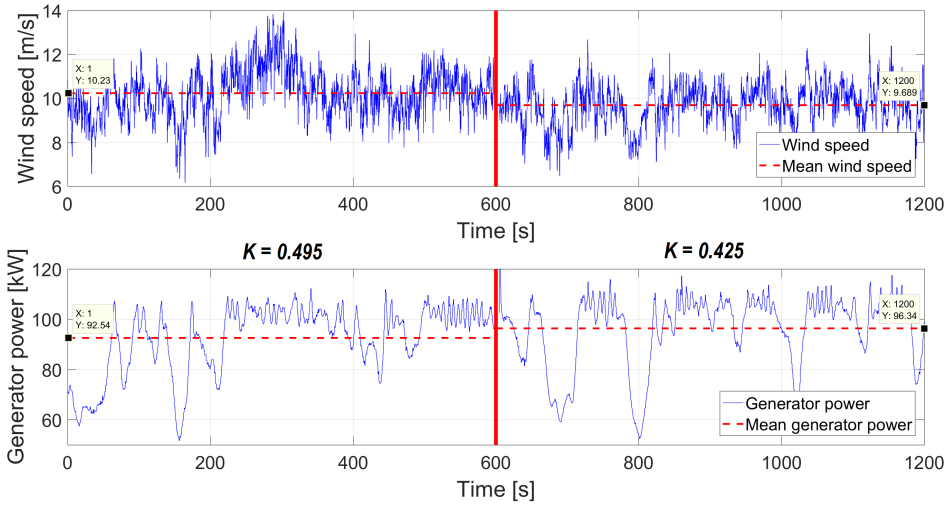

Figure 7-13: Effect of different controller gain on generator power. In the first 600 s the theoretic approximated gain is used, thereafter the gain derived with the ESC algorithm. Even with a lower average wind speed, the gain found with ESC results in a higher average generator power.

The obtained result indicates that the generator speed should be reduced in order to improve generator power extraction, however, more data needs to be collected to support this statement. Further investigation of the obtained result led to the observation that the ESC algorithm compensated for a malfunctioning pressure sensor, which is elaborated in the sequel of this section.

The pelton feed pressure sensor, located at the end of the high-pressure water hoses, is used in Equation 7-1 for the calculation of the generator speed. When taking account pressure losses and the height difference, these sensor measurements should be related to the Kamat discharge pressure measurements at the beginning of the same water hoses. This is schematically presented in Figure 7-14.

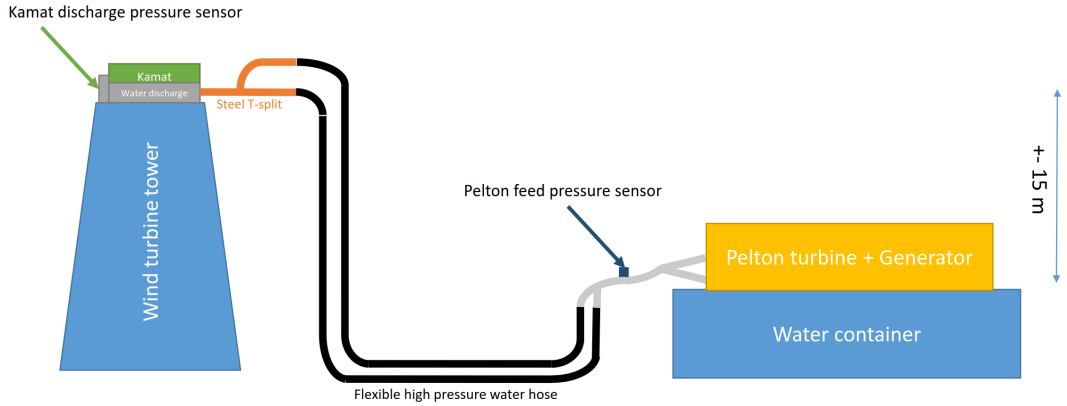

Figure 7-14: Schematic representation of the DOT500 test location. The Kamat feed discharge pressure measurement (at access platform height) should be related to the Pelton feed pressure sensor, only corrected 1.5 bar for the 15 m height difference between the two locations.

However, as presented in Figure 7-15, the pressure increase between the Kamat discharge sensor and the Pelton feed pressure sensor is much larger than the 1.5 bar expected from the 15 m height difference between the two sensor locations.

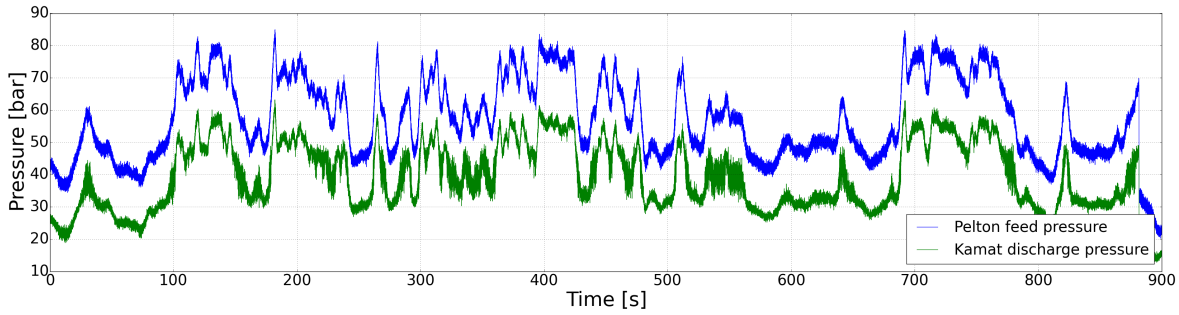

Figure 7-15: Comparison between Kamat discharge pressure and Pelton feed pressure.

To analyse the effect of this pressure difference on the generator speed calculation, three scenarios are considered for comparison. Each of the scenarios uses Equation 7-1, but uses a different measurement sensor and controller gain combination:

1. Scenario 1: Pelton feed pressure & theoretical speed gain
2. Scenario 2: Pelton feed pressure & ESC speed gain
3. Scenario 3: Kamat discharge pressure (with 1.5 bar correction) & theoretical speed gain

The results are presented in Figure 7-16. First, in *blue*, the Pelton feed pressure and original theoretically derived generator speed gain is used. Second, in *red*, the Pelton feed pressure is used with the gain derived from the ESC experiment. Finally, in *green*, the theoretic gain is used but now with the Kamat discharge pressure measurements.

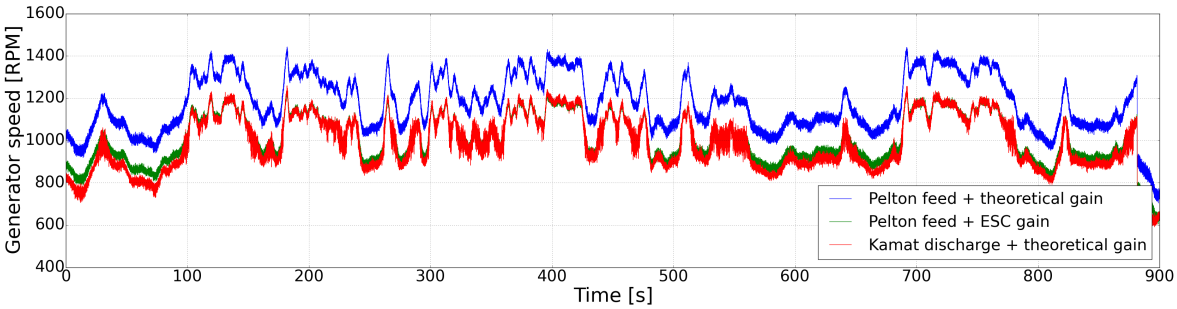

Figure 7-16: Required generator speed using three different methods. *Blue* indicates the original generator speed calculation. *Red* presents the generator speed calculation according to the gain found with the ESC experiment. *Green* uses the original gain, but with the Kamat discharge pressure measurements.

As observed in Figure 7-16, the second and third method show a nearly identical result. This suggests that the initial theoretical generator speed gain approximation was not far off, but the generator speed setpoint calculation was based on unreliable measurements. Furthermore, it indicates in the second method that the ESC algorithm has compensated for the malfunctioning Pelton feed pressure sensor.

The observed difference between sensor measurements became more evident at higher flows and pressures. These circumstances were also present during the ESC optimisation experiment. This suggests that the origin of this measurement problem is related to turbulent fluid effects, which have a larger influence on the pressure measurement at higher flows and pressures. However, the exact origin of this sensor problem is considered outside the scope of this thesis. The example is merely used to prove the capability of the ESC algorithm to compensate for modelling and measurement errors.

7-3 Future parameter tuning opportunities of the DOT500.

The earlier mentioned tests in this chapter are merely examples of the opportunities to tune the DOT500 turbine with Extremum Seeking Control. In the next phase of the DOT project, where the oil loop will be discarded, passive nozzle control in the below-rated region could be the solution for power optimization. The study of Diepeveen in [1] showed that by correctly sizing of the components between the rotor and the pressurized fluid jet at the exit of the nozzle, the wind turbine operates stable at the maximum power coefficient without any form of active control. Different "tuning" of the operational characteristics is possible by merely adjusting the size of the nozzle. Extremum Seeking Control appears to be a valuable method to perform this nozzle parameter tuning, using a generator power maximization objective. A schematic overview of this potential future optimization configuration is given in Figure 7-17.

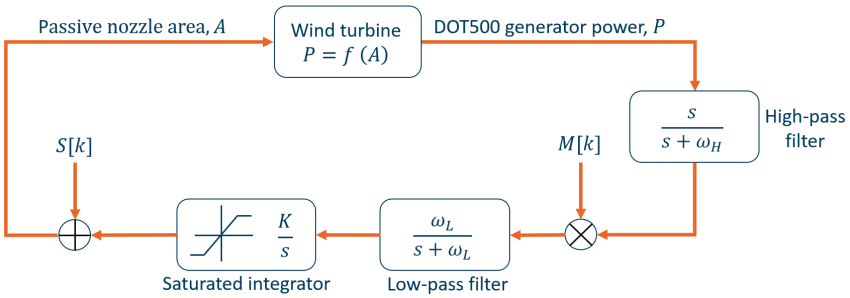

Figure 7-17: Schematic overview of the ESC implementation for maximizing the generator power P, with the passive nozzle diameter as the decision variable.

Furthermore, the current Vestas V44 turbine rotor is not designed for the hydraulic drive train concept that is used in the DOT500. Performance tests, that were performed outside the scope of this thesis, indicate that higher overall efficiency of the DOT500 could be obtained when the turbine deviates from tip-speed ratio for which the rotor was originally designed. Therefore, ESC should perhaps be implemented to find the fine-pitch angle that results in generator power maximization, instead of rotor power. In that case, the rotor characteristics are accurately coupled to the fluid power transmission characteristics. Due to the modularity of the designed ESC software implementation, all software for this test is now readily available.

Another opportunity arises when ESC is used to periodically tune parameters of individual wind turbines of a wind farm. In this way ESC can take into account wear, positioning and/or manufacturing differences among turbines; just as it did for the malfunctioning sensor in the previous section. This periodic optimization step requires only remote access and monitoring, and therefore minimizes offshore maintenance costs while improving energy yield.

Chapter 8

Conclusions & recommendations

8-1 Conclusions

In this thesis, the control design of the DOT500 hydraulic wind turbine was developed. The control design was validated through field trials and subsequently improved online with the data-driven Extremum Seeking Control (ESC) algorithm. In the introduction of this thesis, the following research objective was formulated:

How to implement below-rated hydraulic drive train control in the DOT500 wind turbine, as a substitute to regular generator torque control, and use direct data-driven optimization for verification of assumed controller parameters?

With this objective in mind, the following conclusions are drawn.

- The use of spear valves to regulate fluid pressure to vary the system torque, as opposed to the industry standard generator torque control, is not found in any other existing hydraulic wind turbine concept. The results in this thesis proof that active spear valve control is a feasible solution in both the below- and above-rated region.
- Field recorded tests of the DOT500 show that the implemented active spear valve control strategy is able to maintain the designed tip-speed ratio of 7.55 during below-rated operation. In combination with the derived fine-pitch angle of $-2\,\text{deg}$, this leads to operation at the theoretical maximum rotor power coefficient in the below-rated region. However, the actuator bandwidth of the current spear valves appeared to be too low for smooth transition between the below- and above-rated region in the current strategy.
- The DOT500 control objective was formulated to maximize wind energy capture, while taking account of safe operation restrictions such as rated power, rated speed and cut-out wind speed. However, the omission of thrust force mitigation in this objective was noticeable in a 10 % higher maximum thrust force during operation in the transition region, when compared to the original Vestas V44 data sheet.

- A simplified aerodynamic wind turbine simulation model was implemented to perform hardware-in-the-loop simulations. The modularity of the model allows for rapid modification, to test different hardware components under a variety of simulated wind conditions. This method is first used to simulate stair-case, realistic turbulent wind and emergency stop scenarios on a test set-up of the hydraulic drive train. Second, the method is applied to the blade pitch actuator for verification and fine-tuning of the pitch controller before actual operation. In this way, bugs and errors were quickly identified and fixed, without taking the risk of damaging the wind turbine by unexpected behaviour.

- Extremum Seeking Control (ESC) appeared to be a valuable data-driven method to compensate for modelling and measurement errors. First, the ESC method was used to update the optimal fine-pitch angle online for below-rated operation. Results indicate rotor power optimisation from different initial conditions at the updated fine-pitch angle, however, more data needs to be collected to support this statement. Second, the method was used to update the generator speed controller gain. Tracing back the latter derived result led to the detection of an incorrect pressure measurement at higher flow-pressure combinations, for which the gain derived with ESC compensated.

- The developed DOT500 control strategy and software implementation in this thesis proved to be safe and stable over the full turbine range of operation. Software design includes starting and (emergency) stopping procedures. Choking the high-pressure oil line proved to be a reliable method to stop the rotor under emergency conditions, as back-up to the industry standard pitch controlled emergency stop. The functioning of all controllers is examined during field trials on the actual DOT500 turbine.

8-2 Recommendations

Based on the results and conclusions derived in this thesis, the following recommendations remain open for further research:

- The current Vestas V44 rotor is not designed for the hydraulic drive train concept that is used in the DOT500. Due to the mismatching efficiency operating envelopes of the rotor and the hydraulic components, maximum rotor power not necessarily leads to generator power maximization. It could therefore be beneficial to no longer optimize for maximum rotor power extraction, but to use the generator power as decision variable instead. Preliminary performance tests, outside the scope of this thesis, indicate that operation at a far lower tip-speed ratio could result in a higher overall turbine efficiency. Operation at this new tip-speed ratio results in reduced flows at higher system pressures, which increases the pressure sensitivity to small spear valve position variations. This increases the controllability of the system torque and could be a solution to the current controller transition issue between below- and above-rated operation. Performance in this transition area could also be improved by either using faster spear valves or a Multi-Input Multi-Output (MIMO) control strategy that includes a saturation overlap of the two controllers.

- The thrust force was disregarded in the current control strategy. Results in this thesis indicate that a higher thrust force was present in the transition region, when compared to the original Vestas V44 data sheet. The possible unfavourable consequences of this mitigation, however, require further research and should be incorporated in the control strategy of future prototypes.
- Once the hydraulic oil loop is abandoned in the next DOT prototype phase, passive nozzle control for attaining the maximum power coefficient in the below-rated region should be investigated. Extremum Seeking Control has high potential as a data-driven tool to find the optimal effective nozzle area in this new control strategy. The modular nature of the Extremum Seeking Control algorithm makes it plug-and-play for tuning this nozzle parameter and a implementation is already proposed in this thesis.
- All results are associated with some uncertainty because of the amount of available data and the wind climate at the wind site. Online data-driven tuning algorithms are still scarcely applied in the wind industry. Therefore, further work should be focused at collecting more data to ensure performance improvements during nominal operation after ESC optimization.

Figure 8-1: Photo of the DOT500 prototype at Maasvlakte II, the Netherlands.

Appendix A

Vestas V44 data sheet

VESTAS V44 600 44.0

Company	VESTAS
Type/Version	V44
Rated power	600,0 kW
Secondary generator	0,0 kW
Rotor diameter	44,0 m
Tower	Tubular
Grid connection	50 Hz
Origin country	DK
Blade type	VESTAS 20
Generator type	One generator
Rpm, rated power	28,0 rpm
Rpm, initial	0,0 rpm
Hub height(s)	35,0; 40,0; 45,0; 50,0; 55,0 m
Maximum blade width	0,00 m
Blade width for 90% radius	0,00 m
Valid	No
Creator	
Created	2000-09-25 00:00
Edited	2000-09-25 00:00

Power curve: Manufactor 24/8-2000 1.225 20.00 0.00
Source Manufactor 24/8-2000

Source date	Creator	Created	Edited	Default	Stop windSpeed [m/s]	Air density [kg/m3]	Tip angle [°]	Power control	CT curve type
1899-12-30 00:00		2000-11-20 14:02	2000-11-20 14:03	No	20,0	1,225	0,0	Pitch	User defined

Power curve

Wind speed [m/s]	3,00	4,00	5,00	6,00	7,00	8,00	9,00	10,00	11,00	12,00	13,00	14,00	15,00	16,00	17,00
Power [kW]	0,00	0,00	30,00	77,00	135,00	206,00	287,00	371,00	450,00	514,00	558,00	582,00	594,00	598,00	600,00
Ce	0,000	0,000	0,258	0,383	0,423	0,432	0,423	0,398	0,363	0,319	0,273	0,228	0,189	0,157	0,131

Wind speed [m/s]	18,00	19,00	20,00
Power [kW]	600,00	600,00	600,00
Ce	0,110	0,094	0,081

Ct curve

Wind speed [m/s]	3,00	4,00	5,00	6,00	7,00	8,00	9,00	10,00	11,00	12,00	13,00	14,00	15,00	16,00	18,00
Ct	0,00	0,00	0,85	0,83	0,79	0,73	0,67	0,60	0,54	0,48	0,40	0,32	0,25	0,20	0,14

HP curve comparison

Vmean	[m/s]	5	6	7	8	9	10
HP value	[MWh]	706	1 163	1 637	2 099	2 489	2 835
Manufactor 24/8-2000 1.225 20.00 0.00	[MWh]	686	1 124	1 576	1 993	2 337	2 592
Check value	**[%]**	**3**	**3**	**4**	**5**	**7**	**9**

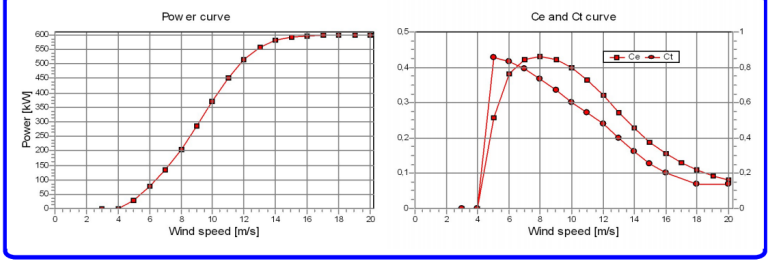

Figure A-1: Vestas V44 data sheet [29]

Appendix B

Initial derivation of pitch PI controller gains from equations of motion

The following derivation of the pitch PI controller gains is adopted from Jonkman et al. in [77]. A simple single-degree-of-freedom (single-DOF) model of a wind turbine is used. Because the goal of the blade pitch control system is to regulate the generator speed, the DOF is the angular rotation of the shaft. To compute the required control gains, it is beneficial to examine the equation of motion of this single-DOF system. From a simple free-body diagram of the drivetrain, the equation of motion is

$$\tau_{\text{aero}} - N_{\text{gear}}\tau_{\text{gen}} = I_{\text{drivetrain}}\frac{d}{dt}\left(\Omega_0 + \Delta\Omega\right) = I_{\text{drivetrain}}\Delta\dot{\Omega}, \tag{B-1}$$

where τ_{aero} is the low-speed shaft aerodynamic torque, τ_{gen} is the high-speed shaft generator torque, N_{gear} is the high-speed to low-speed gearbox ratio, Ω_0 is the rated low-speed shaft rotational speed, $\Delta\Omega$ is the small perturbation of low-speed shaft rotational speed about the rated speed, $\Delta\dot{\Omega}$ is the low-speed shaft rotational acceleration, and t is the simulation time. The drive train inertia consists of:

$$I_{\text{drivetrain}} = I_{\text{rotor}} + N_{\text{gear}}^2 I_{\text{gen}} \tag{B-2}$$

were I_{rotor} is the rotor mass moment of inertia and I_{gen} the generator inertia relative to the high speed shaft. Because the controller maintains constant power in region 3, the generator torque in region 3 is inversely proportional to the generator speed:

$$\tau_{\text{gen}}\left(N_{\text{gear}}\Omega\right) = \frac{P_0}{N_{\text{gear}}\Omega} \tag{B-3}$$

Similarly, assuming negligible variation of aerodynamic torque with rotor speed, the aerodynamic torque in region 3 is

$$\tau_{\text{aero}}\left(\theta\right) = \frac{P\left(\theta, \Omega_0\right)}{\Omega_0} \tag{B-4}$$

Using a first-order Taylor series expansion of Equation B-3 and B-4 one can see that

$$\tau_{\text{gen}} \approx \frac{P_0}{N_{\text{gear}}\Omega_0} - \frac{P_0}{N_{\text{gear}}\Omega_0^2}\Delta\Omega, \tag{B-5}$$

$$\tau_{\text{aero}} \approx \frac{P_0}{\Omega_0} + \frac{1}{\Omega_0}\left(\frac{\partial P}{\partial \theta}\right)\Delta\theta, \tag{B-6}$$

where $\Delta\theta$ is a small perturbation of the blade pitch angles about their operating point. With proportional-integral (PI) control, this is related to the rotor-speed perturbations by

$$\Delta\theta = K_{\text{P}} N_{\text{gear}}\Delta\Omega + K_{\text{I}}\int_0^t N_{\text{gear}}\Delta\Omega dt \tag{B-7}$$

where K_{P} and K_{I} are the blade pitch controller proportional and integral gains respectively. Now by using above expressions and setting $\dot{\phi} = \Delta\Omega$, Equation B-1 becomes

$$\frac{P_0}{\Omega_0} + \frac{1}{\Omega_0}\left(\frac{\partial P}{\partial \theta}\right)\left(K_{\text{P}} N_{\text{gear}}\dot{\phi} + K_{\text{I}}\int_0^t N_{\text{gear}}\dot{\phi}dt\right) - N_{\text{gear}}\left(\frac{P_0}{N_{\text{gear}}\Omega_0} - \frac{P_0}{N_{\text{gear}}\Omega_0^2}\dot{\phi}\right) = I_{\text{drivetrain}}\ddot{\phi} \tag{B-8}$$

Rewriting this equations results in:

$$\underbrace{\left[I_{\text{drivetrain}}\right]}_{M_\phi}\ddot{\phi} + \underbrace{\left[\frac{1}{\Omega_0}\left(\frac{\partial P}{\partial \theta}\right)K_{\text{P}} N_{\text{gear}} - \frac{P_0}{\Omega_0^2}\right]}_{C_\phi}\dot{\phi} + \underbrace{\left[\frac{1}{\Omega_0}\left(\frac{\partial P}{\partial \theta}\right)N_{\text{gear}} K_{\text{I}}\right]}_{\text{K}_\phi}\phi = 0 \tag{B-9}$$

From Equation B-9 it is clear that the PI-controlled rotor-speed error will respond as a second-order system with the natural frequency $\omega_{\phi\text{n}}$ and damping ratio ζ_ϕ equal to:

$$\omega_{\phi\text{n}} = \sqrt{\frac{K_\phi}{M_\phi}} \tag{B-10}$$

$$\zeta_\phi = \frac{C_\phi}{2\sqrt{K_\phi M_\phi}} = \frac{C_\phi}{2M_\phi\omega_{\phi\text{n}}} \tag{B-11}$$

The negative damping from the generator-torque controller, the $-P_0/\Omega^2$ part in C_ϕ in Equation B-9, will be ignored. Then using Equation B-10, and filling in K_ϕ and M_ϕ from Equation B-9, the proportional and integral gain become:

$$K_{\text{P}} = \frac{2I_{\text{drivetrain}}\Omega_0\zeta_\phi\omega_{\phi\text{n}}}{N_{\text{gear}}\left[-\frac{\partial P}{\partial \theta}\right]}, \tag{B-12}$$

$$K_{\text{I}} = \frac{I_{\text{drivetrain}}\Omega_0\omega_{\phi\text{n}}^2}{N_{\text{gear}}\left[-\frac{\partial P}{\partial \theta}\right]} \tag{B-13}$$

Appendix C

Experimental data for validation rotor mass moment of inertia

In this appendix the data that is used for the experimental validation of the rotor mass moment of inertia is given. Each plot shows the exact data points that are used for the calculations in Section 5-2-2.

Test 1

Figure C-1 shows the data for test 1.

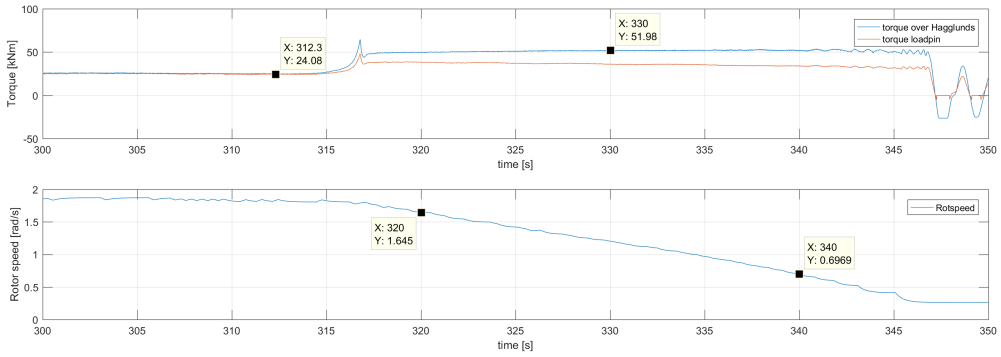

Figure C-1: Data measurements for test 1.

Test 2

Figure C-2 shows the data for test 2.

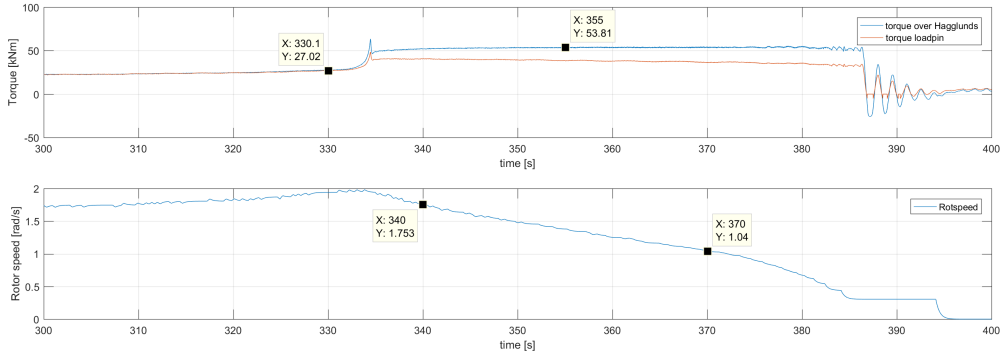

Figure C-2: Data measurements for test 2.

Test 3

Figure C-3 shows the data for test 3.

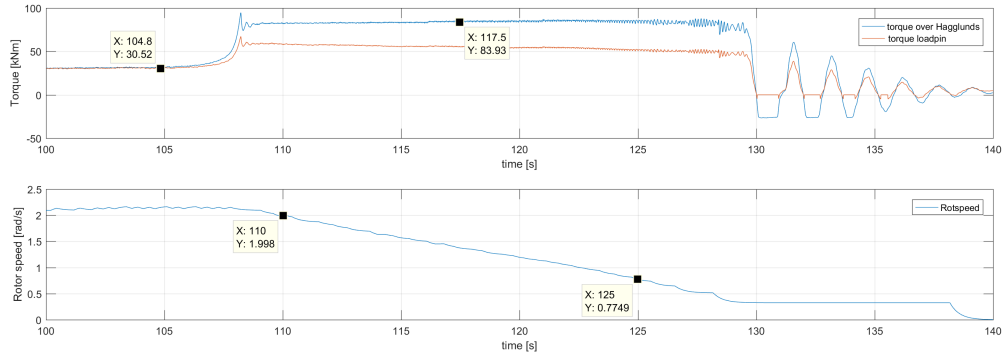

Figure C-3: Data measurements for test 3.

Test 4

Figure C-4 shows the data for test 4.

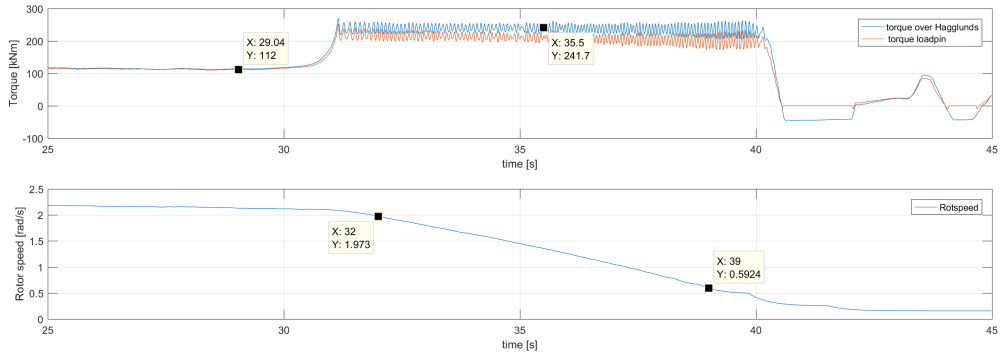

Figure C-4: Data measurements for test 4.

Test 5

Figure C-5 shows the data for test 5.

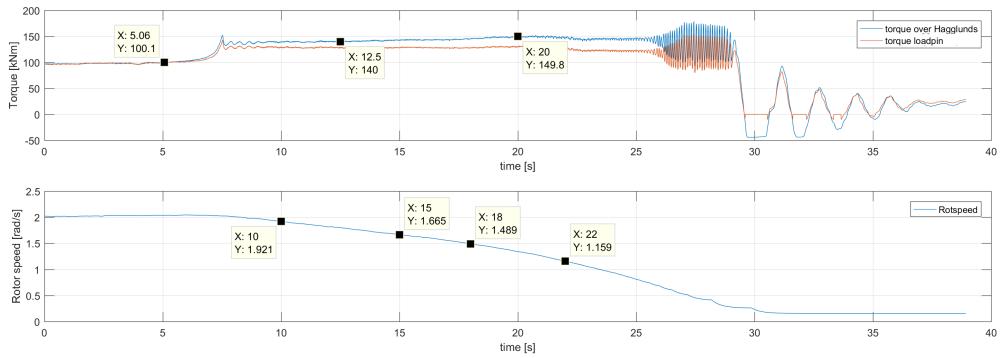

Figure C-5: Data measurements for test 5.

Test 6

Figure C-6 shows the data for test 6.

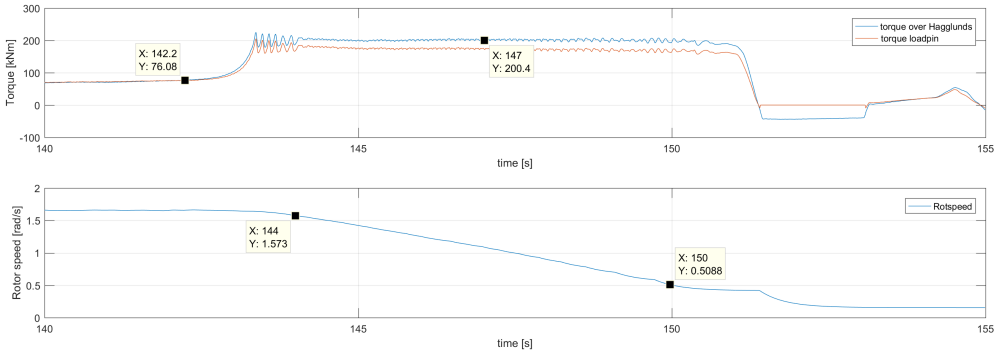

Figure C-6: Data measurements for test 6.

Test 7

Figure C-7 shows the data for test 7.

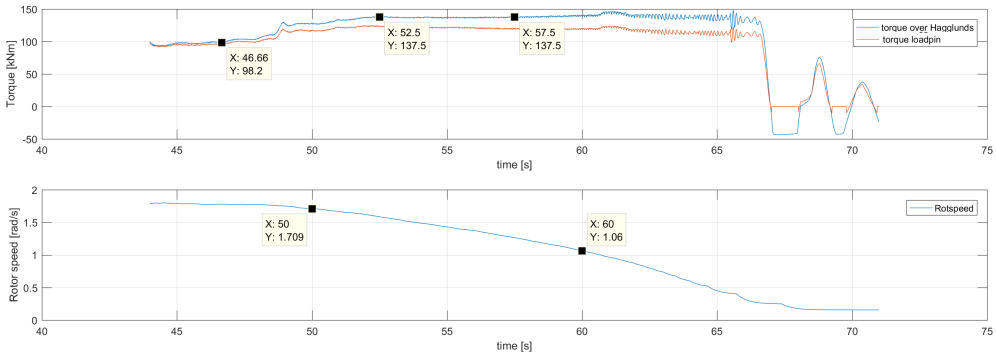

Figure C-7: Data measurements for test 7.

Test 8

Figure C-8 shows the data for test 8.

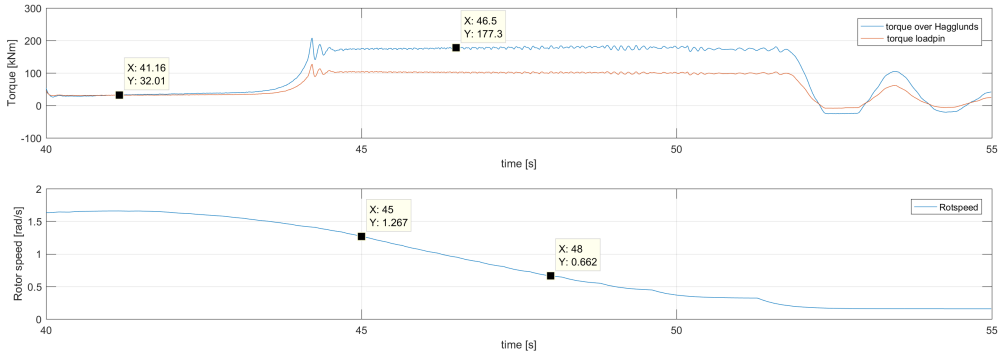

Figure C-8: Data measurements for test 8.

Bibliography

[1] N.F.B. Diepeveen, *On the Application of Fluid Power Transmission in Offshore Wind Turbines*. Phd thesis, TU Delft, Delft University of Technology, 2013.

[2] J. van der Tempel, "Energy extraction system, has water pump attached to rotor, windmill for pumping water from sea, water system connected to water pump, for passing water pumped from sea, and generator connected to water system," 2009.

[3] S. Rybak, "Description of the 3MW SWT-3 Wind Turbine at San Gorgonio Pass, California," tech. rep., The Bendix Coorporation Energy, Environment and Technology Office, 1982.

[4] A. Ragheb and M. Ragheb, "Wind Turbine Gearbox Technologies," in *Nuclear & Renewable Energy Conference (INREC), 2010 1st International*, pp. 1–8, IEEE, 2010.

[5] R. Budny and A. Crowther, "Meet the achilles heel behind most gearbox failures." http://www.nawindpower.com/online/issues/NAW1505/, 2015.

[6] H. Polinder, J. A. Ferreira, B. B. Jensen, A. B. Abrahamsen, K. Atallah, and R. A. McMahon, "Trends in wind turbine generator systems," *IEEE Journal of Emerging and Selected Topics in Power Electronics*, vol. 1, no. 3, pp. 174–185, 2013.

[7] I. G. P. Rodriguez, *Hydraulic drivetrains for wind turbines*. Msc thesis, Delft University of Technology, 2012.

[8] A. Akers, M. Gassman, and R. Smith, *Hydraulic power system analysis*. CRC press, 2006.

[9] Kable, "The world's 10 biggest wind turbines." http://www.power-technology.com/features/featurethe-worlds-biggest-wind-turbines-4154395/, 2014.

[10] H. Höller, "Hydrodynamics in Drive Technology," tech. rep., Voith, 1993.

[11] M. Sasaki, A. Yuge, T. Hayashi, H. Nishino, and M. Uchida, "Large Capacity Hydrostatic Transmission with Variable Displacement," *The 9th International Fluid Power Conference*, 2014.

[12] P. Silva, A. Giuffrida, N. Fergnani, E. Macchi, M. Cantu, R. Suffredini, M. Schiavetti, and G. Gigliucci, "Performance prediction of a multi-MW wind turbine adopting an advanced hydrostatic transmission," *Energy*, vol. 64, pp. 450–461, 2014.

[13] S. H. Salter and M. Rea, "Hydraulics for Wind," *European Wind Energy Conference, Hamburg, Germany*, pp. 22–26, 1984.

[14] D. Quarton, "Wind energy technology and the research challenge," tech. rep., GL Gerrard Hassan, 2013.

[15] R. J. Hicks, F. Cunliffe, and U. Giger, "Optimized Gearbox Design for Modern Wind Turbines," *2004 European Wind Energy Conference and Exhibition (EWEC 2004)*, pp. 1–8, 2004.

[16] Voith, "WinDrive Technology." http://www.voith.com/en/products-services/power-transmission/variable-speed-gearboxes/windrive-technology-26688.html, 2016.

[17] Artemis IP, "Artemis Intelligent Power," 2016.

[18] EMEA, "SeaAngel." http://www.emea.mhps.com/resources/documents/products/mpse-sea-angel-brochure.pdf, 2012.

[19] Renews, "Mitsubishi pulls plug on SeaAngel." http://renews.biz/83704/mitsubishi-pulls-plug-on-seaangel/, 2015.

[20] J. Jensen, A. Furuseth, P. Chang, and K. Thomsen, "Technological Advances in Hydraulic Drive Trains for Wind Turbines," *EWEA Annual Conference Proceedings*, vol. April, 2012.

[21] B. Skaare, B. Hörnsten, and F. Nielsen, "Energy considerations for wind turbines with hydraulic transmission systems.," in *Proceedings of EWEA Offshore 2011, Amsterdam, Netherlands*, 2011.

[22] B. Skaare, B. Hörnsten, and F. Gunnar Nielsen, "Modeling, simulation and control of a wind turbine with a hydraulic transmission system," *Wind Energy*, vol. 16.8, pp. 1259–1276, 2013.

[23] Statoil, "Hywind Project." http://www.statoil.com/, 2016.

[24] J. Schmitz, N. Diepeveen, N. Vatheuer, and H. Murrenhoff, "Dynamic Transmission Response of a Hydrostatic Transmission measured on a Test Bench," in *Proceedings of EWEA Conference, Copenhagen, Denmark*, 2012.

[25] M. Vukovic and H. Murrenhoff, "The Next Generation of Fluid Power Systems," *Procedia Engineering*, vol. 106, no. November, pp. 2–7, 2015.

[26] J. Schmitz, M. Vukovic, and H. Murrenhoff, "Hydrostatic Transmission for Wind Turbines: An Old Concept, New Dynamics," *ASME/BATH 2013 Symposium on Fluid Power and Motion Control*, no. October, 2013.

[27] D. Buhagiar, T. Sant, and M. Bugeja, "Control of an open-loop hydraulic offshore wind turbine using a variable-area orifice," *Proceedings of the International Conference on Offshore Mechanics and Arctic Engineering - OMAE*, vol. 9, no. November, 2015.

[28] D. Buhagiar and T. Sant, "Steady-state analysis of a conceptual offshore wind turbine driven electricity and thermocline energy extraction plant," *Renewable Energy*, vol. 68, no. August, pp. 853–867, 2014.

[29] Kulak, "Vestas V44/600 specifications." http://www.kulak.com.pl/Wiatraki/pdf /vestas%20v44.pdf, 2016.

[30] E. Bossanyi, "The Design of closed loop controllers for wind turbines," *Wind Energy*, vol. 3, no. 3, pp. 149–163, 2000.

[31] D. Simms, S. Schreck, M. Hand, and L. Fingersh, "NREL Unsteady Aerodynamics Experiment in the NASA-Ames Wind Tunnel: A Comparison of Predictions to Measurements," Tech. Rep. June, National Renewable Energy Laboratory, 2001.

[32] G. van der Veen, *Identification of wind energy systems*. PhD Thesis, Delft University of Technology, Delft., 2013.

[33] E. van Solingen and J. W. van Wingerden, "Iterative feedback tuning of wind turbine controllers," *To Be Published*, pp. 1–29, 2016.

[34] J. G. Ziegler and N. Nichols, "Optimum Settings for Automatic Controllers," *Transaction of the A.S.M.E*, vol. 64, pp. 759–768, 1942.

[35] K. Van Heusden, "Non-Iterative Data-Driven Model Reference Control," *Communications*, vol. 4658, p. 167, 2010.

[36] H. Hjalmarsson, S. Gunnarsson, and M. Gevers, "A convergent iterative restricted complexity control design scheme," *Proceedings of the 33rd IEEE Conference on Decision and Control*, vol. 2, no. March, pp. 1735 –1740 vol.2, 1994.

[37] H. Hjalmarsson, "Iterative feedback tuning - An overview," *International Journal of Adaptive Control and Signal Processing*, vol. 16, no. 5, pp. 373–395, 2002.

[38] K. Van Heusden, A. Karimi, and D. Bonvin, "Data-driven model reference control with asymptotically guaranteed stability," *International Journal of Adaptive Control and Signal Processing*, vol. 25, no. 4, pp. 331–351, 2011.

[39] H. Hjalmarsson, "Control of nonlinear systems using iterative feedback tuning," *Proceedings of the 1998 American Control Conference*, pp. 2083–2087, 1998.

[40] H. Hjalmarsson, M. Gevers, S. Gunnarsson, and O. Lequin, "Iterative feedback tuning: Theory and applications," *IEEE Control Systems Magazine*, vol. 18, no. 4, pp. 26–41, 1998.

[41] J. Sjöberg and F. De Bruyne, "on a Nonlinear Controller Tuning Strategy," *Proceedings of the 14th IFAC World Congress, Beijing, China*, pp. 1–6, 1999.

[42] H. Hjalmarsson, "Efficient tuning of linear multivariable controllers using iterative feedback tuning," *International Journal of Adaptive Control and Signal Processing*, vol. 13, no. 7, pp. 553–572, 1999.

[43] H. Hjalmarsson, "Model free tuning of controllers: Experience with time-varying linear systems," *Procedings European Control Conference*, pp. 2869 – 2874, 1995.

[44] F. D. Bruyne, B. D. Anderson, M. Gevers, and N. Linard, "Iterative controller optimization for nonlinear systems," in *Proceedings of the 36th Conference on Decision & Control San Diego, California USA*, no. December, 1997.

[45] J. Sjöberg and M. Agarwal, "Non-linear controller tuning based on linearized time-variant model," *Proceedings of American Control Conference, Albuquerque, New mexico, 4-6 June*, pp. 3336–3340, 1997.

[46] H. Hjalmarsson and S. M. Veres, "Robust loopshaping using Iterative Feedback Tuning," *European Control Conference*, pp. 2046–2051, 2001.

[47] H. Procházka, M. Gevers, B. P. O. Anderson, and C. Ferrera, "Iterative feedback tuning for robust controller design and optimization," *Proceedings of the 44th IEEE Conference on Decision and Control, and the European Control Conference, CDC-ECC '05*, vol. 2005, pp. 3602–3607, 2005.

[48] M. F. Heertjes, B. Van Der Velden, and T. Oomen, "Constrained Iterative Feedback Tuning for Robust Control of a Wafer Stage System," *IEEE Transactions on Control Systems Technology*, vol. 24, no. 1, pp. 56–66, 2016.

[49] W. Meng, S. Q. Xie, Q. Liu, C. Z. Lu, and Q. Ai, "Robust Iterative Feedback Tuning Control of a Compliant Rehabilitation Robot for Repetitive Ankle Training," *IEEE/ASME Transactions on Mechatronics*, vol. 4435, no. ILC, 2016.

[50] S. T. Navalkar and J. W. van Wingerden, "Iterative feedback tuning of an LPV feedforward controller for wind turbine load alleviation," *IFAC-PapersOnLine*, vol. 48, no. 26, pp. 207–212, 2015.

[51] G. O. Guardabassi and S. M. Savaresi, "Virtual reference direct design method: an off-line approach to data-based control system design," *IEEE Transactions on Automatic Control*, vol. 45, no. 5, pp. 954–959, 2000.

[52] M. Campi, A. Lecchini, and S. Savaresi, "Virtual reference feedback tuning: a direct method for the design of feedback controllers," *Automatica*, 2002.

[53] A. Lecchini, M. C. Campi, and S. M. Savaresi, "Virtual reference feedback tuning for two degree of freedom controllers," *International Journal of Adaptive Control and Signal Processing*, vol. 16, no. 5, pp. 355–371, 2002.

[54] M. C. Campi and S. M. Savaresi, "Direct Nonlinear Control Design : The Virtual Reference Feedback Tuning (VRFT) Approach," *IEEE Transactions on Automatic Control*, vol. 51, no. 1, pp. 14–27, 2006.

[55] F. Gasdos and P. Dostál, "Direct controller design and iterative tuning applied to the coupled drives apparatus," *Journal of Electrical Engineering*, vol. 60, no. 2, pp. 106–111, 2009.

[56] J. K. Huusom, N. K. Poulsen, and S. B. Jørgensen, "Improving convergence of Iterative Feedback Tuning," *Journal of Process Control*, vol. 19, no. 4, pp. 570–578, 2009.

[57] O. Lequin, M. Gevers, M. Mossberg, E. Bosmans, and L. Triest, "Iterative feedback tuning of PID parameters: Comparison with classical tuning rules," *Control Engineering Practice*, vol. 11, no. 9, pp. 1023–1033, 2003.

[58] M. Radac, R. Precup, and R. Roman, "Model-Free control performance improvement using virtual reference feedback tuning and reinforcement Q-learning," *International Journal of Systems Science*, vol. 7721, no. October, pp. 1–13, 2016.

[59] M. C. Campi, A. Lecchini, and S. M. Savaresi, "An Application of the Virtual Reference Feedback Tuning Method to a Benchmark Problem," *European Journal of Control*, vol. 9, no. 1, pp. 66–76, 2003.

[60] F. Previdi, T. Schauer, S. M. Savaresi, and K. J. Hunt, "Data-Driven Control Design for Neuroprotheses: A Virtual Reference Feedback Tuning (VRFT) Approach," *IEEE Transactions on Control Systems Technology*, vol. 12, no. 1, pp. 176–182, 2004.

[61] J. D. Rojas, X. Flores-Alsina, U. Jeppsson, and R. Vilanova, "Application of multivariate virtual reference feedback tuning for wastewater treatment plant control," *Control Engineering Practice*, vol. 20, no. 5, pp. 499–510, 2012.

[62] M. Leblanc, "Sur l'électrification des chemins de fer au moyen de courants alternatifs de fréquence élevée," *Revue générale de l'électricité*, vol. 12, pp. 275–277, 1922.

[63] Y. Xiao, Y. Li, and M. Rotea, "Experimental Evaluation of Extremum Seeking Based Region-2 Controller for CART3 Wind Turbine," *34th Wind Energy Symposium*, no. January, pp. 1–19, 2016.

[64] M. Krstić and H.-H. Wang, "Stability of extremum seeking feedback for general nonlinear dynamic systems," *Automatica*, vol. 36, no. 4, pp. 595–601, 2000.

[65] K. J. Åström and W. Björn, *Adaptive control*. Courier Corporation, 2013.

[66] M. Krstić, "Performance improvement and limitations in extremum seeking control," *Systems & Control Letters*, vol. 39, no. 5, pp. 313–326, 2000.

[67] J. Creaby, Y. Li, and J. E. Seem, "Maximizing Wind Turbine Energy Capture using Multivariable Extremum Seeking Control," *Wind Engineering*, vol. 33, pp. 361–387, 2009.

[68] M. Rotea, "Analysis of multivariable extremum seeking algorithms," *Proceedings of the 2000 American Control Conference*, vol. 1, no. June, pp. 433–437, 2000.

[69] K. B. Ariyur and M. Krstić, "Analysis and design of multivariable extremum seeking," *Proceedings of the American Control Conference*, vol. 4, no. 0, pp. 2903–2908, 2002.

[70] K. B. Ariyur and M. Krstic, *Real-time optimization by extremum-seeking control*. John Wiley & Sons, 2003.

[71] M. Komatsu, H. Miyamoto, H. Ohmori, and A. Sano, "Output maximization control of wind turbine based on extremum control strategy," *Proceedings of the 2001 American Control Conference*, vol. 2, no. 8, pp. 1739–1740, 2001.

[72] I. Chiharu, H. Hiroshi, and O. Hiromitsu, "Modeling of variable pitch micro wind turbine and its output optimization control with adaptive extremum control scheme," *Nippon Kikai Gakkai Ronbunshu, C Hen/Transactions of the Japan Society of Mechanical Engineers, Part C*, vol. 69, no. 11, pp. 3034–3040, 2003.

[73] A. Ghaffari, M. Krstic, and S. Sechagiri, "Power optimization and control in wind energy conversion systems using extremum seeking," *IEEE Transactions on Control Systems Technology*, vol. 22, no. 5, pp. 1684–1695, 2014.

[74] Y. Xiao, Y. Li, and M. A. Rotea, "Multi-objective Extremum Seeking Control for Enhancement of Wind Turbine Power Capture with Load Reduction," *Journal of Physics: Conference Series.*, vol. 753, no. 5, 2016.

[75] R. J. M. Fernando D. Bianchi, Hernan De Battista, *Wind Turbine Control Systems. Principles, Modelling and Gain Scheuling Design.* Springer, 2007.

[76] A. Tustin, "a Method of Analysing the Behaviour of Linear Systems in Terms of Time Series," *Electrical Engineers-Part IIA: Automatic Regulators and Servo Mechanisms*, vol. 94, no. 1, pp. 130–142, 1947.

[77] J. Jonkman, S. Butterfield, W. Musial, and G. Scott, "Definition of a 5-MW reference wind turbine for offshore system development," Tech. Rep. NREL/TP-500-38060, NREL National Renewable Energy Laboratory, feb 2009.

[78] K. Kohnson, L. Pao, M. Balas, and L. Fingersh, "Control of Variable Speed Wind Turbines," *Ieee Control Systems Magazine*, vol. 26, no. 3, p. 6, 2006.

[79] L. Pao and K. Johnson, "Control of Wind Turbines: Approaches, Challenges, and Recent Developments," *Ieee Control Systems Magazine*, vol. 31, no. APRIL, pp. 44 – 62, 2011.

[80] L. Euler, *Maximes pour arranger le plus avantageusement les machines destinées á élever de l'eau par le moyen des pompes'.* Mémoires de l'Académie des Sciences de Berlin, 8 ed., 1752.

[81] I. Houtzager, J. W. van Wingerden, and M. Verhaegen, "VARMAX-based closed-loop subspace model identification," in *proceedings of The 48th IEEE Conference on Decision and Control, Shanghai, China*, 2009.

[82] K. Kragh and P. Fleming, "Rotor speed dependent yaw control of wind turbines based on empirical data," *Proceedings of the 50th AIAA Aerospace Sciences Meeting Including the New Horizons Forum and Aerospace Exposition, Nashville, TN*, no. January, pp. 1–9, 2012.

[83] K. A. Kragh and M. H. Hansen, "Load alleviation of wind turbines by yaw misalignment," *Wind Energy*, vol. 17(7), pp. 971–982, 2014.

[84] K. E. Johnson and P. A. Fleming, "Development, implementation, and testing of fault detection strategies on the National Wind Technology Center's controls advanced research turbines," *Mechatronics*, vol. 21, no. 4, pp. 728–736, 2011.

[85] J. Rapp and J. Turesson, *Hydrostatic Transmission in Wind Turbines Development of Test Platform.* PhD thesis, Linköping University, 2015.

[86] A. González Rodríguez, A. González Rodríguez, and M. Burgos Payán, "Estimating Wind Turbines Mechanical Constants," *International Conference on Renewable Energies and Power Quality*, pp. 9–11, 2007.

[87] M. F. Sanner, "Python: a programming language for software integration and development," *J Mol Graph Model*, vol. 17, no. 1, pp. 57–61, 1999.

[88] Modbus Organisation, "Modbus." http://www.modbus.org, 2016.